

NORTHWESTERN UNIVERSITY

Anisotropic Gold Nanostars: Seedless Growth Mechanism, Post-Synthetic Separation, and
Ligand Distribution Quantification

A DISSERTATION

SUBMITTED TO THE GRADUATE SCHOOL
IN PARTIAL FULFILLMENT OF THE REQUIREMENTS

for the degree

DOCTOR OF PHILOSOPHY

Field of Materials Science and Engineering

By

Kavita Chandra

EVANSTON, ILLINOIS

June 2018

© Copyright by Kavita Chandra 2018

All Rights Reserved

ABSTRACT

Anisotropic Gold Nanostars: Seedless Growth Mechanism, Post-Synthetic Separation, and Ligand Distribution Quantification

Kavita Chandra

Metal particles at the nanoscale display unique physical, chemical, and optical properties corresponding to their size, shape, and ligands. These factors can be manipulated to target specific biomedical applications, such as drug delivery and sensing, through functionalized surfaces. The development of specialized synthetic methods for the precise control of nanoparticle size and morphology enables the desired ligand distribution. Nanoparticle curvature has a significant effect on ligand loading; understanding this relationship is critical in determining particle-cell interactions. This work focused on the factors affecting the synthesis mechanism and post-synthetic separation of anisotropic gold nanostars (AuNS) and the quantification of ligand distribution on varying nanoparticle morphologies.

The seedless synthesis of AuNS requires two precursors, but the methodology often resulted in poor yield of branched particles. In Chapter 2, we described four critical factors affecting the final nanoparticle morphology: mechanical agitation, concentration ratio, buffer type, and chemical environment. We established a set of design considerations to increase the homogeneity of nanoparticle shape and anisotropic particle yield and expanded the library of precursors used for anisotropic growth to include a morpholine-based buffer. This work led to the creation and classification of a collection of nanoparticles with tunable optical properties.

While synthesizing AuNS with a morpholine-based buffer was possible, the buffer created unstable and heterogenous particles. In Chapter 3, we showed a robust strategy to obtain highly homogenous AuNS populations through a stabilization and sorting method. By altering the storage conditions, particle stability increased three-fold. The stable AuNS were separated through density gradient centrifugation (DGC) based on branch length and number. We demonstrated that one round of DGC efficiently separated AuNS populations and additional rounds did not improve homogeneity.

In Chapter 4, we used our optimized separation methodology to obtain DNA-functionalized particles. Specifically, we probed how curvature of individual particles impacted ligand distribution through time-of-flight secondary ion mass spectrometry. AuNS with a medium density of branches had six-fold more ligands per particle than a spherical nanoparticle of comparable size. As branch number increased beyond this point, the negative curvature increased and hindered additional ligand loading. This fundamental tool allowed for the simultaneously probing of an inorganic core and unlabeled-ligands on the single particle level.

Finally, in chapter 5, we explored the mechanism of the seedless growth of anisotropic AuNS through evaluating the intermediate species of the reaction. By repurposing electron paramagnetic resonance spectroscopy, we studied the radical concentration *in situ* during the reaction and determined the effect of buffer concentration and type. We correlated the trend in radical intensity to the ensemble optical properties and individual particle morphology.

ACKNOWLEDGEMENTS

First and foremost, I want to deeply thank my advisor, Prof. Teri W. Odom, for her guidance and unwavering support throughout my Ph.D. When I first joined the department, I was unsure about what research to pursue and Teri provided direction while always pushing me to become a better scientist, writer, and communicator. She has a personalized mentorship style and commits to her students' interests and chosen career paths, even my non-traditional one. Outside of her scientific guidance, Teri is a role model for me and will be a guiding influence in my future endeavors. Her unparalleled work ethic and continued commitment to excellence are an inspiration. She has the uncanny ability to raise everyone around her to higher standards. I will spend the rest of my career trying to emulate these qualities!

I would also like to thank my qualifying and thesis committee members – Prof. Ramille Shah, Prof. Vinayak Dravid, Prof. Mark Hersam, and Prof. George Schatz – for their contributions to my research. They have provided helpful feedback on my projects and made significant impact on my graduate career.

I am also very grateful that I have had so many wonderful collaborators, co-authors, and friends in the Odom Group. In particular, I would like to thank Kayla Culver and Duncan Dam for making me the third member of the then-new bio subgroup (BSG!) and training me comprehensively. The early years of my research career were markedly some of the best because of times in lab with them. I want to thank all past and present Odom group members for their companionship and support, specifically Yi Hua, Stephanie Werner, Vished Kumar, Emma Coughlin, Michael Knudson, Alex Hyrn, Weijia Wang, Tingting Liu, and Ankun Yang.

I am grateful for all of my educators, particularly from elementary, middle, and high school, whose strong intellectual curiosity and interest in me have shaped my life trajectory: Mrs. Kauzlarich, Mrs. Johnson, Mr. Friedlander, Mrs. Ewart, and Mrs. Kelly. I would also like to thank my collaborators in the Northwestern community and at other institutions: Brandon Rugg, Dr. Michael Eller, Prof. Emile Schweikert, Dr. Juyeong Kim, and Prof. Qian Chen. Also, all of my work would not have been possible without the Northwestern staff and research facilities, including Lisa Gugwor, Lindsay Haukebo, Dr. Keith MacRenaris, Dr. Eric Roth, Dr. Benjamin Myers, Dr. Jinsong Wu, Dr. Charlene Wilke, and Dr. Angki Kandela. I also appreciatively acknowledge the HMCP and BTP fellowships for funding.

On a personal note, I would also like to thank my extended family – the Arun, Vrid, Balu, Prakash, Ravichandran, Balasubramanian, Patel, Khatau, Thackersey, Vemuri, and Aggarwal families – for always believing in me and supporting me through these long five years. Especially for excusing my absence at many birthdays, vacations, weddings, and other events due my scientific research. Also, thanks to my MIT family – Anjali Muralidhar (Rai), Dr. Anjali Thakkar, Dr. Sumi Sinha, Shannon Moran, Eliana Schelifer, Celine Yang, and Pierre-Guy Douyon – for supporting me and not asking when I would graduate. Additionally, I want to thank my Chicago family – Dr. Niki Mansukhani (Kogar), Dr. Jade Balla, Dr. Anshul Kogar, Lam-Kiu Fong, Amelia Plunk, Piku Mody, and Shivan Patel (B.I.L.) – who made the day-to-day of my graduate school life infinitely happier. In particular, I would like to thank my classmate Linda Guiney for her support, personally and professionally. Specifically, for receiving approximately 50 texts/emails/snaps/gchats daily from me, for always taking Lakefill walks, and for never turning down an outdoor pitcher. Without her, I am certain I could not have earned my Ph.D. I am eternally

grateful to have met Linda, my Chicago sister, and developed one of the most formative friendships of my life.

I must thank my brilliant partner, Doctor Shyam Khatau, Ph.D. He is the kindest, most generous person I know, and equally as weird as I am. In particular during past year, I would like to thank him for listening to me complain, calming me during my (co)sinusoidal panic attacks, and all the while loving me unconditionally. During my periods of self-doubt, Shyam has always believed in me and supported me to accomplish things I could never have without him. Our whole truly is greater than the sum of our parts. After two years, I have already learned and grown so much, and I cannot wait for the rest of our lives!

Most importantly, I need to thank my parents, Appa and Amma, for being the best parents and people I have ever known. The greatest privilege of my life is being their daughter. My father came from a small village in India to become a prominent professor in the U.S., while supporting his entire family. All of my accomplishments are due to sacrifices that he made. My mother, also an academic, cared for my sister and me for many years and is the fiercest-loving parent. I thank her deeply for always putting my needs above her own and supporting me even when I don't deserve it. I thank my sister, Alli, for being my best friend, confidant, support system, article editor, PowerPoint maker, essay writer, and so much more; nearly all of my achievements have been directly due to my sister's help. My best memories in life are with her and, more significantly, in my darkest times, Alli has been my sole guiding light. Where ever I am in life, I know I will never be alone because I have her and that is the greatest comfort.

This dissertation and all of my life's work are due to my sister, parents, and Shyam pushing me to be my best and inspiring me every day.

LIST OF ABBREVIATIONS

| | |
|--------------------|---|
| 3D | Three dimensional |
| AuNS | Gold nanostar |
| CTAB | Cetrimonium bromide |
| CY | Coincidental yield |
| DGC | Density gradient centrifugation |
| DLS | Dynamic light scattering |
| DNA | Deoxyribonucleic acid |
| EM | Electron microscopy |
| EPPS | 4-(2-Hydroxyethyl)-1-piperazinepropanesulfonic acid |
| EPR | Electron paramagnetic resonance |
| FCC | Face centered cubic |
| FFT | Fast Fourier Transform |
| Gd(III) | Gadolinium(III) |
| HAuCl ₄ | Gold(III) chloride trihydrate or gold salt |
| HEPES | 4-(2-hydroxyethyl)-1-piperazineethanesulfonic acid |
| HR | High resolution |
| ICP-MS | Inductively coupled plasma mass spectrometry |
| K _a | Acid dissociation constant |
| LSP | Localized surface plasmon |
| MES | 2-(N-morpholino)ethanesulfonic acid |
| MOPS | 3-(N-morpholino)propanesulfonic acid |

| | |
|------|-------------------------------------|
| MRI | Magnetic resonance imaging |
| NIR | Near infrared |
| NP | Nanoparticle |
| PEG | Polyethylene glycol |
| RPM | Rotation per minute |
| SEM | Scanning electron microscopy |
| SERS | Surface enhanced Raman spectroscopy |
| SIMS | Secondary ion mass spectrometry |
| ss | Single stranded |
| TEM | Transmission electron microscopy |
| TOF | Time of flight |
| UV | Ultraviolet |
| Vis | Visible |
| w/v | Weight by volume |
| wt% | Weight percent |

For Alli, Amma, Appa, and Shyam

TABLE OF CONTENTS

| | |
|---|-----------|
| ABSTRACT..... | 3 |
| ACKNOWLEDGEMENTS | 5 |
| LIST OF ABBREVIATIONS | 8 |
| TABLE OF CONTENTS | 11 |
| LIST OF FIGURES | 15 |
| LIST OF TABLES | 32 |
| CHAPTER 1 : INTRODUCTION TO SYNTHESIS OF GOLD NANOPARTICLES | 33 |
| 1.1 Introduction to Noble Metal Nanoparticles | 34 |
| 1.1.1 Historical Background | 34 |
| 1.1.2 Applications of Metal Nanoparticles | 38 |
| 1.2 Structure and Morphology of Gold Nanoparticles..... | 40 |
| 1.2.1 Size..... | 42 |
| 1.2.2 Shape..... | 44 |
| 1.3 Overview of Synthetic Approaches for Anisotropic Gold Nanoparticles | 45 |
| 1.3.1 Seed-Mediated Synthetic Methods | 45 |
| 1.3.2 Seedless Synthetic Methods..... | 48 |
| 1.3.3 Seedless Synthesis of Gold Nanostars | 49 |
| 1.4 Dissertation Overview | 50 |

CHAPTER 2 : MANIPULATING THE ANISOTROPIC STRUCTURE OF GOLD

NANOSTARS USING GOOD'S BUFFERS53

| | | |
|-------|--|----|
| 2.1 | Introduction..... | 54 |
| 2.2 | Results and Discussion | 56 |
| 2.2.1 | Stirring During Synthesis Improved Yield of AuNS | 56 |
| 2.2.2 | Reaction Kinetics and Stability Depended on Good's Buffer Type | 61 |
| 2.2.3 | pH Crucial for AuNS Formation..... | 70 |
| 2.2.4 | Structure and Corresponding Optical Properties of AuNS | 73 |
| 2.3 | Summary..... | 80 |
| 2.4 | Experimental Methods | 85 |
| 2.4.1 | Gold Nanostar Synthesis..... | 85 |
| 2.4.2 | Particle Characterization Techniques | 86 |

CHAPTER 3 : SEPARATION OF STABILIZED MOPS GOLD NANOSTARS BY

DENSITY GRADIENT CENTRIFUGATION87

| | | |
|-------|--|-----|
| 3.1 | Introduction..... | 88 |
| 3.2 | Results and Discussion | 89 |
| 3.2.1 | Establishing MOPS AuNS Stability | 89 |
| 3.2.2 | Exchanging Solvent Storage Conditions | 95 |
| 3.2.3 | Comparing Linear and Step Gradients..... | 95 |
| 3.2.4 | Characterizing Separation of AuNS in a Linear Gradient | 100 |
| 3.2.5 | Sorting AuNS by Branch Length and Number | 102 |
| 3.2.6 | Sorting AuNS through a Second Round of Separation..... | 106 |

| | |
|--|------------|
| | 13 |
| 3.3 Summary | 106 |
| 3.4 Experimental Methods | 108 |
| 3.4.1 Gold Nanostar Synthesis..... | 108 |
| 3.4.2 Particle Characterization Techniques | 108 |
| 3.4.3 Density Gradient Centrifugation..... | 109 |
| | |
| CHAPTER 4 : LABEL FREE PARTICLE-BY-PARTICLE QUANTIFICATION OF | |
| DNA-LOADING ON SORTED GOLD NANOSTARS..... | 110 |
| 4.1 Introduction..... | 111 |
| 4.2 Results and Discussion | 113 |
| 4.2.1 Separation and Characterization of Sorted HEPES AuNS | 113 |
| 4.2.2 Quantification of Co-Emitted Species | 116 |
| 4.2.3 Determination of DNA Distribution Per Particle on Varying Morphologies | 133 |
| 4.3 Summary | 137 |
| 4.4 Experimental Methods | 137 |
| 4.4.1 Nanoparticle Synthesis..... | 137 |
| 4.4.2 Particle Characterization Techniques | 138 |
| 4.4.3 Density Gradient Centrifugation..... | 138 |
| 4.4.4 Functionalization of DNA to Nanoparticles | 139 |
| 4.4.5 Surface Area and Volume Characterization | 139 |
| 4.4.6 Secondary Ion Mass Spectroscopy | 140 |
| | |
| CHAPTER 5 : DETECTING AND VISUALIZING REACTION INTERMEDIATES OF | |
| ANISOTROPIC NANOPARTICLE GROWTH..... | 142 |

| | |
|--|------------|
| | 14 |
| 5.1 Introduction..... | 143 |
| 5.2 Results and Discussion | 144 |
| 5.2.1 Proposed Mechanism for Radical Generation | 144 |
| 5.2.2 Radical Generation Corresponded to a Plasmon Peak Shift and Particle Size Increase | 147 |
| 5.2.3 Second Radical Concentration Increase Indicated Higher Aspect Ratio AuNS. | 156 |
| 5.2.4 Radical Generation Depended on Buffer Concentration | 160 |
| 5.2.5 Visualizing AuNS Growth through In Situ TEM | 164 |
| 5.3 Summary..... | 169 |
| 5.4 Experimental methods | 169 |
| 5.4.1 Nanostar synthesis and characterization | 169 |
| 5.4.2 Particle Characterization Technique | 169 |
| 5.4.3 Growth Solution Quenching | 170 |
| 5.4.4 Electron Paramagnetic Resonance Spectroscopy | 171 |
| REFERENCES..... | 172 |
| CURRICULUM VITAE..... | 188 |

LIST OF FIGURES

- Figure 1.1: Photographs of the Lycurgus cup.** The Lycurgus cup in (a) reflected and (b) transmitted light. Adapted from the Department of Prehistory and Europe, The British Museum, Higgitt *et. al.*⁴ with permission under the Creative Commons CC-BY license as published through Springer Nature. 35
- Figure 1.2: Scheme of localized surface plasmons for metal nanoparticles.** Schematic of plasmon oscillation for a sphere, showing the displacement of the conduction electron charge cloud relative to the nuclei. Adapted with permission from Schatz *et. al.*⁹ Copyright 2003 American Chemical Society. 37
- Figure 1.3: HR-TEM images of spherical noble metal nanocrystals with different crystal structures:** (a) a single-crystalline, (b) a singly twinned, (c) a multiple planar-twinned, (d) a cyclic penta-twinned gold, and (e, f) a multiple-twinned icosahedral gold nanocrystal. Adapted with permission from Xu *et. al.*⁵⁰ Copyright 2011 American Chemical Society. 41
- Figure 1.4: Photographs of aqueous solutions of gold nanospheres (4- 40 nm, top) and gold nanorods (bottom) as a function of increasing dimensions.** Corresponding TEM images of the nanoparticles are shown (all scale bars 100 nm). For the nanorods, the aspect ratio varies from 1.3 to 5 for short rods (TEMs f-j) and 20 (TEM k) for long rods. Adapted with permission from Mody *et. al.*⁵⁴ Copyright 2010 American Chemical Society..... 43
- Figure 1.5: General methodology for the generation of gold nanorods.** Adapted with permission from Murphy *et. al.*⁶⁹ Copyright 2004 American Chemical Society. 46

Figure 2.1: Stirring the reaction caused red shift in AuNS peak absorbance and improved yield of branched particles. (a) TEM images of HEPES AuNS that were unstirred (left) or stirred for 30 min at 200 RPM. (b) The absorbance spectra of HEPES AuNS that were unstirred (blue line) or stirred at 200 RPM from 1 (cyan line) up to 30 min (red line). The absorbance was measured 24 h after the reaction completed and indicated that increasing stirring time resulted in a red-shifted absorbance. The inset highlights the decrease in the peak near 500 nm corresponding to the spherical byproducts. 57

Figure 2.2: Percent of AuNS particles in solution increased with stirring speed. Growth solutions were stirred for 30 min at the designated RPM and then left in the dark overnight. TEM grids were made and particle analysis was conducted through ImageJ. For each stirring time point, 300 – 400 particles were measured. For all three buffers, an overall increase in the percentage of AuNS occurred. MOPS had the greatest heterogeneity (ca. 65%) 59

Figure 2.3: LSP shifted with stirring speed. The final primary peak wavelength of (a) HEPES, (b) EPPS, and (c) MOPS AuNS after being stirred for varying lengths of time at 200 – 1400 RPM. The growth solutions were stirred for 0 – 30 min and then left overnight to allow for the reaction to complete. The spectra were taken 24 h after stirring. With an increase in stirring time, a red shift in the absorbance peak for all three buffers occurred. For HEPES and EPPS AuNS, a plateau in the LSP resonance occurred around 6 min of stirring. There was no clear effect of the different stirring speeds on the peak wavelength. 60

Figure 2.4: MES buffer did not produce AuNS at any pH or concentration. MES absorption spectra (a, b) and corresponding particle size (c, d) for 100 to 2500 R_{MES} were collected at two

pHs: 6.7 and 5.65. MES was tested through the entire buffering range from 5.5 – 6.7. Two representative spectra are shown above and below the pK_a of MES. At a high pH, the solutions were unable to form particles in solution except at the lowest [MES] of 20 mM. At $pH < pK_a$, MES formed spherical particles in solution. 63

Figure 2.5: Reaction rates of HEPES, EPPS, and MOPS AuNS synthesis at $R_{buffer} = 700$. (a)

The final spectra of AuNS formed by HEPES, EPPS, and MOPS at $R_{buffer} = 700$. TEM images indicate general shape of AuNS solutions from different buffers with box size $200\text{ nm} \times 200\text{ nm}$.

(b) Peak absorbance wavelength of HEPES, EPPS, and MOPS AuNS as the reaction progressed.

The solid symbols correspond to λ_1 , the peak ca. 700 nm, and the open symbols correspond to λ_2 , the peak ca. 1000 nm.

(c) The λ_1 peak of the absorbance spectra was recorded over 30 days for

AuNS synthesized at 700 R_{buffer} . HEPES and EPPS AuNS peak wavelength was maintained, while

MOPS AuNS peak wavelength blue shifted. 65

Figure 2.6: Reaction rate spectra of AuNS. Absorbance spectra of **(a)** HEPES, **(b)** EPPS, and

(c) MOPS AuNS during the synthesis at $R_{buffer} = 700$. Spectra were taken every two min until the reaction completed. EPPS and MOPS AuNS had two LSP peaks, and HEPES AuNS had one peak.

The reaction time for MOPS was longer than that of HEPES and EPPS. 67

Figure 2.7: Stability of the LSP peak of HEPES AuNS under different storage conditions.

HEPES AuNS were stored either in the growth solution or resuspended in water. These solutions were either then stored at 4°C or at room temperature. The storage conditions that caused the smallest shift in LSP peak was in the original growth solution at 4°C . Only a 9-nm LSP shift occurred after 20 days and 15-nm over 40 days, which indicated excellent structural and colloidal

stability. Blue-shifts in the LSP under other storage conditions are due to AuNS re-shaping, similarly seen with MOPS AuNS solutions blue-shift over a month corresponding to particle shape changing (Figure 2.8). Particle aggregation was not affected by storage conditions. 68

Figure 2.8: TEM images of AuNS from different buffers after a month. TEM images of HEPES, EPPS, and MOPS particles one and 30 days after synthesis. HEPES and EPPS particles maintained the morphology over time; however, the MOPS particles mostly turned into spheres. 69

Figure 2.9: pH dependence of HEPES, EPPS, and MOPS AuNS formation throughout their respective buffering range. (a) Photographs of the solutions at varying pH conditions, $pK_a \pm 0.7$. (b) Corresponding peak wavelength of the absorbance spectra. The solid symbols corresponded to λ_1 , and the open symbols corresponded to λ_2 71

Figure 2.10: Spectra of AuNS synthesized at varying pH. Absorbance spectra of (a) HEPES, (b) EPPS, and (c) MOPS AuNS synthesized at varying pH within the buffering range of each buffer. HEPES AuNS were formed throughout the buffering range but with decreased absorbance with increased pH. EPPS AuNS formed below and slightly above the pK_a of the buffer. When the pH was much greater than the pK_a of the buffer, EPPS AuNS were unable to form. MOPS solutions showed the lowest tolerance to changes in pH and were unable to form AuNS above the pK_a of the buffer..... 72

Figure 2.11: Absorbance spectra of HEPES, EPPS, and MOPS through the concentration ranges that produced AuNS. Absorbance spectra and TEM images of AuNS synthesized with (a)

250 to 750 R_{HEPES} , **(b)** 400 to 2500 R_{EPPS} , and **(c)** 500 to 1100 R_{MOPS} . The lowest concentration (black) starts on the left and increases to the right to the highest concentration (red or cyan). The number in the upper RH corner of each image is the corresponding R_{buffer} value 75

Figure 2.12: Photographs of AuNS at varying buffer concentrations. AuNS solutions synthesized with **(a)** HEPES, **(b)** EPPS, and **(c)** MOPS at varying concentrations. MOPS produced AuNS in the smallest concentration range compare with EPPS and HEPES. EPPS was able to produce AuNS in the largest concentration range from $R_{\text{EPPS}} = 400$ to 2500..... 76

Figure 2.13: DLS of AuNS synthesized at varying concentrations. AuNS were synthesized from 100 to 2500 R_{buffer} . With an increase in R_{EPPS} , AuNS particle size increased whereas HEPES and MOPS AuNS particle size plateaued or solutions aggregated. These measurements were taken through DLS, which determines the size distribution of particles (typically spheres) in solution. Since our particles are anisotropic, the hydrodynamic diameter measurements serve only as an estimate of their overall size. 77

Figure 2.14: Low magnification images of AuNS. Zoomed-out TEM images of **(a)** HEPES, **(b)** EPPS, and **(c)** MOPS AuNS. HEPES and EPPS solutions had fewer spheres. These images demonstrate the large distribution of particle shapes for MOPS AuNS solutions. Based on ≥ 300 particles, we found MOPS AuNS solutions contained 53% spherical byproducts..... 78

Figure 2.15: HR-TEM images of HEPES AuNS synthesized at 700 R_{HEPES} . HEPES AuNS branches grew in the [111] direction. The dotted white boxes indicate the area analyzed by FFT (bottom). AuNS particles were on an amorphous carbon mesh grid that produced the ring-like

structure in the FFT. The presence of the ring depended on the sample thickness (i.e. AuNS branch thickness) and the electron beam intensity. 81

Figure 2.16: HR-TEM images of EPPS AuNS synthesized at 2500 R_{EPPS} . EPPS AuNS grew in the [110] direction. The dotted white boxes indicate the area analyzed by FFT (bottom). AuNS particles were on an amorphous carbon mesh grid that produced the ring-like structure in the FFT. The presence of the ring depended on the sample thickness (i.e. AuNS branch thickness) and the electron beam intensity. 82

Figure 2.17: HR-TEM images of MOPS AuNS synthesized at 1100 R_{MOPS} . MOPS AuNS grew in the [110] direction. The dotted white boxes indicate the area analyzed by FFT (bottom). AuNS particles were on an amorphous carbon mesh grid that produced the ring-like structure in the FFT. The presence of the ring depended on the sample thickness (i.e. AuNS branch thickness) and the electron beam intensity. 83

Figure 2.18: HR-TEM images of HEPES, EPPS, and MOPS AuNS. HR-TEM images were taken of AuNS synthesized at the highest R_{buffer} for each buffer. The solid white box on the particle (left) indicates where the zoomed-in HR-TEM image (center) was acquired. The lattice spacing (d) and the direction perpendicular to the corresponding lattice planes (white arrow) were determined through FFT analysis. The FFT (right) was taken from the area outlined with a dotted white box. **(a)** HEPES AuNS have branches in the [111] direction indicated by $d \sim 0.235$ nm between lattice planes and the electron diffraction pattern. **(b)** EPPS and **(c)** MOPS AuNS have branches in the [110] direction, as evidenced by the 0.289 nm distance between lattice planes. 84

Figure 3.1: Stabilization and separation of MOPS AuNS scheme. 91

Figure 3.2: Absorbance peak of MOPS AuNS in growth solution blue shifted over 30 days.

(a) The absorbance was measured 24 h (red line) after the addition of H_{AuCl}₄ up to 30 days (black line) in 5-day increments. (b) TEM images of MOPS AuNS after 1, 15, and 30 days after the addition of H_{AuCl}₄. 92

Figure 3.3: Absorbance spectra of AuNS stored in growth solution for initial 24 h. The λ_1 and

λ_2 peak do not decrease in intensity nor shift in wavelength 24 h after the addition of gold. The maximum peak absorbance was reached after 60 min, which indicated that the reaction completed. Only minimal shifts in the LSP and absorbance occurred between 1 and 24 h. 93

Figure 3.4: Shape stability of AuNS increased due to water resuspensions. (a) Plot of the LSP

resonance shift over time for solutions at one (black) and two (red) resuspensions. Filled markers correspond to the λ_1 peak and open markers correspond to λ_2 peak. (b) TEM images of AuNS 30 days after one or two resuspensions in water. 96

Figure 3.5: Linear gradient allowed for greater separation than step gradient. The control

(no AuNS) was used to establish the linear and step gradients and contained the coloring agent Trypan blue. Once the gradients were established, AuNS were centrifuged through a gradient with without Trypan blue (Sorted AuNS). A linear gradient with increasing viscosity and density produced two bands: red and blue. The particles had a greater spatial separation over a step gradient. The step gradient produced two bands, but within the bands particles were not further separated. 97

Figure 3.6: Varying concentration of layered sample did not affect separation. The layered sample for DGC is typically limited to 200 – 500 μL ; however, the concentration of the sample can be increased. We changed the concentration of the 500- μL layered solution to 20 \times , 40 \times , and 60 \times the as-synthesized solution concentration. The concentration of the layered solution did not affect the quality of AuNS separation..... 99

Figure 3.7: Separation of AuNS through a linear density gradient by size and shape. (a) Photographs of F5 – F23 of the AuNS (top) layered on top of the gradient and (bottom) centrifuged through the linear sucrose gradient. (b) Absorbance spectra for every odd-numbered fraction from F5 – F23. (c) Representative TEM images from F5, F13, and F17 show branched particles in all the different fractions..... 101

Figure 3.8: Branch length increased with fraction number. (a) TEM images for odd numbered fractions in F5 – F19. (b) The percentage of branches that are short (< 30 nm) or long (> 30 nm) for each fraction. 103

Figure 3.9: Zoomed-out TEM images from each fraction after one round of DGC. Images were collected from different areas of the grid and analysis was performed on ≥ 500 branches per fraction. 104

Figure 3.10: Analyzing the AuNS branch number population for each fraction. (a) TEM images of high, medium, and low number of branches. The dimensions of all the images are 150 nm \times 200 nm. (b) The percentage of the AuNS population that have low (1 – 2), medium (3 – 4) or high (> 5) number of branches. 105

Figure 3.11: Round 2 of DGC fractions did not enrich branch populations. (a) Odd-numbered original fractions were layered on top of a 50 – 55 wt% sucrose gradient and centrifuged for 45 min at $4400 \times g$. Top (T), middle (M), and bottom (B) fractions of the each of the round 2 fractionated samples were collected. (b) The branch number distribution for each of the T, M, and B samples was analyzed manually. The population distribution was similar among the original fractions (O) and re-fractionated samples..... 107

Figure 4.1: Density gradient centrifugation (DGC) isolates populations of AuNS with similar morphologies. (a) Photographs of a centrifuge tube before (top) and after (bottom) centrifugation of a concentrated AuNS solution in a sucrose linear density gradient. (b) Branch number distribution within each fraction based on manual branch counting of ≥ 400 particles per fraction. (c) TEM images of unsorted AuNS (top) and different fractions after DGC (bottom). The cartoon scheme denotes different areas of curvature (i.e. positive, negative, or neutral) on a AuNS. 114

Figure 4.2: Low-magnification TEM images of sorted HEPES AuNS. Zoomed-out images of 100 mM HEPES AuNS sorted through DGC in fractions (a) 2, (b) 4, (c) 6, (d) 8, and (e)10. All scale bars are 100 nm. These images demonstrate the difference in particle shape of the sorted AuNS..... 115

Figure 4.3: The surface area and volume per particle in each AuNS fraction..... 117

Figure 4.4: Gd-nanoparticle surface area standard curve. Gold nanospheres (2 – 150 nm in diameter) with known surface area were functionalized with Gd-chelate. Through ICPMS, the

amount of Gd per particle was determined. This standard curve was used to determine the surface area of the sorted AuNS particles. 118

Figure 4.5: SEM image of F4 AuNS as prepared for SIMS analysis. (a) At 12 K, the images show that the nanoparticles organize on to the surface in small groups after deposition. (b) At 65 K, higher resolution reveals the distribution of individual particles on the surface. AuNS connect in long chains with a few particles completely isolated on the substrate. 119

Figure 4.6: Schematic of cluster SIMS experiment. Each projectile is separated in time and space, and upon impacting the sample causes emission from a volume 10-15 nm in diameter. For each projectile impact the co-emitted ions are mass analyzed by TOF and collected in a mass spectrum. 120

Figure 4.7: Mass spectra identified notable peaks of functionalized AuNS. Notable peaks are identified and color coded: purple are carbon clusters, pink are DNA related, orange are silicon related, green are salt, and black are Au clusters. 121

Figure 4.8: Mass spectrum of F4 AuNS. Each panel shows a different mass range and the y-axis is the intensity divided by the number of projectile impacts. Notable peaks are identified and color coded. Pink peaks are related to the DNA, black are gold clusters, orange are related to the silicon support, green are sodium chloride clusters, and blue are carbon clusters. 122

Figure 4.9: Two-dimensional correlation heat map for F2 AuNS. The color scale is correlation coefficient, with red corresponding to positive correlation and blue to negative correlation. Ions

which do not have a significant correlation were not plotted. The evaluated ions are listed on the y-axis, the coincidental mass spectrum is listed on the x-axis..... 123

Figure 4.10: Two-dimensional correlation heat map for F4 AuNS. The color scale is correlation coefficient, with red corresponding to positive correlation and blue to negative correlation. Ions which do not have a significant correlation were not plotted. The evaluated ions are listed on the y-axis, the coincidental mass spectrum is listed on the x-axis..... 124

Figure 4.11: Two-dimensional correlation heat map for F6 AuNS. The color scale is correlation coefficient, with red corresponding to positive correlation and blue to negative correlation. Ions which do not have a significant correlation were not plotted. The evaluated ions are listed on the y-axis, the coincidental mass spectrum is listed on the x-axis..... 125

Figure 4.12: Two-dimensional correlation heat map for F8 AuNS. The color scale is correlation coefficient, with red corresponding to positive correlation and blue to negative correlation. Ions which do not have a significant correlation were not plotted. The evaluated ions are listed on the y-axis, the coincidental mass spectrum is listed on the x-axis..... 126

Figure 4.13: Two-dimensional correlation heat map for F10 AuNS. The color scale is correlation coefficient, with red corresponding to positive correlation and blue to negative correlation. Ions which do not have a significant correlation were not plotted. The evaluated ions are listed on the y-axis, the coincidental mass spectrum is listed on the x-axis. 127

Figure 4.14: Two-dimensional correlation heat map for 50-nm spheres. The color scale is correlation coefficient, with red corresponding to positive correlation and blue to negative

correlation. Ions which do not have a significant correlation were not plotted. The evaluated ions are listed on the y-axis, the coincidental mass spectrum is listed on the x-axis. 128

Figure 4.15: Emission homogeneity demonstrated 100% surface coverage. The sum of the silicon, salt and DNA/gold on all samples gives ca. $1 \pm .1$ (100 %), which indicates all the regions of the sample surface were identified. Good agreement between the DNA + Gold and DNA homogeneity was found, signifying most of the DNA was bound to the particles. This is a representative homogeneity graph for the F4 AuNS sample. 131

Figure 4.16: Homogeneity of each nanoparticle sample. The surface composition was determined for each sample using the methodology described in the article. In each sample the composition of the surface is composed of exposed silicon, sodium chloride, and gold particles. In all cases there is good agreement between DNA and DNA plus gold, indicating little or no unbound DNA was deposited on the surface. Additionally, the summation of silicon, sodium chloride and DNA plus gold gives 1.0 ± 0.1 showing all regions of the surface were identified. The absolute number of deposited gold particles depends on the initial concentration in solution and the deposition area. 132

Figure 4.17: Coincidental yield for particles of varying morphology. The CY ratio for the for the deprotonated thymine nucleotide and a fragment of the nucleotide at m/z 248 compared to the 50-nm spheres. F4 demonstrated $6\times$ enhancement of loading compared with spheres as shown through ratio of the CY of deprotonated nucleotide. 136

Figure 5.1: A chemical reaction scheme for the synthesis of AuNS with a Good's buffer (HEPES or EPPS), measured by EPR. 145

Figure 5.2: Absorption spectra of HEPES and EPPS at varying concentrations. (a) One injection of HAuCl_4 into 100 – 1000 mM HEPES produced solutions with one LSP peak, λ_1 . Above 500 mM [HEPES], the particles were unstable in solution and did not produce AuNS. (b) One injection of HAuCl_4 into 100 – 1000 mM EPPS produced solutions with two LSP peaks, λ_1 and λ_2 . For all [EPPS], the particles were stable in solution and produced AuNS. 146

Figure 5.3: Characterization of intermediate species of HEPES + HAuCl_4 . (a) Initial EPR signal of 100 mM HEPES before (inset) and after the addition of HAuCl_4 . (b) Integrated radical concentration and LSP (λ_1) of the absorbance spectra over the reaction time. t_1 indicates the time of the initial increase in radical concentration. (c) TEM images of the quenched growth reaction at 3, 6, and 10 min..... 148

Figure 5.4: EPR spectra of pure HAuCl_4 and EPPS. No radical signal was produced for pure (a) HAuCl_4 or (b) EPPS..... 149

Figure 5.5: EPR spectra of HAuCl_4 + HEPES. (a) The radical signal peaked at 10 minutes and decayed over the rest of the reaction. (b) At 60 minutes, the signal was weak..... 150

Figure 5.6: Raw HEPES and EPPS EPR spectra. Raw spectra for (a) 100, (b) 250, (c) 500, (d) 750, and (e) 1000 mM EPPS and HEPES concentrations at varying time points. 151

Figure 5.7: Reaction Rate Spectra for HEPES. Absorbance spectra of HEPES AuNS during the course of the synthesis at 100 mM. Spectra were taken every 1 min until the reaction was completed. 100 mM HEPES AuNS solutions had one LSP peak (λ_1)..... 152

Figure 5.8: Quenched spectra compared to reaction rate spectra. The LSP peak of the real-time reaction rate spectra (solid) compare well with the quenched solutions (dashed)..... 153

Figure 5.9: Low magnification images of quenched HEPES AuNS. Zoomed-out TEM images of 100 mM HEPES AuNS in the growth solution quenched at (a) 3, (b) 5, (c) 10, and (d) 60 minutes. These images demonstrate the change in particle shape over the reaction. After ca. 10 minutes, the reaction completed and the particles did not grow further in solution. 154

Figure 5.10: Average branch length, particle volume, and branch length of HEPES AuNS. 100 mM HEPES + HAuCl₄ was quenched at 6, 8, 9, 10, and 12 minutes with PEG. Using ImageJ, particle morphology was analyzed at each time point based on ≥ 300 particles. (a) The average branch length increased to ca. 14 nm during the first 10 minutes of the reaction. The branch length did not increase significantly after that time. The large error bars are due to the heterogeneity of branch number for HEPES AuNS. (b) The average particle volume remained low below 8 minutes, due to the formation of small particles. After 8 minutes, the particle grew in average particle volume which corresponded to the large growth in branch length and branch number. (c) From 6 to 10 minutes during the reaction, the branch number increased from ca. 2 to ca. 4 branches. . 155

Figure 5.11: Two increases in radical generation for EPPS AuNS. (a) 2 LSP peaks (λ_1 - filled and λ_2 - open) and radical concentration over the reaction. Two increases in radical intensity occur

at t_1 and t_2 . **(b)** TEM images of the quenched growth at 5, 15, 30, 40, 60, and 75 min. **(c)** The percentage of particles with no branches (spheres), short branches (< 30 nm), or long branches (≥ 30 nm) at different time points during the reaction. 157

Figure 5.12: Low magnification images of quenched EPPS AuNS. Zoomed-out TEM images of 500 mM HEPES AuNS in the growth solution quenched at **(a)** 5, **(b)** 15, **(c)** 30, **(d)** 40, **(e)** 60, and **(f)** 75 minutes. The scale bars for (a) and (b) are 40 and 50 nm, respectively, due to the small size of the particles. All remaining scale bars are 100 nm. These images demonstrate the change in particle shape over the EPPS AuNS reaction. A significant increase in branch length occurs between (c) 30 and (d) 45 minutes..... 158

Figure 5.13: Average branch length, particle volume, and branch length of EPPS AuNS. 500 mM EPPS + HAuCl₄ was quenched at 5, 10, 15, 20, 25, 30, 40, 45, 50, and 60 minutes with PEG. Using ImageJ, particle morphology was analyzed at each time point based on ≥ 300 particles. **(a)** The average branch length increased to ca. 12 nm during the first 30 minutes of the reaction. The branch length increased significantly to ca. 30 nm between 30 and 40 minutes. The error bars increased between 30 and 40 minutes, because not every particle branch length increased, which created a greater distribution of branch length. **(b)** The average particle volume grew steadily up to 50 minutes. Initially, during the first 30 minutes, the particle volume was due to an increase in branch number. After 30 minutes, the increase in particle volume was due to an increase in branch length. **(c)** During the reaction, from 5 to 30 minutes, the branch number increased from ca. 1 to ca. 3 branches, and remained around 3 – 4 for the remainder of the reaction. The standard deviation of branch number was due to particle heterogeneity. 159

Figure 5.14: Radical generation depends on buffer concentration and type. (a) HEPES and (c) EPPS radical intensity at 3 different [buffer]. Each line scan is offset by 40 (a.u.). A dashed line was placed at 20 min to distinguish the relative radical increases at t_1 and t_2 . Thinner dashed lines demonstrate the temporal shift for t_2 of different [EPPS]. Corresponding TEM images of AuNS quenched at different time points during the reaction (in the upper LH corner of each image) for (b) HEPES and (d) EPPS..... 161

Figure 5.15: Radical generation depends on buffer concentration and type. (a) HEPES and (b) EPPS line scans at 5 different [buffer] (100, 250, 500, 750, and 1000 mM). Green and pink radical scans represent additional concentrations to demonstrate the trend continuity. Each line scan is offset by 30 (a.u.). HEPES AuNS only produced a significant second rise at 250 and 500 mM. EPPS AuNS produced a second rise of varying intensities at varying times..... 162

Figure 5.16: LSP peak shift during the AuNS reaction. (a) HEPES AuNS formed 1 LSP peak for all concentrations except for 500 mM which formed 2 LSP peaks. For concentrations > 500 mM, the absorbance spectra did not have any defined peaks (Fig. S1). (b) EPPS AuNS > 100 mM had absorbance spectra with 2 LSP peaks. 163

Figure 5.17: Morphological evolution of HEPES AuNS through *in situ* TEM using a SiN cell. (a) HEPES interacting with a high-kV caused large artifacts in the cell, which preventing imaging of the AuNS. (b) After direct deposition of the growth solution, images of AuNS at 5, 25, and 45 minutes were taken. (c) Two snaps of a movie collected of the growth solution *in situ*, spaced 1.2 seconds apart. The movement of the particles in solution was too rapidly to allow for imaging of one particle over an extended time period. 166

Figure 5.18: Crystallographic structure of initial HEPES particles. (a) Initial particle formation during the first 5 minutes of the reaction. (b) HR-TEM images were taken of initial particles during the AuNS growth reaction in a liquid graphene cell. The lattice spacing (d) was determined through FFT analysis. The FFT (inset) was taken from the area outlined with a dotted white box. The initial particles had twinned boundaries (solid white line) between the $\langle 111 \rangle$ direction. 168

LIST OF TABLES

Table 2.1: Molecular structure of Good’s buffers (HEPES, EPPS, MOPS, and MES).

Molecular structure of HEPES and EPPS, containing a piperazine ring and a hydroxyl group, and MES and MOPS, containing a morpholine ring. HEPES and MES have an ethane sulfonate group, where EPPS and MOPS have a propane sulfonate group with an additional carbon (dashed circle).
 62

Table 2.2: AuNS particle size at the highest R_{buffer} ratio. The overall particle size was measured

through DLS and branch length was measured by analyzing TEM images through ImageJ. Approximately 200 – 250 branches were measured manually to obtain the average branch length. Representative images were taken across the entire TEM grid. 66

Table 3.1: Particle size, average branch length, and percentage of spherical particles at

different time points. The overall particle size was measured using DLS and branch lengths were measured through analysis of TEM images. ≥ 500 branches were measured manually to obtain average branch length. Representative images were taken across the entire TEM grid. At initial time points, larger particles (> 80 nm) remained in solution, with an average branch length 45 ± 9 nm. At longer time points (30 days), particle size decreased by 35 ± 10 nm, and branch length shortened by 20 ± 4 nm compared to the day-1 solution. Additionally, spherical particles percentage increased from 35% to 54% over 30 days, which was corroborated by an increase in the 520-nm LSP peak. 94

CHAPTER 1:
INTRODUCTION TO SYNTHESIS
OF GOLD NANOPARTICLES

1.1 Introduction to Noble Metal Nanoparticles

1.1.1 Historical Background

Nanotechnology, particularly the development of novel nanomaterials with desirable properties, has accelerated significantly in the last few decades. During this period, the explanation of the relationships between structure and function has opened new areas of applications for nanomaterials. The use of these materials on the nanoscale, however, predates our understanding of their structure-function relationships. For example, noble metals have been used dating back to the Vedic period of ancient India; the presence of gold bhasma – gold particles containing ashes – were prepared for medicinal purposes.¹ Ancient Egyptian cultures used gold for mental, physical, and spiritual cleansings. Drinkable, soluble gold in a slightly pink solution, characteristic of gold nanoparticles, was hailed in medieval Europe for having curative properties for several diseases.² Outside of medicinal purposes, the oldest well-documented example of nanoparticles is their utilization for decorative purposes in glass ware, ceramics, and pottery coloration (e.g. the pink pigment created from gold nanoparticles known as Purple of Cassius).³ A famous, existing example is the Lycurgus cup, a Roman artifact from the 4th century A.D. (**Figure 1.1**).⁴ The composition is similar to modern day glass but with small amounts of gold and silver nanoparticles. Due to these nanoparticles, the cup presents different colors in reflected (green) and transmitted (red) light. Due to this aesthetic quality, nanoparticles were a standard inclusion in stained glass for cathedral windows throughout medieval Europe. While many early scholars understood and theorized the concept of “solutions containing gold in the finest degree of subdivision,”⁵ very few formal studies systematically explored the nature of nanoparticles until Michael Faraday.

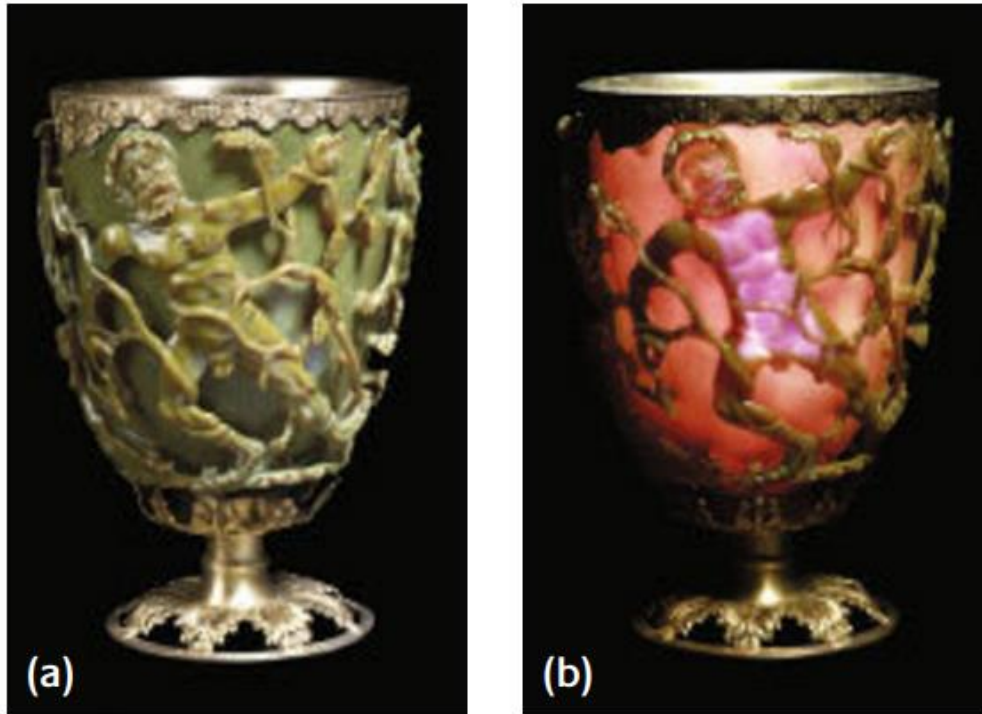


Figure 1.1: Photographs of the Lycurgus cup. The Lycurgus cup in (a) reflected and (b) transmitted light. Adapted from the Department of Prehistory and Europe, The British Museum, Higgit *et. al.*⁴ with permission under the Creative Commons CC-BY license as published through Springer Nature.

In 1857, Faraday conducted one of the first scientific experiments to explore the properties of nanoparticles.⁶⁻⁷ He synthesized gold colloids in solution which created gold seeds known as “sols.” He found that nanoparticle size changed due to the addition of different salts at varying concentrations. Notably, he recognized that the characteristic color change to ruby-red was due to the size of the gold particles and not due to any additional chemicals or materials. Furthermore, he discovered that the different sized gold nanoparticles suspended in solution had different colors due to their light scattering properties, called the Faraday-Tyndall effect. Although Faraday could not wholly explain the origin of these optical properties, his seminal work created a field of structure-function nanoparticle studies that have continued till this day.

Our understanding of noble metal nanomaterials unique properties has since increased due to the advancement of modern techniques, enabling analysis of single, distinct nanoparticles rather than the entire ensemble. Particularly, the visualization of nanoparticles through transmission electron microscopy (TEM)⁸ coupled with studies of their optical properties have deepened our understanding of the structure-function relationship of nanoparticles. Recent studies show that the optical properties of nanoparticles can be explained by the physical phenomena of localized surface plasmon (LSP) resonances. LSP occurs in small nanoparticles due to the oscillation of surface plasmons (coherent delocalized electrons) which have been excited by light (**Figure 1.2**).⁹ The LSP of gold nanoparticles is in the visible light range (400 – 700 nm). Due to this LSP wavelength, gold nanoparticles absorb visible light, resulting in the bright colors exhibited by the solutions. These properties cause gold nanoparticles to be extensively exploited for many applications. These properties are dependent on the size and shape, which is not the case for their corresponding bulk materials. Understanding the fundamental structure-

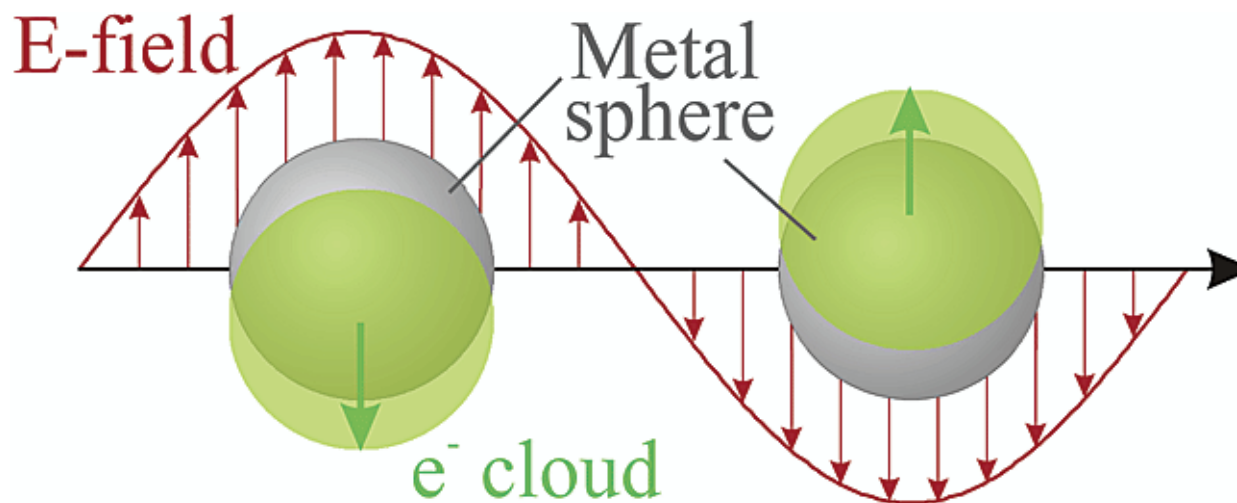


Figure 1.2: Scheme of localized surface plasmons for metal nanoparticles. Schematic of plasmon oscillation for a sphere, showing the displacement of the conduction electron charge cloud relative to the nuclei. Adapted with permission from Schatz *et. al.*⁹ Copyright 2003 American Chemical Society.

function relationship and developing the synthetic techniques to tune desirable properties have accelerated the number of applications for nanoparticles.

1.1.2 Applications of Metal Nanoparticles

Metal particles with nanometer-scale dimensions demonstrate tunable properties distinct from their bulk form, which has enabled numerous, wide-ranging applications including catalysis, therapeutics, bioimaging, sensing, and nanoelectronics. For a metal at room temperature, the mean free path of an electron is on the order of 10 – 100 nm and as the particle approaches this size, unusual effects are observed.^{5, 10} For example, gold nanoparticles of a diameter ≤ 3 nm are no longer inert and can catalyze chemical reactions quickly, unlike their bulk counterparts.¹¹⁻¹² These gold nanoparticles can oxidize extremely toxic CO into a less toxic CO₂ efficiently and quickly, which illustrate just one of many potential applications of this property. Many factors play a role in the catalytic rates of nanoparticles, among which are shape, crystal structure, and composition.

Noble metal nanoparticles such as gold and silver have long been used for therapeutic applications and more recently their use has been extended to other biomedical applications as a result of their low cytotoxicity and high biocompatibility *in vivo*.¹³ The surface of these nanoparticles provides an easy template for functionalization with various biological molecules, such as aptamers used for targeting and delivery of therapeutic drugs to cancer cells.¹⁴ Furthermore, nanoparticles have tunable LSP wavelengths in the NIR region, which is where blood and tissues are relatively transparent to irradiation.¹⁵ Additionally, the strong LSP of metal nanoparticles allows for imaging of individual particle locations with the advent of advanced optical microscopy techniques, such as dark-field and two-photon luminescence microscopy.¹⁶⁻¹⁷ Specifically, for anisotropic nanoparticles, NIR absorption and photothermal effects allow for dual therapy as well

as imaging functionality, which has been demonstrated for nanorods, nanocages, and nanostars.¹⁸⁻
¹⁹ Additionally, colloidal gold particles have been used as contrast agents for electron microscopy because of their electron-dense nature. This use as a contrast agent has now expanded into optical imaging and sensing applications, which rely on the elastic light scattering properties of metal nanoparticles.²⁰⁻²⁵

In addition to functional ligands that bind to nanoparticles for biomedical purposes, certain molecules that adsorb to the surface of metal nanoparticles undergo surface-enhanced Raman scattering (SERS) effects because of the coupling of the plasmon band of the irradiated metal with the electronic states of the molecule.²⁶⁻²⁸ Thus, one emerging application of metallic nanoparticles is single-molecule detection through SERS.²⁹⁻³⁰ Surface-enhanced fluorescence is also similar to SERS, although the molecule must be 10 – 100 nm away from the metal surface to prevent quenching.³¹⁻³³ Metal nanoparticles have been used to detect trace amounts of pesticides,³⁴⁻³⁵ biomolecules,³⁶⁻³⁷ viruses,³⁸⁻³⁹ glucose,⁴⁰⁻⁴² or DNA⁴³⁻⁴⁵ among many other molecules.

Gold and silver nanoparticles have been used for optical applications as well, including optical communications and information processing. Optical nonlinearity, as explored through the Z-scan technique, has been demonstrated for nanoparticles composed of a single-material⁴⁶ as well as alloys containing two metals.⁴⁷ The nanoparticles behave as saturable absorbers or reverse saturable absorbers, depending on the excitation. Thus, they can be used in logic gating and pattern recognition in optical computers.

Size and shape direct the physical and chemical properties of noble metal nanoparticles; thus, creating studies on how to optimize these structural parameters for a variety of potential applications is crucial. To address this need, many systematic studies have been dedicated to

develop methods to produce monodisperse noble metal nanoparticles with a desirable size and shape, in particular those composed of gold.

1.2 Structure and Morphology of Gold Nanoparticles

Variations in properties of matter at the nanoscale is one of the most fascinating aspects of nanoscience. Properties of gold nanoparticles can be varied by altering the size, shape, aggregation, and local environment. This dissertation will focus on the factors that control the size and morphology of gold nanostars (AuNS) and specific applications of these particles. Before delving into the synthetic factors and fundamental mechanism, a framework for elucidating nanoparticle morphology will be explored.

Two main factors control nanoparticle size and shape: crystal structure and surface facets. Crystal structure develops during particle nucleation and formation, and the surface facets are defined during particle growth.⁴⁸ Nanoparticles can either be monocrystalline (no defects), polycrystalline (many defects), or contain a distinct number of defects. Monocrystalline particles are difficult to synthesize because defects are common in metallic particles (**Figure 1.3a**). The most common defect in FCC (face-centered cubic) metals, such as gold, is a twin defect (**Figure 1.3b-c**), since the energy barrier for their formation is low.⁴⁹ A specific type is a crystal twin defect where two distinct crystals have overlapping lattice points in a symmetrical way. For gold nanoparticles, many twin defects can occur in a single particle, particularly for spherical nanoparticles that are often used as seeds. For spherical Au nanoparticles, penta-twinned (5 twin boundaries from one central point) and multiply-twinned (intersection of many twin planes) are the most common (**Figure 1.3d-f**). The final morphology of the resulting nanoparticle is defined

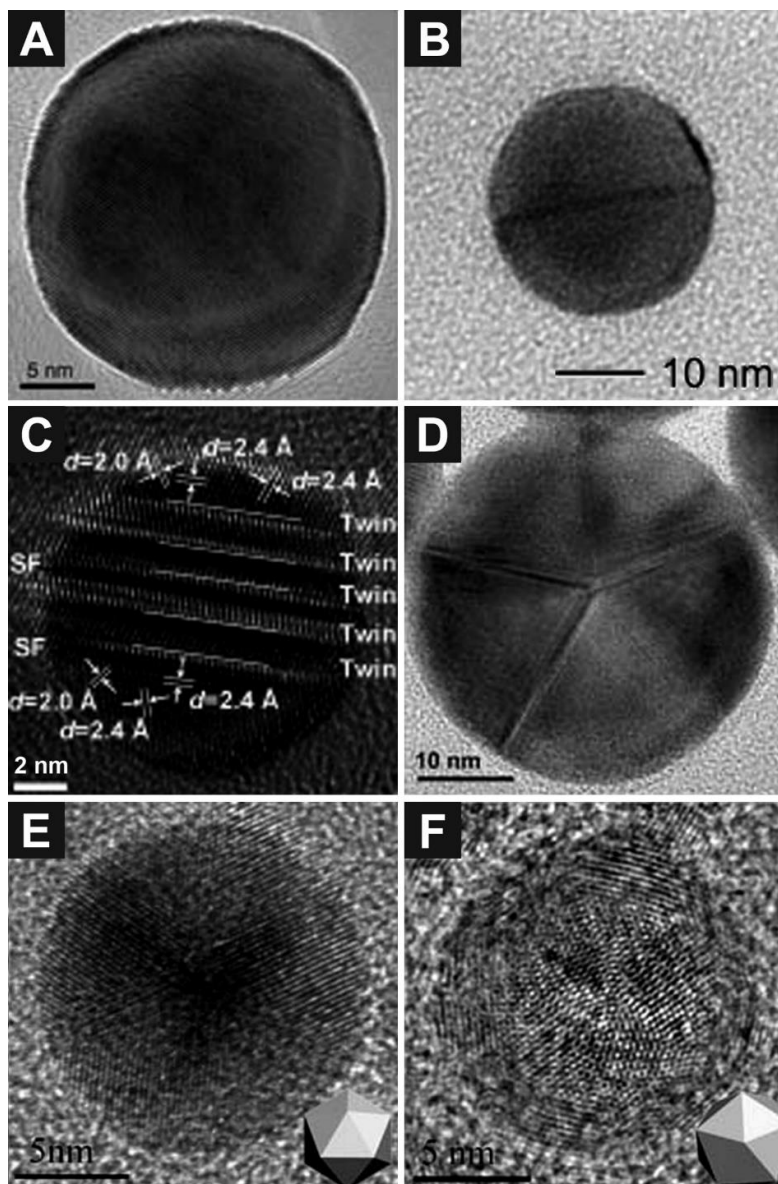


Figure 1.3: HR-TEM images of spherical noble metal nanocrystals with different crystal structures: (a) a single-crystalline, (b) a singly twinned, (c) a multiple planar-twinned, (d) a cyclic penta-twinned gold, and (e, f) a multiple-twinned icosahedral gold nanocrystal. Adapted with permission from Xu *et. al.*⁵⁰ Copyright 2011 American Chemical Society.

not only by the crystal structure (i.e. defects) formed during the nucleation phase but also the surface structure.

A metal nanoparticle has exposed surfaces with a specific arrangement of atoms, named facets. The structure of these atoms changes based on the alignment of the exposed surface arrangement compared with the lattice structure of the FCC unit cell for gold. These facets can be defined through Miller indices, a notation system for planes determined by three integers ($\{h\ k\ l\}$) all consisting of either 0 or 1. For gold, three low index facets exist: $\{111\}$, $\{100\}$, and $\{110\}$. In particular, $\{111\}$ has a closed-packed arrangement of atoms and is the most thermodynamically favorable.⁵¹ Several approaches, such as physical templating⁵² and kinetic control,^{48,53} have been developed to favor growth on specific facets. The directed growth of exposed facets coupled with the defects created during the nucleation phase leads to the final nanoparticle morphology.

1.2.1 Size

Nanoparticles are of particular interest because their optical properties can be tuned depending on their size, unlike the bulk form. Specifically, for small (≤ 30 nm) spherical gold nanoparticles, the LSP absorbs light in the blue-green portion of the spectrum (ca. 500 nm) while red light (ca. 700 nm) is reflected. Due to these optical properties, the characteristic color of spherical gold nanoparticles is a rich-ruby color, first systematically studied by Faraday (**Figure 1.4a-d**). As the particle diameter increases, the peak LSP wavelength, related to the optical absorption, shifts to longer wavelengths. As this increase occurs, more red light is absorbed as blue light is reflected which produces solutions with a pale blue or purple color. For spherical nanoparticles, the particle size reaches a bulk limit where the wavelengths move into the IR portion of the spectrum and most visible wavelengths are reflected, which corresponds to a clear or translucent color. This

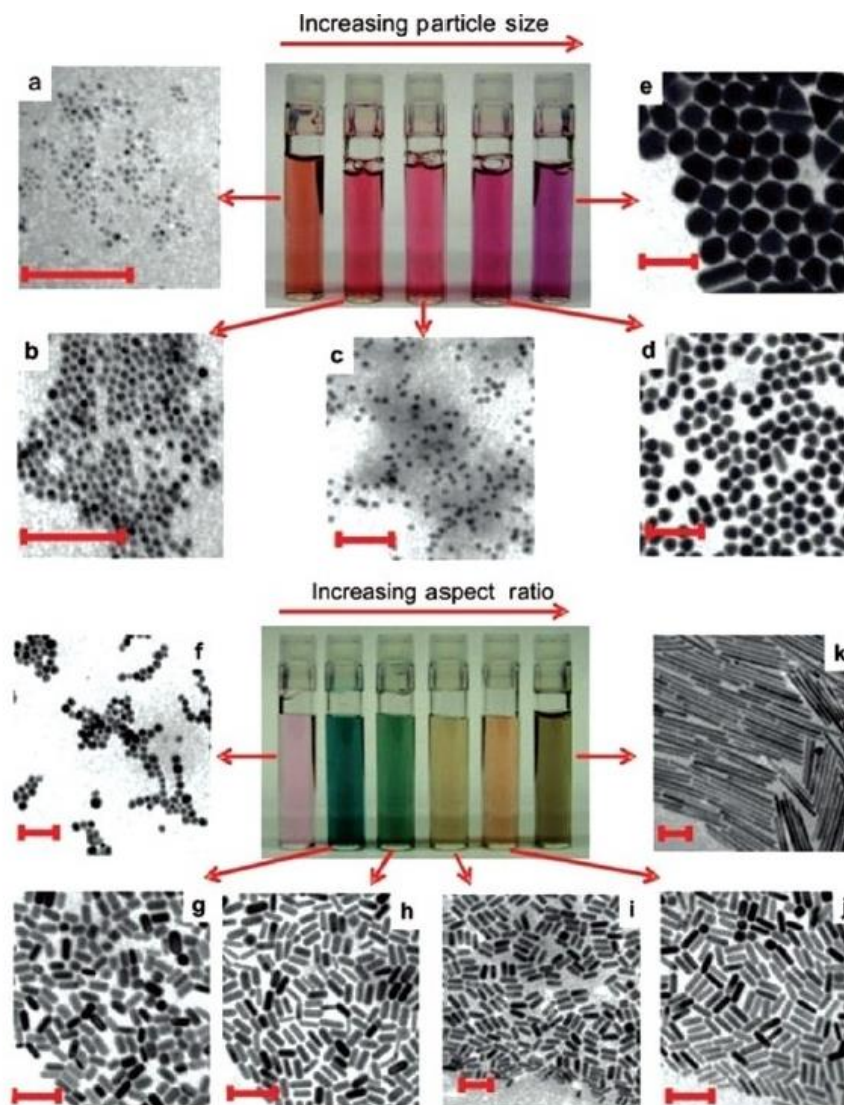


Figure 1.4: Photographs of aqueous solutions of gold nanospheres (4- 40 nm, top) and gold nanorods (bottom) as a function of increasing dimensions. Corresponding TEM images of the nanoparticles are shown (all scale bars 100 nm). For the nanorods, the aspect ratio varies from 1.3 to 5 for short rods (TEMs f-j) and 20 (TEM k) for long rods. Adapted with permission from Mody *et. al.*⁵⁴ Copyright 2010 American Chemical Society.

absorption shift is also observed when excess salts are added into the gold solution. The surface charge of the nanoparticles changes from slightly negative to neutral, which causes the nanoparticles to aggregate in solution, resulting in a color change from red to blue. Gold nanoparticles have a versatile surface chemistry and can be functionalized with small molecules, which prevents aggregation. Changing only the size of spherical gold nanoparticles, however, allows for minimal tunability in their optical properties.

1.2.2 Shape

In the past twenty years, many advances in synthetic techniques of non-spherical gold nanoparticles, especially nanorods, have paved the way for even more promising applications because of their unique properties. Specifically, gold nanorods have two LSP peaks — one in the visible and another in either the visible or near-infrared (NIR) range — which correspond to the short axis (transverse) and long axis (longitudinal) of the nanorod.^{9-10,55-57} These peaks are tunable depending on the dimensions of the nanorods. Therefore, gold nanorods can be synthesized at specific aspect ratios that correspond to the absorption of light at certain wavelengths in the visible and NIR (**Figure 1.4f-k**).

This dissertation will focus on AuNS, which are of particular interest among anisotropic nanoparticles. Since shape modifications, such as number of branches, aspect ratio, and length of branches⁵⁸ enable tunability of the position and number of LSP resonances.⁵⁹⁻⁶¹ Strong electric field enhancements can occur on multiple sharp tips of AuNS,⁶² making them high-performing substrate materials for a variety of applications.^{14,59,63-67} Additionally, regions of negative curvature between the branches can alter the physicochemical properties of molecules tethered to the Au

surface (e.g. For example, the relaxivity of a Gd(III)-based MRI contrast agent was tripled when bound to the surface of AuNS compared to spherical nanoparticles).⁶⁸

1.3 Overview of Synthetic Approaches for Anisotropic Gold Nanoparticles

For anisotropic nanoparticles, the size and shape dependence of the physical and optical properties make them useful in current materials research. To create particles with desirable properties, specialized synthetic strategies are needed to enable precise control over size and shape of particles. Chemically growing either bulk or nanometer-sized materials involves precipitation of a solid phase from solution. Fundamental understanding of the mechanism underlying this precipitation can improve the engineering of the nanoparticle growth to the desired size and shape.

A certain solubility for a solute exists for any given solvent. If excess solute is added into the solvent, nucleation and formation of nanocrystals will occur. Therefore, to induce nucleation and synthesize nanoparticles, the solution needs to be supersaturated either by (1) dissolving a high concentration solute at a high temperature and then cooling the solution; or (2) producing a supersaturated solution with the required precursors during the growth stages. After precipitation and nucleation, the nanoparticle growth stage occurs. The nucleation and growth stages can occur in two ways: (1) a multi-step, seed-mediated process or (2) a one-pot, seedless method.

1.3.1 Seed-Mediated Synthetic Methods

In seed-mediated growth, the conditions for nucleation and growth are dissimilar and thus the process is usually done through a multi-step process. A simple reaction usually involves a two-step process: (1) preparation of isotropic seeds and (2) addition of the seeds to a growth solution containing a shape-directing agent (**Figure 1.5**).

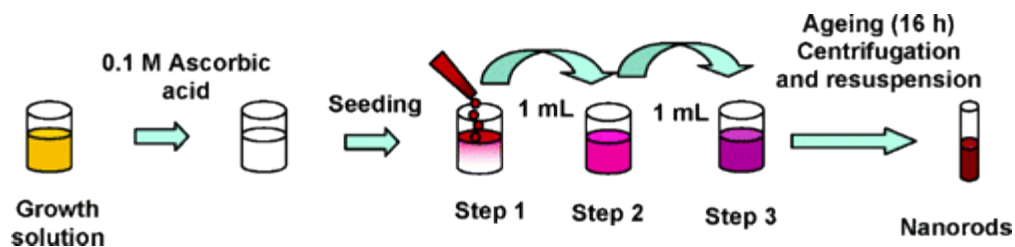


Figure 1.5: General methodology for the generation of gold nanorods. Adapted with permission from Murphy *et. al.*⁶⁹ Copyright 2004 American Chemical Society.

A simple reduction of metal salts by reducing agents in a controlled fashion generally produces spherical nanoparticles, because spheres are the most thermodynamically favorable shape. Some of the most well-known and frequently used methods to synthesize spherical gold nanoparticles include: (a) the Turkevich method involving the reduction of gold chloride by citrate;⁷⁰⁻⁷¹ (b) the related Frens method;⁷² and (c) the Brust method in 1994 involving gold ions reduced with borohydride.⁷³ Nucleation of spheres requires high chemical supersaturation, allowing for indiscriminate growth of all crystal facets creating a relatively isotropic, uniform spherical seed.⁷⁴ When the size of the aggregates reaches a critical threshold (ca. 2 nm), a nucleus of gold atoms is formed, most of which are not monocrystalline but twinned.⁷⁵ This structure forms when two 1-nm seeds coalesce to form a single particle and grow in all directions into a larger particle. These isotropic, twinned nanoparticles are used as a precursor for anisotropic particle growth. After the seeds are fully formed, the reaction conditions are altered to create anisotropic particles either by introducing more gold salt with a different reductant or by adding a shape determining surfactant.

The directed growth of seed nanoparticles into the desired morphology happens in the shape-directing solution, which contains excess metal ions, a surfactant, and a mild reducing agent. Enough reducing agent is added to reduce the gold salt to an ionic phase but not enough to nucleate particles without the seed. The key to developing anisotropic particles instead of even larger spherical particles is the use of a shape-directing agent, such as cetyltrimethylammonium bromide (CTAB).⁷⁶⁻⁷⁷ The shape-directing agent promotes anisotropic growth in one crystallographic direction by preferentially binding to certain crystal facets.⁷⁸⁻⁷⁹ Due to the presence of the surfactant, only certain facets of the seed are bare, which facilitates the reduction of the metal salts preferentially

onto the surface of the exposed seeds causing directed growth. Additional reagents, such as silver nitrate, are used during nanoparticle synthesis to increase the yield of anisotropic particles.⁸⁰

Of anisotropic gold nanoparticles, nanorods are the most commonly used and have an established protocol to tune the size and shape as explored by Murphy^{69, 76, 81-83} and El-Sayed.^{79, 84-86} Since the synthetic process of nanorods has been widely established and fundamentally studied, nanorods are a useful model system to understand the mechanism for directed growth in seed-mediated synthesis. For nanorods, sodium borohydride (NaBH_4) reduces gold to form seeds in the nucleation solution and, in a separate solution, CTAB preferentially binds to the {110} facet of the seeds causing directed growth in the [111] direction.⁷⁹ Noble metal nanoparticles of diverse structures – rods, wires, triangles, stars, and flowers – can be synthesized using the seed-mediated method as well.⁸⁷ A disadvantage to many seed-mediated syntheses is that the strongly-bound surfactants create a highly cytotoxic bilayer,⁸⁸⁻⁹⁰ which is challenging to replace with other functional ligands.^{89, 91} Additionally, seed purity determines the quality of the resulting structures.

1.3.2 Seedless Synthetic Methods

Anisotropic gold nanoparticles can also be synthesized by “seedless” methods, where the reducing agent, shape-directing agent, and gold salt (HAuCl_4) are added to one pot, and the nucleation and directed growth occur simultaneously. These syntheses require fewer precursors and steps and can result in morphologies beyond those of polyhedral or perfectly symmetrical geometries, such as concave gold nanocrystals.^{61, 92 93}

Jana and Pradeep separately showed that gold nanoparticles can be formed without seeds. Jana demonstrated that monodisperse gold and silver nanorods, spheroids, nanowires, platelets, or cubes of 4 – 50 nm dimension and controllable aspect ratio can be prepared by introducing a mixture of

strong and weak reducing agents into the micellar solution of a metal salt without using seeds.⁹⁴ Here, the strong reducing agent initiates nucleation and the weak reducing agent induces the nanoparticle growth. Pradeep found that addition of a calculated amount of NaBH₄ directly into the growth solution leads to the formation of uniform gold nanorods. They hypothesized that the addition of NaBH₄ led to *in situ* formation of the seed particles, which enabled the growth of gold nanorods.⁹⁵ Variations on seedless syntheses, such as tuning the type and concentration of precursors, pH, temperature, and stirring speeds have been used to produce a wide variety of anisotropic shapes, such as AuNS.^{58, 96-100}

1.3.3 Seedless Synthesis of Gold Nanostars

In this dissertation, the anisotropic nanoparticles studied are AuNS synthesized through a seedless reduction of HAuCl₄ by a Good's buffer — e.g., 4-(2-hydroxyethyl)-1-piperazineethanesulfonic acid (HEPES).^{58, 96, 100} HEPES contains three chemical moieties: a hydroxyl, an alkane sulfonate, and a nitrogen-centered piperazine ring. Due to this combination of groups, HEPES acts as both the reducing and shape-directing agent. When exposed to HAuCl₄, the two tertiary amines of HEPES reduce Au(III) ions to Au(0) and produce nitrogen-centered cationic free radicals.¹⁰¹⁻¹⁰² The ethane sulfonate group of HEPES preferentially directs the growth of the branches along the [111] direction.¹⁰³ Additionally, the weakly-bound ethane sulfonate group of HEPES and the hydroxyl group facilitate self-assembly and bilayer formation via hydrogen bonding to allow for shape stability.¹⁰³ Due to this simplistic, two-precursor synthetic approach, the preparation of AuNS is highly scalable and we have demonstrated the preparation of multiple liter batches within 30 minutes.¹⁰⁴

An advantage of the AuNS synthesized with Good's buffers is that they can be easily functionalized with a variety of ligands through Au-thiol chemistry. We and others have demonstrated that biomolecules, such as DNA and proteins, can be conjugated to AuNS.^{60, 68, 104-107} Good's buffers are biologically compatible and gold is inherently inert, resulting in AuNS that do not elicit a toxic response *in vivo*. Also, this synthesis technique results in a negative surface charge on the nanoparticles, mitigating aggregation.¹⁰⁸ Finally, compared to conventional convex particle geometries, such as spheres and nanorods, multi-branched AuNS have unique 3D geometries with multiple sharp tips and concave features.¹⁰⁰ Thus, structure-property relationships of AuNS are interesting to study for a variety of applications such as imaging,^{68, 92, 109} sensing,¹¹⁰ and photothermal effects.^{58, 92}

1.4 Dissertation Overview

This dissertation strives to provide an enhanced understanding of the chemical and physical factors which control the seedless growth of anisotropic AuNS. Additionally, we study the effect of final AuNS morphology on the ligand distribution by single-particle analysis. The study of how nucleation and directed growth occur in one pot can contribute to the fundamental understanding of the synthetic factors affecting the growth of the nanoparticles, which will allow for tunability of nanoparticle with a desired shape and size for applications.

Chapter 2 reported the synthetic factors affecting the seedless growth of AuNS synthesized with Good's buffers. Through exploration of mechanical agitation, concentration ratio, buffer type, and pH of the solution we tuned branch length, branch direction, and overall size of AuNS. The overall homogeneity of the solution increased and the percentage of unwanted spherical by-products was reduced by stirring at a high-speed during the growth reaction. Varying the buffer

concentration changed the overall size and branch length of the AuNS, which lead to tunable LSP resonances from visible to NIR. The size and stability were dramatically affected by the pH of the growth solution. Furthermore, the two distinct alkane sulfonate groups of the Good's buffers induced branched growth in different crystallographic directions. The synthetic insights of this chapter created set of design considerations for controlling the growth and final shape of AuNS prepared by seedless syntheses. This work represents the first reported synthesis of anisotropic gold nanoparticles synthesized with a Good's Buffer containing a morpholine ring.

Chapter 3 describes a strategy to obtain highly homogenous populations of AuNS by combining stabilization and sorting processes. After establishing that a morpholine-based buffer induced anisotropic growth, additional challenges needed to be addressed, specifically homogeneity and stability. We improved the stability over time and reduced the percentage of by-products by adjusting the storage conditions. By centrifuging the as-synthesized, unsorted mixtures through a sucrose density gradient, we isolated AuNS based on branch length and number. We demonstrated that only a single round of post-synthetic density gradient centrifugation (DGC) separation was necessary to sort AuNS efficiently by size and shape. Any additional rounds of DGC did not significantly improve separation. This work demonstrated certain fundamental limits of separation for rate-zonal DGC.

Chapter 4 used this optimized DGC strategy to obtain homogeneous AuNS to determine how particle curvature affected steric and conformational hindrance of ligands. Time-of-flight secondary ion mass spectroscopy was used to precisely quantify the number and position of ligands on non-spherical nanoparticle surfaces in different regions of curvature (positive, negative, or neutral). AuNS with a medium density of branches (3 – 5) showed the highest amount of DNA

loading. As the number of branches increased beyond this, the negative curvature where the branch meets the core sterically hindered the attachment of additional DNA. Direct, simultaneous measurements of an inorganic core and unlabeled-ligands was achieved on the single particle level for the first time.

Chapter 5 further probed the fundamental mechanism of the seedless synthesis of anisotropic AuNS. We identified the reaction through radical generation *in situ* based on electron paramagnetic resonance spectroscopy. The radical trend was correlated to ensemble optical properties and single particle morphology. Depending on buffer type and concentration, one or two increases in radical intensity occurred, which corresponded to the initial particle formation and an increase in branch length, respectively. Thus, the radical intensity trend is an indicator of the resulting nanoparticle shape and properties. We revealed insights about the seedless growth mechanism of AuNS and developed a robust way to study the mechanism of growth for nanoparticles.

This dissertation significantly enhanced the understanding of the seedless synthesis mechanism, post-synthetic separation, and ligand distribution for anisotropic gold nanostars. This work represents an important step toward the fundamental understanding of directed synthesis of gold nanoparticles. Additionally, the effect of shape on ligand distribution will greatly impact future design criteria for nanoparticles. This, in turn, can enable the direct synthesis of a range of desirable nanoparticle shapes and expand their applications.

CHAPTER 2:
MANIPULATING THE ANISOTROPIC STRUCTURE
OF GOLD NANOSTARS USING GOOD'S BUFFERS

This chapter is based, in part, on the research described in the following publication:
Chandra, K.; Culver, K.S.B.; Werner, S.E.; Lee, R.C.; Odom, T.W.; Manipulating the
Anisotropic Structure of Gold Nanostars using Good's Buffers. *Chemistry of Materials* **2016**, 28
(18) 6763-6769

2.1 Introduction

Anisotropic gold nanoparticles (Au NPs) have plasmon resonances that can be tuned by their size and morphology.¹¹¹ The seed-mediated synthesis of anisotropic Au NPs, such as nanorods or nano-bipyramids,⁷⁹⁻⁸⁰ typically begins with the nucleation of isotropic seeds^{74, 112} that are then added to a separate solution containing shape-directing agents. In contrast, seedless syntheses can create anisotropic particles where both nucleation and directed growth occur in a one-pot solution.^{96, 113} These syntheses require only two precursors and can result in Au NP morphologies beyond those of polyhedral or perfectly symmetrical geometries, such as concave Au nanocrystals.
61, 92-93

Gold nanostars (AuNS) are of particular interest among anisotropic NPs because shape modifications, such as number of branches, aspect ratio, and length of branches⁵⁸ have enabled tunability of the position and number of localized surface plasmon (LSP) resonances.^{59-61, 97} Strong electric field enhancements can occur on multiple sharp tips of AuNS,⁶² making AuNS high-performing substrate materials for SERS,^{59, 63-65} photothermal therapy,^{66, 14} and photoacoustic imaging.⁶⁷ Additionally, the regions of negative curvature between the branches can alter the physicochemical properties of molecules tethered to the Au surface. For example, the relaxivity of a Gd(III)-based magnetic resonance imaging contrast agent was tripled when bound to the surface of AuNS compared spherical NPs because of the elongated residence times of water near the Gd(III).⁶⁸

The most commonly used seedless synthesis method for AuNS involves two precursors: gold salt (HAuCl_4) and a biocompatible Good's buffer, e.g. 4-(2-hydroxyethyl)-1-piperazineethanesulfonic acid (HEPES).^{58, 60, 96} AuNS synthesized with Good's buffers do not

require additional surfactants for stabilization and are thus easy to functionalize^{60, 107} compared to anisotropic particles prepared by strongly bound surfactants such as CTAB.^{76, 89, 91} HEPES buffer acts as both a reducing and shape-directing agent to produce AuNS. In the presence of H₂AuCl₄, the two tertiary amines of the piperazine group in HEPES create cationic free radicals that can reduce Au ions and lead to the formation of NPs.^{101-102, 114} The alkane sulfonate group in HEPES has been proposed to facilitate the anisotropic growth of branches.¹⁰³ Another Good's buffer with a piperazine ring, 4-(2-hydroxyethyl)-1-piperazinepropanesulfonic acid (EPPS), has also been used to synthesize AuNS with sizes similar that of HEPES AuNS.^{103, 115} Although Good's buffers with a morpholine ring, such as 2-(N-morpholino)ethanesulfonic acid (MES) and 3-(N-morpholino)propanesulfonic acid (MOPS), have been able to reduce Au ions via radical formation to produce spherical NPs,¹⁰¹⁻¹⁰² they have not yet demonstrated shape-directing properties.

Other factors that affect the growth of seedless Au NPs include the concentration ratio of the precursors, pH of the growth solution, and mechanical agitation or stirring.^{58, 61, 116-117} Changing the concentration of either the buffer or H₂AuCl₄ can tune particle size and shape.^{58, 114} Adjusting the pH of the growth solution can affect the yield of anisotropic Au NPs and the colloidal stability of particles.⁸² Additionally, stirring the growth solution can uniformly distribute the precursors.¹¹⁸ High-speed stirring has improved the yield and homogeneity of seed-mediated Au nanorods;¹¹⁸ however, agitation and stirring are typically avoided in seedless AuNS synthesis.^{58, 96, 115} AuNS have only been synthesized with Good's buffers containing a piperazine moiety, but there have been no systematic studies on how to control this seedless, anisotropic growth.

Here we describe a seedless synthesis using Good's buffers that can tune branch length, branch direction, and overall size of AuNS. Mechanical agitation, concentration ratio, buffer type, and pH

of solution were the four parameters that were used to manipulate specific features of AuNS. We improved homogeneity and reduced the percentage of unwanted spherical byproducts by stirring the reaction. Changing the concentration ratio of Good's buffer to gold salt altered the overall size and branch length of AuNS, which lead to tunable LSP resonances from the visible to near-infrared wavelengths. We found that the size and stability of AuNS were also sensitive to the type of Good's buffer and pH during synthesis. By testing over the entire buffering range, we expanded the family of Good's buffers that could produce AuNS. Furthermore, the different alkane sulfonate groups induced branched growth in different crystallographic directions.

2.2 Results and Discussion

2.2.1 *Stirring During Synthesis Improved Yield of AuNS*

Previously, AuNS have been synthesized by adding HAuCl_4 to HEPES buffer ($R_{\text{HEPES}} = 700$ and pH 7.2) without stirring.¹⁰⁷⁻¹⁰⁸ Since varying buffer or HAuCl_4 concentration can tune the particles, we refer to the ratio R_{buffer} between the buffer to Au salt to demonstrate tunability. Although mechanical agitation has been explicitly avoided seedless syntheses,^{58, 92, 96} we found that AuNS could also be formed by shaking the solution after the addition of HAuCl_4 .¹⁴ **Figure 2.1** highlights the differences between stirred and unstirred reactions, where unstirred growth solutions produced heterogeneous AuNS shapes and ca. 15% spheres (**Figure 2.1a**). Thus, we systematically stirred the growth solution to study effects on AuNS formation. The growth solution was stirred at 200 – 1400 rotations per minute (RPM) based on protocols that have aided Au nanorod formation.¹¹⁸ We found that stirring for ≥ 1 minute improved the percentage of branched particles over spherical particles.

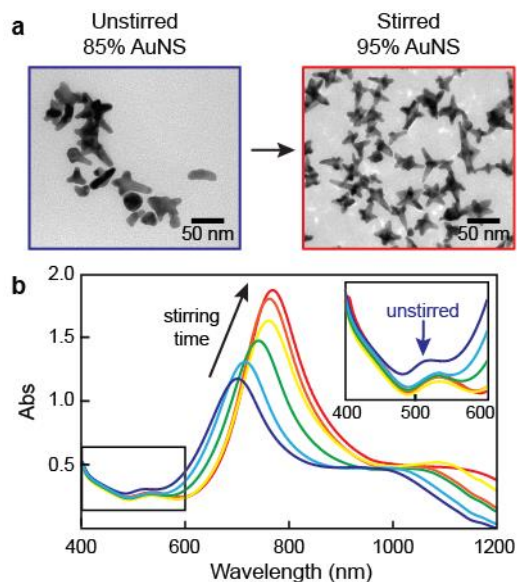


Figure 2.1: Stirring the reaction caused red shift in AuNS peak absorbance and improved yield of branched particles. (a) TEM images of HEPES AuNS that were unstirred (left) or stirred for 30 min at 200 RPM. **(b)** The absorbance spectra of HEPES AuNS that were unstirred (blue line) or stirred at 200 RPM from 1 (cyan line) up to 30 min (red line). The absorbance was measured 24 h after the reaction completed and indicated that increasing stirring time resulted in a red-shifted absorbance. The inset highlights the decrease in the peak near 500 nm corresponding to the spherical byproducts.

At the shortest time point of stirring (1 min) at the lowest speed (200 RPM), the solution had a 67% decrease in spherical by-products compared to the unstirred solution. The percentage of spheres was calculated by analyzing TEM images for ≥ 300 particles for each stirring time and stirring speed. The ensemble optical properties were compared to confirm the decrease in spherical by-products (**Figure 2.1b**), indicated by a reduction in absorbance near the LSP peak of spherical Au NPs (ca. 520 nm). Although the core of AuNS prepared by different methods has shown a weak LSP resonance around 520-560 nm,¹¹⁹⁻¹²¹ we found that the peak around 520 nm is primarily due to spherical NPs based on TEM analysis (**Figure 2.2**). This intensity decreased by half in AuNS solutions that had been stirred for only 1 minute, which demonstrated that even short periods of stirring decreased the number of spherical NPs (Figure 2.1b inset). Because as-synthesized AuNS exhibit heterogeneity, their ensemble absorbance spectra have broad spectral widths but still well-defined peaks at visible and NIR wavelengths. For HEPES AuNS, only one primary peak around 800 nm formed. With increased stirring time, regardless of stirring speed, a red shift in the peak absorbance occurred, and an overall increase in the percentage of branched NPs formed up until ca. 6 min of stirring (**Figure 2.3**). No clear increase in percentage of branched AuNS occurred, however, with increased stirring speed. We attribute this improved shape yield to the more uniform distribution of precursors at the initial stages of growth and to shear forces enhancing the branched growth.

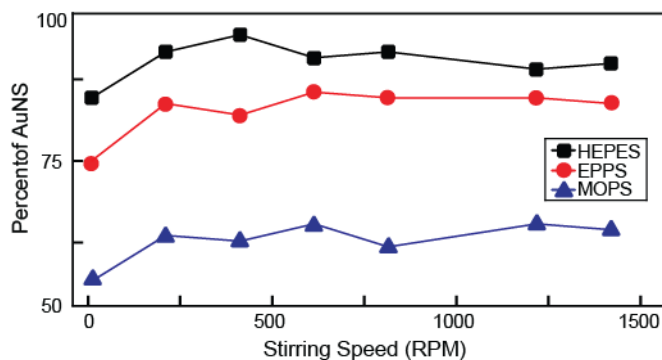


Figure 2.2: Percent of AuNS particles in solution increased with stirring speed. Growth solutions were stirred for 30 min at the designated RPM and then left in the dark overnight. TEM grids were made and particle analysis was conducted through ImageJ. For each stirring time point, 300 – 400 particles were measured. For all three buffers, an overall increase in the percentage of AuNS occurred. MOPS had the greatest heterogeneity (ca. 65%)

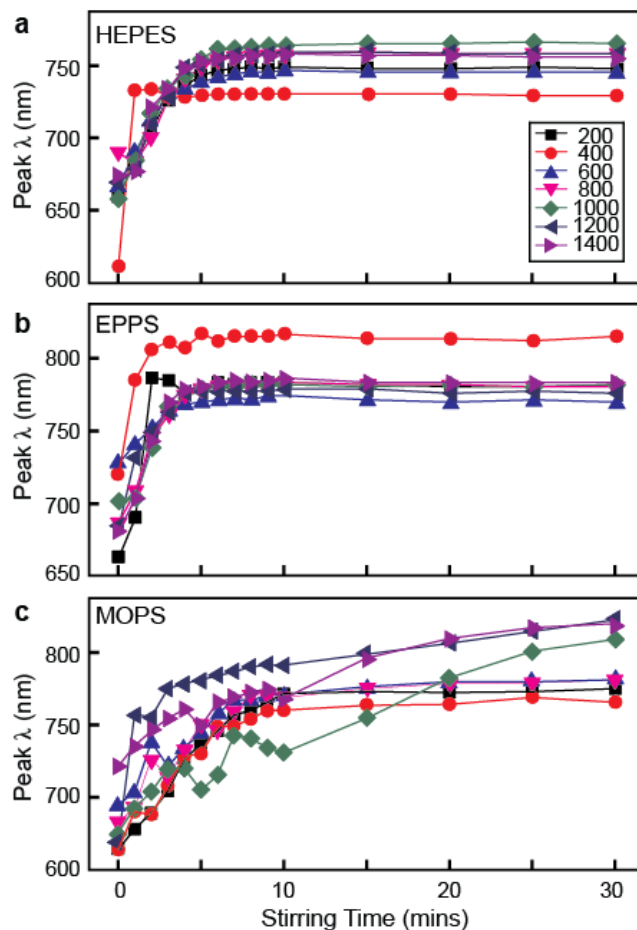


Figure 2.3: LSP shifted with stirring speed. The final primary peak wavelength of (a) HEPES, (b) EPPS, and (c) MOPS AuNS after being stirred for varying lengths of time at 200 – 1400 RPM. The growth solutions were stirred for 0 – 30 min and then left overnight to allow for the reaction to complete. The spectra were taken 24 h after stirring. With an increase in stirring time, a red shift in the absorbance peak for all three buffers occurred. For HEPES and EPPS AuNS, a plateau in the LSP resonance occurred around 6 min of stirring. There was no clear effect of the different stirring speeds on the peak wavelength.

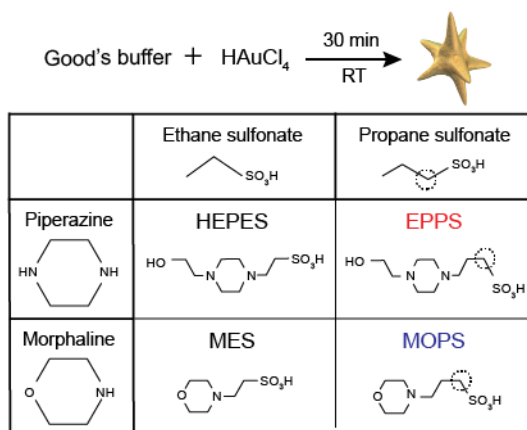
2.2.2 *Reaction Kinetics and Stability Depended on Good's Buffer Type*

Optimized agitation conditions may aid in AuNS syntheses using other Good's buffers that previously did not form such shapes. We used these stirring conditions (5 min at 1400 RPM after addition of gold salt) to test whether other buffers — EPPS, MOPS, and MES — with chemical moieties similar to HEPES could produce AuNS (**Table 2.1**). EPPS contains a piperazine ring, a hydroxyl group, and a propane sulfonate group, and MOPS and MES contain a morpholine group with one tertiary amine, alkane sulfonate groups, and no hydroxyl groups. Morpholine has produced cationic free radicals in the presence of HAuCl_4 ,¹⁰¹ but neither MES nor MOPS has been used previously to synthesize AuNS. Morpholine has only one tertiary amine, so the reaction rate may be slowed compared with buffers that contain the piperazine ring.

To compare the reaction rates among the buffers that produced AuNS, a ratio $R_{\text{buffer}} = 700$ at pH 7.2 was used for all Good's buffers. We measured the optical absorbance of the growth solution every two min until the peak absorbance stabilized ($\pm 1\%$) for at least 10 min. The absorbance was measured again after 24 h to ensure that the reaction had completed. MES did not produce anisotropic particles at these conditions or any concentration ratio or pH within the buffering range (**Figure 2.4**). HEPES, EPPS, and MOPS all produced AuNS at the $R_{\text{buffer}} = 700$. Our observation that a morpholine-containing buffer (MOPS) could show reducing and shape-directing properties opens the phase space for seedless nanoparticle synthesis.

Table 2.1: Molecular structure of Good's buffers (HEPES, EPPS, MOPS, and MES).

Molecular structure of HEPES and EPPS, containing a piperazine ring and a hydroxyl group, and MES and MOPS, containing a morpholine ring. HEPES and MES have an ethane sulfonate group, where EPPS and MOPS have a propane sulfonate group with an additional carbon (dashed circle).



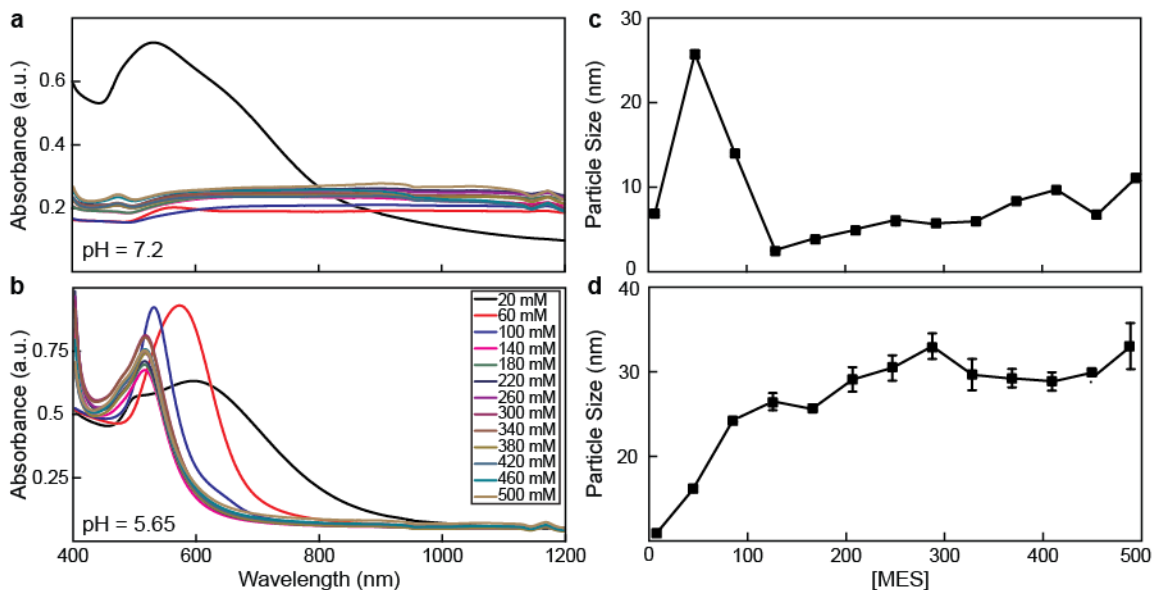


Figure 2.4: MES buffer did not produce AuNS at any pH or concentration. MES absorption spectra (**a**, **b**) and corresponding particle size (**c**, **d**) for 100 to 2500 R_{MES} were collected at two pHs: 6.7 and 5.65. MES was tested through the entire buffering range from 5.5 – 6.7. Two representative spectra are shown above and below the pK_a of MES. At a high pH, the solutions were unable to form particles in solution except at the lowest [MES] of 20 mM. At $pH < pK_a$, MES formed spherical particles in solution.

The primary absorption LSP peak (λ_1) for HEPES AuNS and EPPS AuNS did not change after ca. 15 – 20 min, which indicated the end of the reaction, while MOPS AuNS stabilized at ca. 30 min (**Figure 2.5a, Figure 2.6**). HEPES and EPPS have one more tertiary amine than MOPS and subsequently had a faster reaction time. At $R_{\text{buffer}} = 700$, HEPES solutions had one primary LSP peak, at $\lambda_1 = 800$ nm and a very low intensity peak at 1100 nm, and EPPS and MOPS solutions had two peak resonances at $\lambda_1 \sim 700$ nm and $\lambda_2 \sim 1000$ nm of similar intensity. These two LSP modes were likely from the longer branch lengths and larger overall size of EPPS and MOPS AuNS (Figure 2.5a inset, **Table 2.2**). The λ_2 peak for both EPPS and MOPS AuNS developed around 10 min, which suggests the λ_2 peak did not develop during the initial growth (**Figure 2.5b**).

The structural and optical stability of AuNS solutions were tested for one month. AuNS were stored in the buffer growth solution at 4 °C to minimize peak wavelength shift (**Figure 2.7**). MOPS AuNS turned into spheres after 12 days, while the structure of HEPES and EPPS AuNS were maintained. Specific functional groups in the buffers may play a role in shape stability over time. For example, the ethane sulfonate group of HEPES can bind to the Au surface, and the hydroxyl group can facilitate self-assembly and bilayer formation via hydrogen bonding to allow for shape stability.¹⁰³ Unlike HEPES and EPPS, MOPS does not have a hydroxyl group and cannot form hydrogen bonding necessary to stabilize the self-assembled bilayer. MOPS AuNS did not maintain their shape (**Figure 2.5c, Figure 2.8**); thus, we hypothesize that the lack of bilayer caused the MOPS AuNS to turn into spheres within two weeks of synthesis. In contrast, we attribute the stability of the HEPES and EPPS AuNS to the bilayer formation that is facilitated by the hydroxyl group.

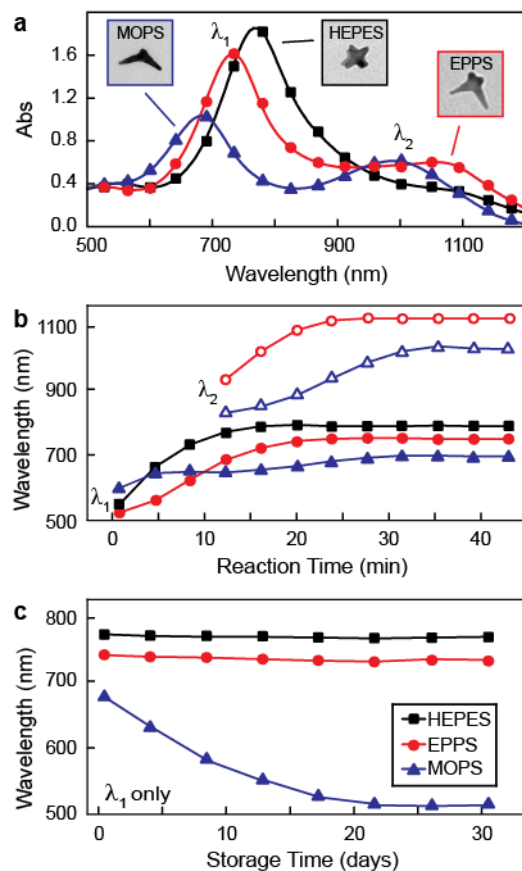


Figure 2.5: Reaction rates of HEPES, EPPS, and MOPS AuNS synthesis at $R_{\text{buffer}} = 700$.

(a) The final spectra of AuNS formed by HEPES, EPPS, and MOPS at $R_{\text{buffer}} = 700$. TEM images indicate general shape of AuNS solutions from different buffers with box size $200 \text{ nm} \times 200 \text{ nm}$. **(b)** Peak absorbance wavelength of HEPES, EPPS, and MOPS AuNS as the reaction progressed. The solid symbols correspond to λ_1 , the peak ca. 700 nm, and the open symbols correspond to λ_2 , the peak ca. 1000 nm. **(c)** The λ_1 peak of the absorbance spectra was recorded over 30 days for AuNS synthesized at 700 R_{buffer} . HEPES and EPPS AuNS peak wavelength was maintained, while MOPS AuNS peak wavelength blue shifted.

Table 2.2: AuNS particle size at the highest R_{buffer} ratio. The overall particle size was measured through DLS and branch length was measured by analyzing TEM images through ImageJ. Approximately 200 – 250 branches were measured manually to obtain the average branch length. Representative images were taken across the entire TEM grid.

| Buffer Type | R_{buffer} | Hydrodynamic diameter (nm) | Average branch length (nm) |
|-------------|---------------------|----------------------------|----------------------------|
| HEPES | 700 | 50 nm \pm 6 nm | 21 \pm 2 nm |
| EPPS | 2500 | 75 nm \pm 10 nm | 43 \pm 2 nm |
| MOPS | 1100 | 60 nm \pm 8 nm | 36 \pm 4 nm |

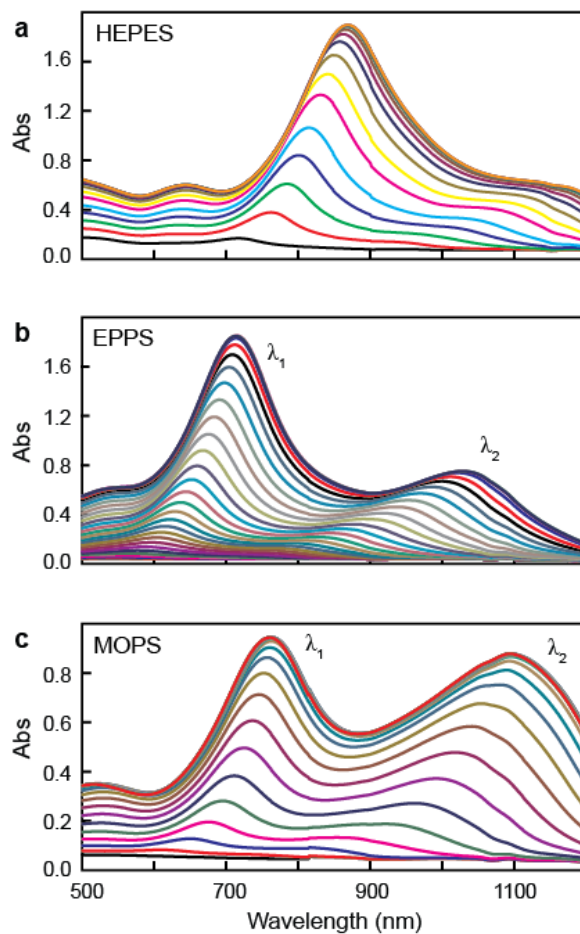


Figure 2.6: Reaction rate spectra of AuNS. Absorbance spectra of (a) HEPES, (b) EPPS, and (c) MOPS AuNS during the synthesis at $R_{\text{buffer}} = 700$. Spectra were taken every two min until the reaction completed. EPPS and MOPS AuNS had two LSP peaks, and HEPES AuNS had one peak. The reaction time for MOPS was longer than that of HEPES and EPPS.

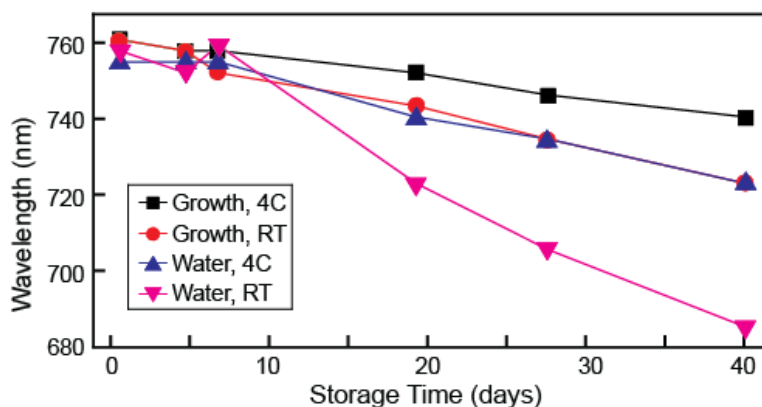


Figure 2.7: Stability of the LSP peak of HEPES AuNS under different storage conditions.

HEPES AuNS were stored either in the growth solution or resuspended in water. These solutions were either then stored at 4°C or at room temperature. The storage conditions that caused the smallest shift in LSP peak was in the original growth solution at 4 °C. Only a 9-nm LSP shift occurred after 20 days and 15-nm over 40 days, which indicated excellent structural and colloidal stability. Blue-shifts in the LSP under other storage conditions are due to AuNS re-shaping, similarly seen with MOPS AuNS solutions blue-shift over a month corresponding to particle shape changing (Figure 2.8). Particle aggregation was not affected by storage conditions.

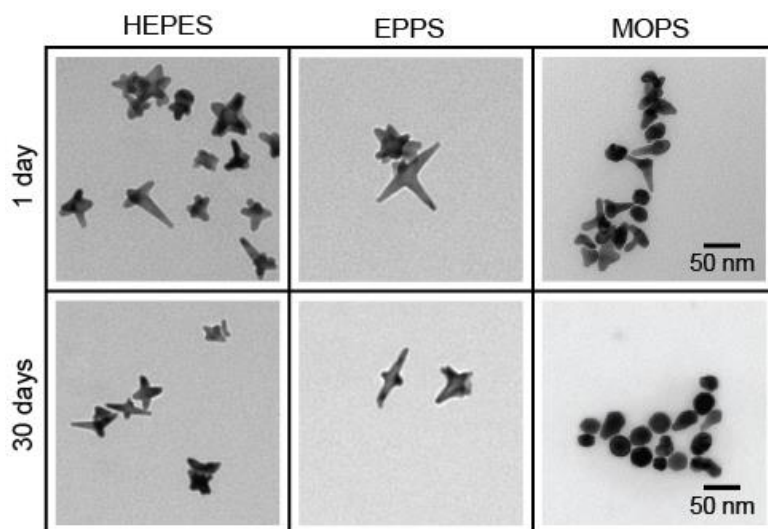


Figure 2.8: TEM images of AuNS from different buffers after a month. TEM images of HEPES, EPPS, and MOPS particles one and 30 days after synthesis. HEPES and EPPS particles maintained the morphology over time; however, the MOPS particles mostly turned into spheres.

2.2.3 pH Crucial for AuNS Formation

Another chemical factor that affects stability of AuNS is the pH of the synthesis solution. All solutions were adjusted to pH 7.2, which is the pK_a of MOPS (7.2) and below the pK_a of HEPES (7.5) and EPPS (8.0). The pH relative to the pK_a affected the charge of the buffer and thus the formation of AuNS. We used a concentration ratio of $R_{\text{buffer}} = 700$ and varied the pH of each buffer solution within their buffering range. To adjust pH, concentrated NaOH was added to the buffer, which also increased the ionic strength (Na^+ ions).¹⁰¹ Since the repulsive forces between negatively charged Au NPs are responsible for colloidal stability, the presence of positively charged ions can lead to aggregation at high Na^+ concentration.

HEPES produced AuNS throughout the entire buffering range (6.9-8.2) with only a slight red shift in the peak wavelength (**Figure 2.9**). Increasing the pH above the pK_a caused a decrease in absorbance and broadening of the LSP peak, which corresponded to greater heterogeneity of NP shape (**Figure 2.10**). For both EPPS and MOPS AuNS, the pH needed to be below or at the pK_a of the buffer to form stable AuNS solutions (**Figure 2.9b**). At a pH above the buffer pK_a , EPPS and MOPS particles aggregated and crashed out a few days later. The syntheses of MOPS and EPPS AuNS were limited to a buffering range smaller than HEPES AuNS.

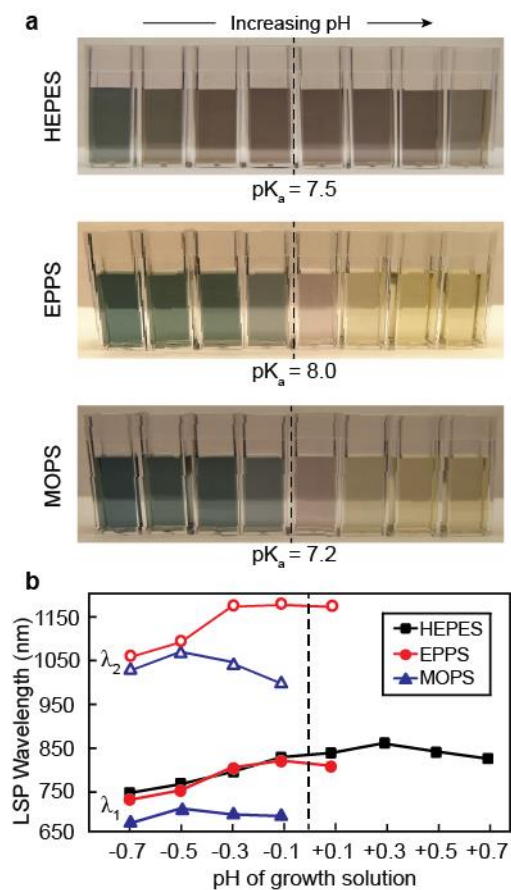


Figure 2.9: pH dependence of HEPES, EPPS, and MOPS AuNS formation throughout their respective buffering range. (a) Photographs of the solutions at varying pH conditions, $pK_a \pm 0.7$. (b) Corresponding peak wavelength of the absorbance spectra. The solid symbols corresponded to λ_1 , and the open symbols corresponded to λ_2

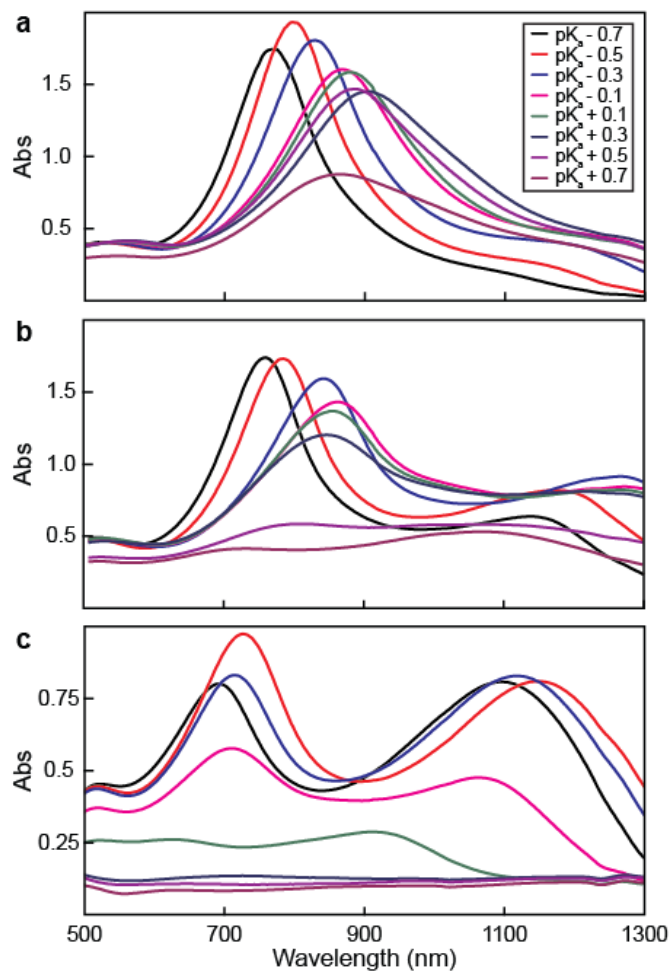


Figure 2.10: Spectra of AuNS synthesized at varying pH. Absorbance spectra of (a) HEPES, (b) EPPS, and (c) MOPS AuNS synthesized at varying pH within the buffering range of each buffer. HEPES AuNS were formed throughout the buffering range but with decreased absorbance with increased pH. EPPS AuNS formed below and slightly above the pK_a of the buffer. When the pH was much greater than the pK_a of the buffer, EPPS AuNS were unable to form. MOPS solutions showed the lowest tolerance to changes in pH and were unable to form AuNS above the pK_a of the buffer

2.2.4 Structure and Corresponding Optical Properties of AuNS

After confirming that $\text{pH} = 7.2$ could form AuNS for all buffers, we established the buffer concentration range to produce AuNS. R_{buffer} was changed with a fixed gold salt concentration (0.2 mM) and constant pH (7.2), conditions that have produced AuNS with HEPES.⁵⁸ At concentration ratios that produced AuNS, HEPES had one LSP peak λ_1 , but EPPS and MOPS AuNS had two peaks λ_1 and λ_2 (**Figure 2.11**). HEPES AuNS were synthesized in the range of $R_{\text{HEPES}} = 250 - 750$, which tuned the LSP peak wavelength from 650 to 900 nm (**Figure 2.11a**, **Figure 2.12**). The average tip-to-tip distance for HEPES AuNS at $R_{\text{HEPES}} = 700$ was ca. 50 nm with averages branch length of 21 ± 2 nm. At low R_{HEPES} , fewer HEPES molecules were available to bind and direct growth, which lead to shorter branches. With increased R_{buffer} , more Au ions reduced onto specific facets of the NP surface to produce structures with longer branches,⁵⁸ and hence a red-shift of the LSP. At higher R_{HEPES} , HEPES AuNS produced a secondary peak ca. 1100 nm with low intensity. In general, any λ_2 peak was less pronounced for HEPES AuNS because of shorter branches compared with EPPS and MOPS AuNS (**Figure 2.13**). The spectral width of the λ_1 peak from HEPES AuNS was narrower than those of EPPS and MOPS AuNS due to greater homogeneity of the solution (Figure 2.11, Figure 2.2). HEPES was unable to form AuNS at $R_{\text{HEPES}} > 750$ (Figure 2.11a).

EPPS buffer produced branched particles in a wider concentration range, $R_{\text{EPPS}} = 400 - 2500$, compared to HEPES (**Figure 2.11b**). At $R_{\text{EPPS}} = 600$, EPPS AuNS were approximately the same overall tip-to-tip size as AuNS at $R_{\text{HEPES}} = 700$. Similar to HEPES, EPPS adsorbed preferentially and exposed only certain facets for gold salt reduction, which caused longer branches with increased concentration. EPPS solutions above $R_{\text{EPPS}} = 600$ produced AuNS with long branches

(ca. 30 – 80 nm) that correlated with the spectra having two LSP peaks. Due to an increase in branch length with increasing R_{EPPS} , both λ_1 and λ_2 resonances red shifted. As the red-shifted λ_2 absorbance peak grew in intensity and broadened, the λ_1 LSP peak decreased in absorbance. At high EPPS concentrations, the λ_2 peak broadened because of heterogeneity of shape¹²²⁻¹²³ in the solution (**Figure 2.14**). At $R_{\text{EPPS}} > 1250$, AuNS had an average tip-to-tip distance of ca. 85 nm and branch lengths (43 ± 2 nm) longer than HEPES could achieve at any concentration ratio (Figure 2.11a-b, Figure 2.13). This result suggests that the propane sulfonate group on EPPS could add additional stability to the branched structure of the particles.¹⁰³

Similar to EPPS, all MOPS solutions that produced AuNS had two LSP peaks: λ_1 around 650 nm and λ_2 around 950 nm (**Figure 2.11c**). MOPS buffer, which contains a morpholine ring and a propane sulfonate group, created AuNS in a range between $R_{\text{MOPS}} = 500 - 1100$. MOPS AuNS also had longer branches (ca. 25 – 35 nm) compared to HEPES AuNS. We propose that the propane sulfonate group¹⁰³ could promote the growth of longer branches than the ethane sulfonate group. The large peak around 550 nm in the MOPS absorbance spectra corresponded to spheres (ca. 47%) in the solutions (Figure 2.14). Ultimately, without hydroxyl and subsequent bilayer formation, MOPS produced more spheres initially, and then the AuNS also changed into spheres over time (Figure 2. 5). These chemical differences also led to larger overall sizes of EPPS and MOPS AuNS compared to HEPES AuNS (Figure 2.13).

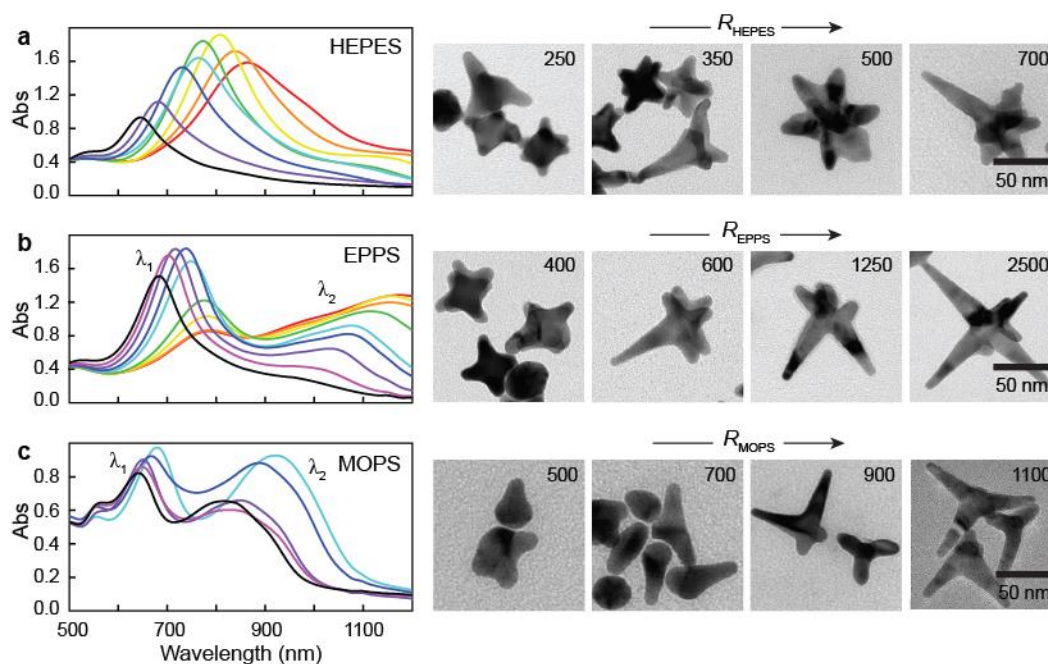


Figure 2.11: Absorbance spectra of HEPES, EPPS, and MOPS through the concentration ranges that produced AuNS. Absorbance spectra and TEM images of AuNS synthesized with (a) 250 to 750 R_{HEPES} , (b) 400 to 2500 R_{EPPS} , and (c) 500 to 1100 R_{MOPS} . The lowest concentration (black) starts on the left and increases to the right to the highest concentration (red or cyan). The number in the upper RH corner of each image is the corresponding R_{buffer} value

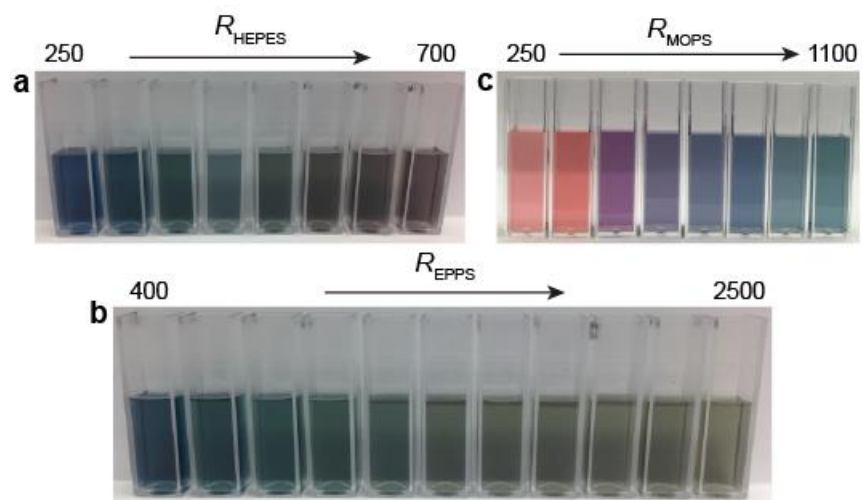


Figure 2.12: Photographs of AuNS at varying buffer concentrations. AuNS solutions synthesized with (a) HEPES, (b) EPPS, and (c) MOPS at varying concentrations. MOPS produced AuNS in the smallest concentration range compare with EPPS and HEPES. EPPS was able to produce AuNS in the largest concentration range from $R_{\text{EPPS}} = 400$ to 2500

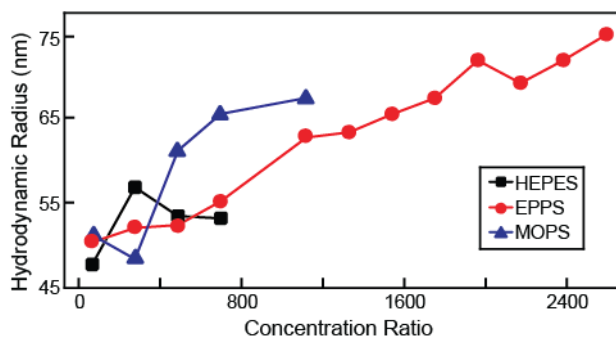


Figure 2.13: DLS of AuNS synthesized at varying concentrations. AuNS were synthesized from 100 to 2500 R_{buffer} . With an increase in R_{EPPS} , AuNS particle size increased whereas HEPES and MOPS AuNS particle size plateaued or solutions aggregated. These measurements were taken through DLS, which determines the size distribution of particles (typically spheres) in solution. Since our particles are anisotropic, the hydrodynamic diameter measurements serve only as an estimate of their overall size.

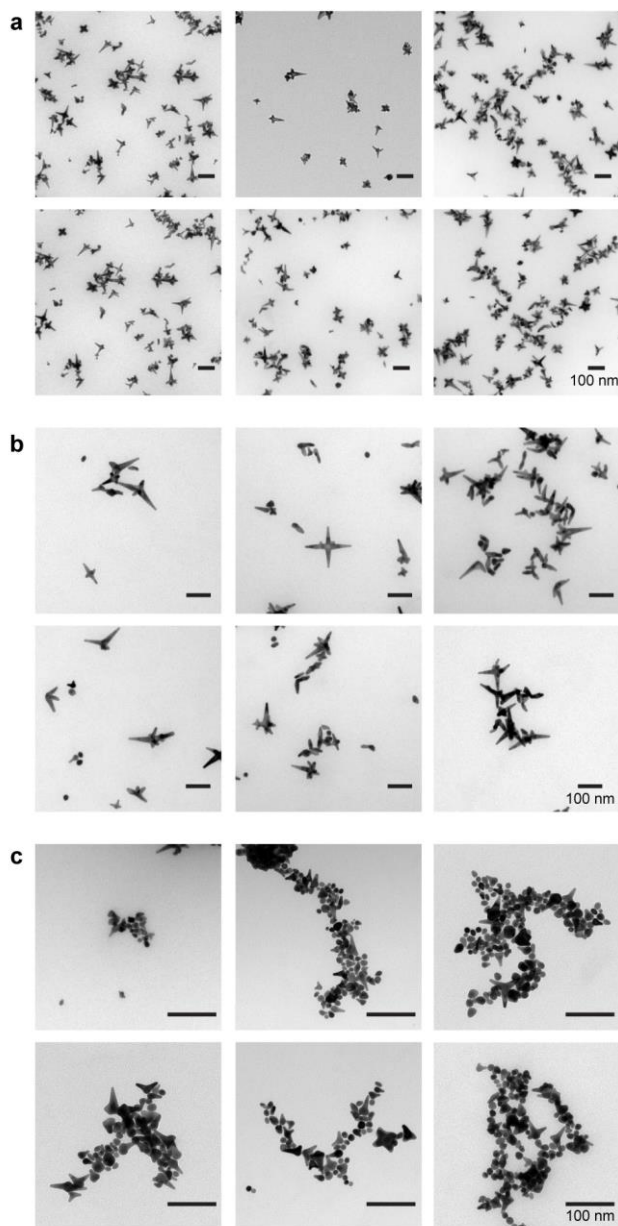


Figure 2.14: Low magnification images of AuNS. Zoomed-out TEM images of (a) HEPES, (b) EPPS, and (c) MOPS AuNS. HEPES and EPPS solutions had fewer spheres. These images demonstrate the large distribution of particle shapes for MOPS AuNS solutions. Based on ≥ 300 particles, we found MOPS AuNS solutions contained 53% spherical byproducts.

Due to varying branch lengths between AuNS synthesized with different buffers, we explored whether variations in the chemical moieties affected the crystallographic direction of branch growth. Because as-synthesized AuNS are heterogeneous, and the structures depended on concentration, we reported branch directions based on HR-TEM analysis of AuNS synthesized at a single (highest) R_{buffer} . To obtain high resolution images with lattice fringes, the orientation of the branches needed to be perpendicular to the direction of the electron beam. Because of the 3D structure of AuNS and random distribution on the TEM grid, however, few branches were so aligned. For a single AuNS with multiple branches, typically only one of the branches was perpendicular to the electron beam, which is necessary to resolve Au lattice fringes. Therefore, we based our assignment on Fast Fourier Transform (FFT) analysis of the lattice fringes on 10 – 15 branches from separate particles from each type of AuNS (**Figure 2.15-17**).

Figure 2.18 shows the lattice spacing between adjacent planes, indicated with two parallel white lines, and the direction of the branches of HEPES, EPPS, and MOPS AuNS. The lattice spacing (d) between the $\{111\}$ planes and between the $\{110\}$ planes in the Au face-centered cubic (FCC) lattice are 0.236 nm and 0.288 nm, respectively. We measured a lattice spacing of $0.234 \pm .003$ nm along the branches of HEPES AuNS, which corresponded to Au $\{111\}$ planes. This result confirmed previous reports^{58, 96} that the branches of HEPES AuNS grew in the $[111]$ direction (**Figure 2.18a**, Figure 2.15). HEPES particles had shorter branches (ca. 20 nm) than the AuNS synthesized in other buffers. Since the branches of the particles were shorter, we could also resolve the central region where the branches intersected. Twin boundaries occurred between the branches, and all grew in the $[111]$ direction.

Interestingly, the small difference in chemical structure between EPPS and HEPES (an additional carbon in the alkane sulfonate chain) had a large effect on the direction of branches. EPPS AuNS had branches with lattice spacing of $0.289 \pm .002$ nm (**Figure 2.18b**), which indicated that the branches grew in the [110] direction. EPPS AuNS had much longer branches than HEPES AuNS. All the branches on EPPS AuNS ($R_{\text{EPPS}} = 2500$) that were analyzed were in the [110] direction (Figure 2.16). Similar to EPPS AuNS, the spacing between lattice planes of MOPS AuNS was $0.286 \pm .009$ nm, which indicated branched growth along the [110] direction (**Figure 2.18c**, Figure 2.17). During the anisotropic growth of branches, gold ions are preferentially reduced along open deposition sites: {111} for HEPES and {110} for EPPS and MOPS. The branch direction was distinct between AuNS formed in buffers containing propane sulfonate groups (EPPS, MOPS) versus ethane sulfonate (HEPES). Previously, the alkane sulfonate group was thought to form a bilayer to stabilize AuNS;¹⁰³ however, we found that a small change in alkane sulfonate chain length could also influence branch direction.

2.3 Summary

We reported a set of design rules for a seedless synthesis method based on Good's buffers that can be used to tailor the dimensions, shape, and optical properties of AuNS. This synthesis is scalable and uses biocompatible reagents instead of more cytotoxic shape-directing agents. Stirring the growth solution during the reaction increased the yield of AuNS and reduced unwanted spherical byproducts. Significantly, we expanded the library of precursors that could form AuNS to include morpholine-containing Good's buffers. We also found that EPPS and MOPS buffers produced AuNS with larger hydrodynamic diameters and branch lengths and promoted branch growth in a different crystallographic direction compared to HEPES buffer. Thus, we hypothesize

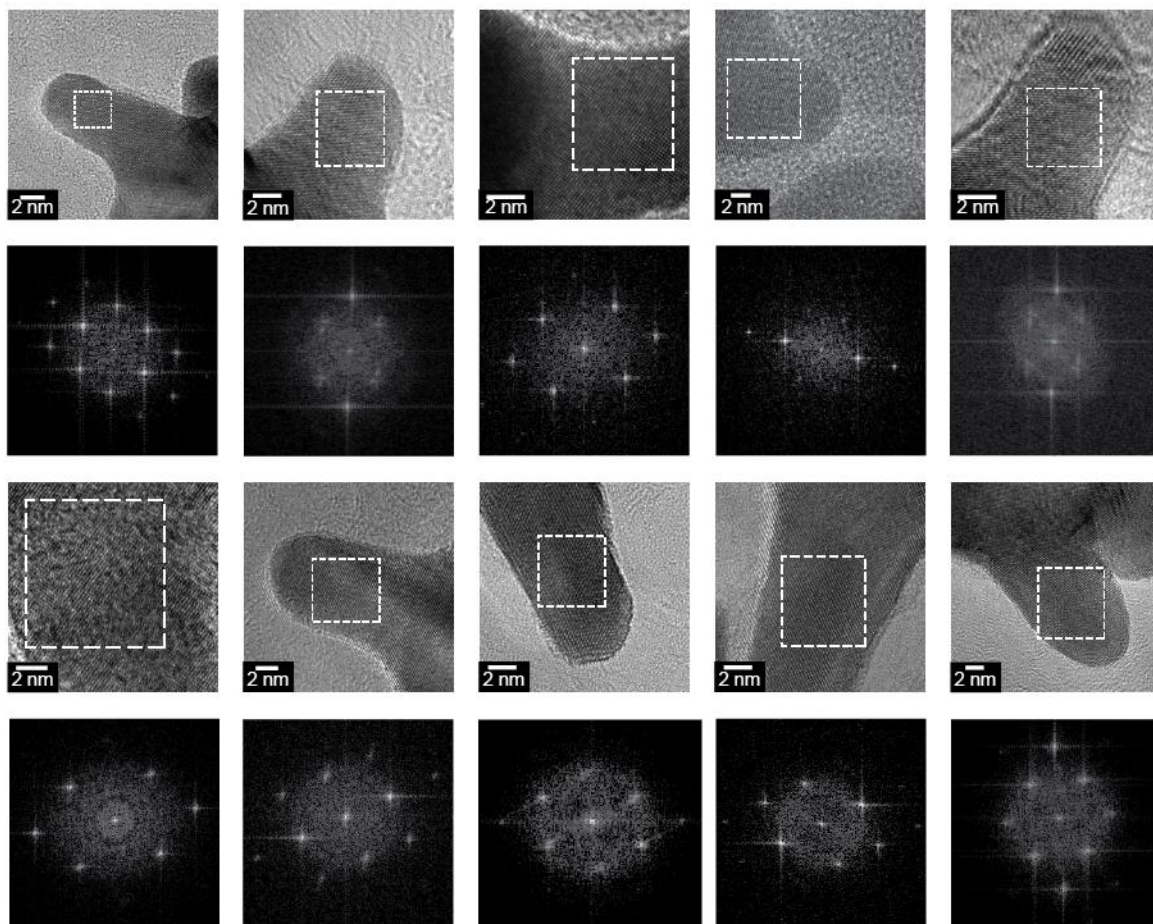


Figure 2.15: HR-TEM images of HEPES AuNS synthesized at 700 R_{HEPES} . HEPES AuNS branches grew in the [111] direction. The dotted white boxes indicate the area analyzed by FFT (bottom). AuNS particles were on an amorphous carbon mesh grid that produced the ring-like structure in the FFT. The presence of the ring depended on the sample thickness (i.e. AuNS branch thickness) and the electron beam intensity.

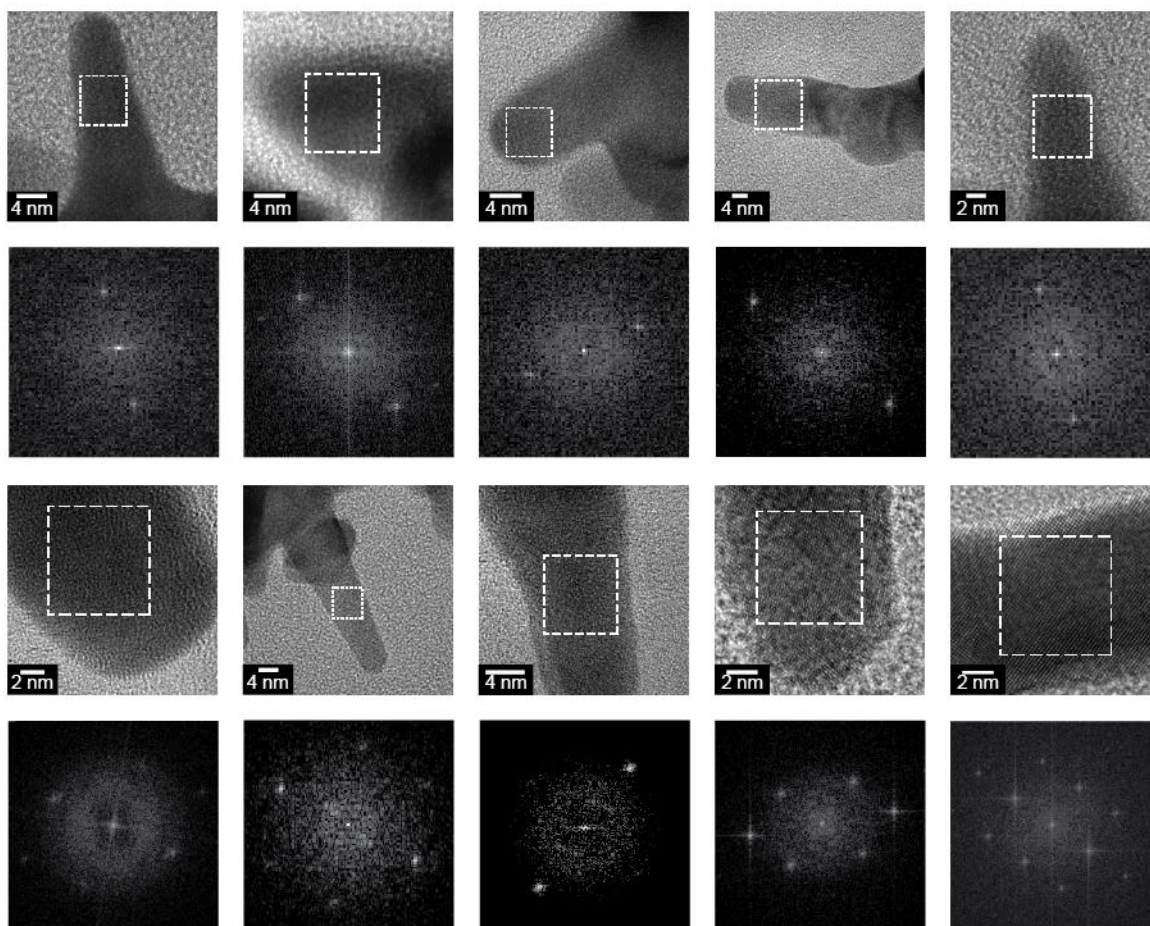


Figure 2.16: HR-TEM images of EPPS AuNS synthesized at 2500 R_{EPPS} . EPPS AuNS grew in the [110] direction. The dotted white boxes indicate the area analyzed by FFT (bottom). AuNS particles were on an amorphous carbon mesh grid that produced the ring-like structure in the FFT. The presence of the ring depended on the sample thickness (i.e. AuNS branch thickness) and the electron beam intensity.

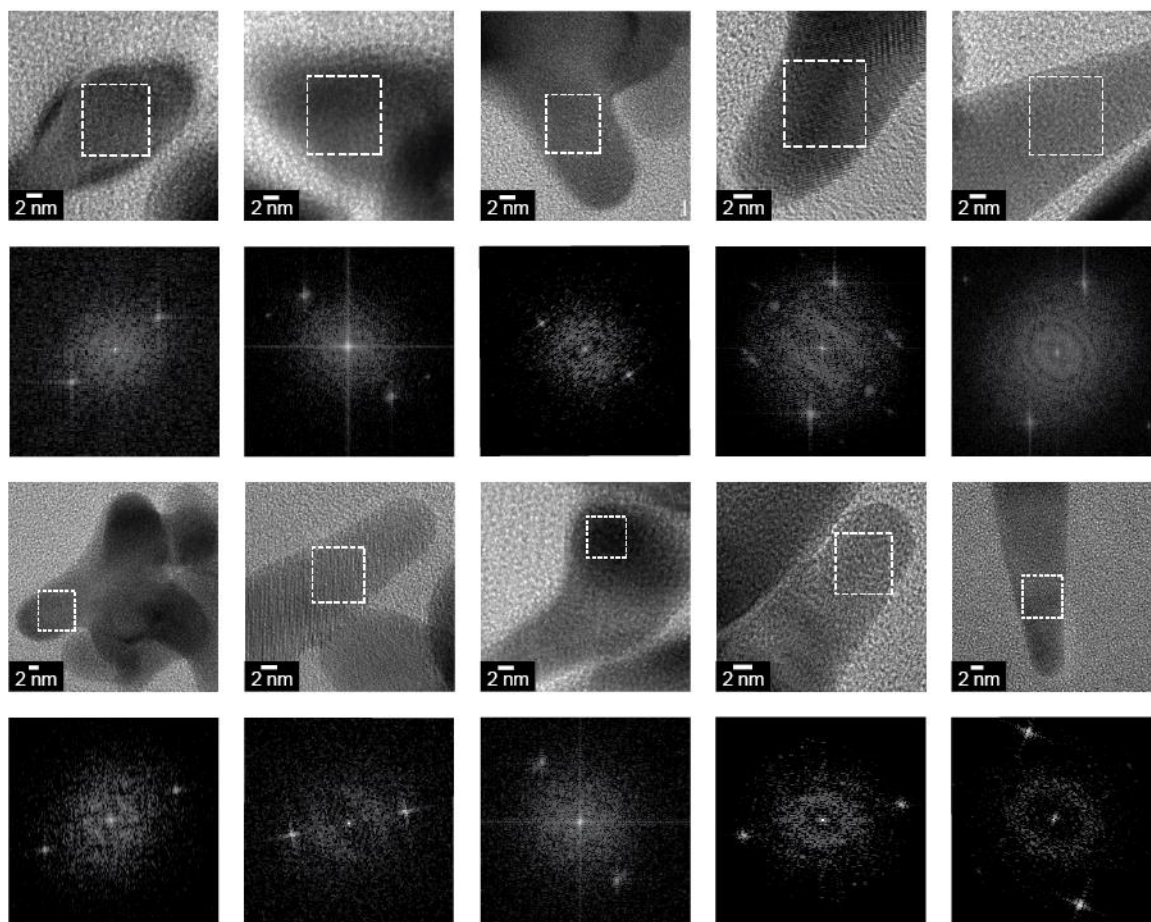


Figure 2.17: HR-TEM images of MOPS AuNS synthesized at 1100 R_{MOPS} . MOPS AuNS grew in the [110] direction. The dotted white boxes indicate the area analyzed by FFT (bottom). AuNS particles were on an amorphous carbon mesh grid that produced the ring-like structure in the FFT. The presence of the ring depended on the sample thickness (i.e. AuNS branch thickness) and the electron beam intensity.

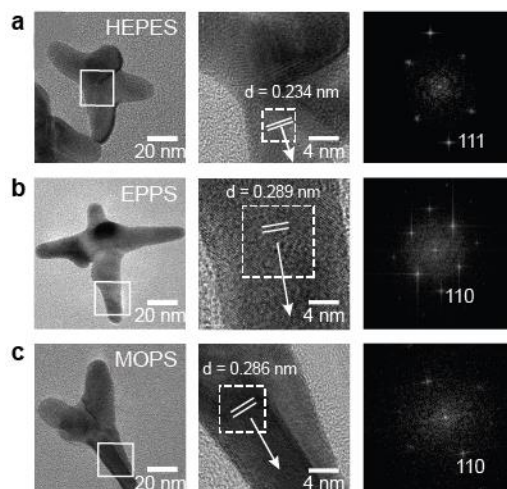


Figure 2.18: HR-TEM images of HEPES, EPPS, and MOPS AuNS. HR-TEM images were taken of AuNS synthesized at the highest R_{buffer} for each buffer. The solid white box on the particle (left) indicates where the zoomed-in HR-TEM image (center) was acquired. The lattice spacing (d) and the direction perpendicular to the corresponding lattice planes (white arrow) were determined through FFT analysis. The FFT (right) was taken from the area outlined with a dotted white box. **(a)** HEPES AuNS have branches in the [111] direction indicated by $d \sim 0.235$ nm between lattice planes and the electron diffraction pattern. **(b)** EPPS and **(c)** MOPS AuNS have branches in the [110] direction, as evidenced by the 0.289 nm distance between lattice planes.

that the alkane length of the sulfonate group may play a significant role in the anisotropic growth of AuNS. AuNS with specific nanoscale features are now possible and their plasmonic properties can be implemented in a variety of applications, from single particle bio-sensing to surface-sensitive catalytic reactions. Our expanded synthetic phase space for the structure and properties of AuNS provides further insight into the mechanism of seedless growth of anisotropic particles.

2.4 Experimental Methods

2.4.1 Gold Nanostar Synthesis

The four Good's buffers used were: 4-(2-hydroxyethyl)piperazine-1-ethanesulfonic acid (HEPES buffer, Sigma Aldrich), 4-(2-hydroxyethyl)-1piperazinepropanesulfonic acid (EPPS buffer, Sigma Aldrich), 2-(N-morpholino) ethanesulfonic acid (MES buffer, Sigma Aldrich), and 3-(N-morpholino)propanesulfonic acid (MOPS buffer, Sigma Aldrich). The 1-M stock solutions were made by dissolving the buffer salt in Millipore water ($18.2 \text{ M}\Omega \cdot \text{cm}$) using a stir bar to ensure thorough mixing. The pH of the buffer solutions was measured using a Thermo Scientific pH meter while being adjusted using concentrated solutions of NaOH. For fine pH adjustments, HCl was added dropwise.

AuNS were synthesized by adding 0.2 mM (final concentration) gold (III) chloride trihydrate (HAuCl_4) (Sigma Aldrich) to varying concentrations of each Good's buffer. Each solution was stirred in a 250-mL round bottom flask for one minute before addition of gold and for 1 to 30 min afterwards. After stirring was stopped at different time points, each solution was left undisturbed at room temperature for 24 h. The zero-minute time point indicates an unstirred solution after the addition of HAuCl_4 . The concentration ratio of the precursors are reported in [buffer]:[HAuCl_4] or R_{buffer} units.

2.4.2 Particle Characterization Techniques

3-mL of AuNS solution was placed in a 1-cm plastic Brookhaven cuvette, and the absorbance spectra was measured from 400 nm to 1200 nm using a LAMBDA 1050 spectrophotometer (Perkin Elmer) or Cary 5000 UV-vis-NIR spectrophotometer (Agilent Technologies). For transmission electron microscopy (TEM) grid preparation, the NPs were concentrated 10 times. Then, 40 μ L of concentrated Au NP solutions were left to rest on carbon Type B, 300 mesh copper grids (Ted Pella) for 20 min and then wicked away with filter paper. A JEOL 1230 TEM and a JEOL 2100F high resolution (HR) TEM were used for imaging the particles. Structural features such as circularity and Feret diameter of AuNS TEM images were characterized using the Analyze Particles plugin on ImageJ for ≥ 300 particles per sample. Images were collected from different areas on the grid to ensure representative imaging of particle shape. A circular threshold of 0.8 was used to define spherical particles. The Feret diameter corresponded to the largest tip-to-tip distance on a particle. Branch lengths were measured manually from the branch tip to the base of the branch from the core of the particle. The crystallographic direction of branch growth was determined by measuring the lattice spacing through Fast Fourier Transform (FFT) analysis of the lattice fringes observed in HR-TEM images.

CHAPTER 3:
SEPARATION OF STABILIZED MOPS GOLD
NANOSTARS BY DENSITY GRADIENT CENTRIFUGATION

This chapter is based, in part, on the research described in the following publication:
Chandra, K.; Kumar, V.; Werner, S.E.; Odom, T.W.; Separation of Stabilized MOPS Gold
Nanostars by Density Gradient Centrifugation. *ACS Omega* **2017**, 2 (8) 4878-4884

3.1 Introduction

The physical and chemical properties of anisotropic gold nanoparticles are controlled by their dimension and shape.¹¹¹ Gold nanostars (AuNS) are high-performing substrate materials for surface-enhanced Raman spectroscopy,^{59, 63-65, 124} photothermal therapy,⁶⁶ and photoacoustic imaging⁶¹ because they exhibit strong electric field enhancements on multiple sharp tips.⁶² AuNS are of interest among anisotropic nanoparticles because minor shape modifications, such as aspect ratio and branch length,^{58, 100} enable tunability of the localized surface plasmon (LSP) resonances.^{59-61, 97} Accessing specific structural features of AuNS has driven synthetic techniques that can control the chemical environment by introducing different reactants.^{87, 125-126} Typically, AuNS are prepared by seed-mediated syntheses;¹²⁷⁻¹²⁸ however, these methods require strongly bound, cytotoxic surfactants that limit biological applications. A commonly used seedless synthesis method for AuNS that avoids additional surfactants only involves two precursors: a Au salt (HAuCl₄) and a biocompatible Good's buffer, usually 4-(2-hydroxyethyl)-1-piperazineethanesulfonic acid (HEPES).^{58, 60, 96, 103, 115} The Good's buffer acts as both a reducing and shape-directing agent, with the ethane sulfonate group of HEPES binding to the Au surface and the hydroxyl group facilitating the assembly and bilayer formation to stabilize AuNS.¹⁰³ Recently, we reported the preparation of AuNS with disparate branch lengths, branch tips with a small radius of curvature (3 – 5 nm), and multiple LSP resonances in the near infrared (NIR) and second NIR window using a Good's buffer with a morpholine ring, 3-(N-morpholino) propane sulfonic acid (MOPS).¹⁰⁰

To exploit the unique structural properties of MOPS AuNS, challenges specific to the buffer must be overcome: (1) the morpholine moiety degrades once exposed to HAuCl₄, which causes

colloidal instability;¹⁰² and, (2) MOPS cannot form a stable bilayer without a hydroxyl group, which leads to heterogeneous solutions.¹⁰³ Adjusting synthetic conditions is a common strategy to obtain stable and homogenous Au nanoparticle solutions, but exquisite control over room-temperature reaction conditions is limited;¹²⁹ hence, post-synthetic separation offers an approach to obtain purer solutions of anisotropic particles. Centrifugation,¹³⁰ size exclusion chromatography,¹³¹ filtration or diafiltration,¹³²⁻¹³³ and electrophoresis¹³⁴ have been used to produce metal nanoparticle solutions with narrow shape and size distributions. In particular, density gradient centrifugation (DGC) is a post-synthetic sorting technique that can refine structural distributions of metal nanoparticles by rate-zonal separation.¹³⁵ In this method, the sorting of particles primarily depends on sedimentation rate, which is a function of their size and shape. Standard gradient media are deleterious to anisotropic metallic nanoparticles with weakly bound surface ligands,¹⁰⁹ however, sucrose shows excellent compatibility.¹³⁶⁻¹³⁷

Here we describe a strategy to obtain highly-enriched populations of AuNS by combining stabilization and sorting processes. We improved the homogeneity of MOPS AuNS and reduced the percentage of unwanted spherical byproducts by adjusting storage conditions. By centrifuging as-synthesized, unsorted mixtures through a sucrose density gradient, we isolated solutions of AuNS based on branch length and number. We demonstrated that only a single round of DGC was needed to sort AuNS solutions by size and shape; an additional round did not significantly improve separation of the sorted samples.

3.2 Results and Discussion

3.2.1 Establishing MOPS AuNS Stability

Figure 3.1 summarizes the stabilization and separation of heterogeneous MOPS AuNS populations. AuNS solutions stored in ultra-pure, deionized water maintained shape integrity compared to those stored in the MOPS buffer. To overcome particle heterogeneity, we sorted AuNS first by layering a concentrated solution on top of a sucrose density gradient and then by performing DGC. In subsequent rounds of DGC, the original (O) fractions were concentrated and centrifuged through a shallow linear gradient.

AuNS were synthesized using a modified version of our previously established procedure¹⁰⁰ with 150 mM of the Good's buffer MOPS and 0.2 mM HAuCl₄. We selected these conditions since this MOPS concentration produced AuNS with two distinct LSP peaks (**Figure 3.2**). The as-synthesized solutions were characterized by UV-Vis spectroscopy to measure the bulk optical properties and transmission electron microscopy (TEM) to visualize individual AuNS. The zero-minute time point indicates an unstirred solution after the addition of HAuCl₄. After one minute of vortexing, one LSP peak at shorter wavelengths, λ_1 , formed between 700 and 750 nm (**Figure 3.1a**). Throughout the reaction, a LSP peak at longer wavelengths, λ_2 , formed at 800 nm and red shifted to ca. 1100 nm. After 24 h, both LSP peaks blue shifted and decreased in absorbance as the 520-nm LSP peak intensity increased (**Figure 3.2b**, **Figure 3.3**), possibly due to a decrease in particle size and average branch length as well as an increase in number of spherical particles (**Table 3.1**). We hypothesize the MOPS buffer was displaced from the surface of the particles, which resulted in a change in shape.

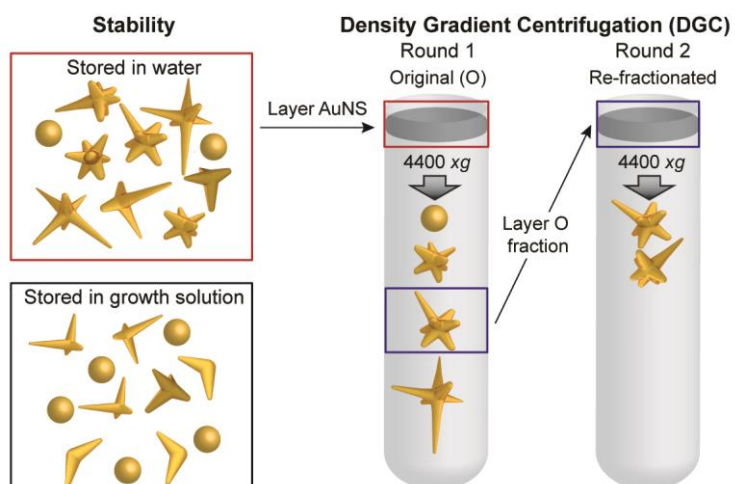


Figure 3.1: Stabilization and separation of MOPS AuNS scheme.

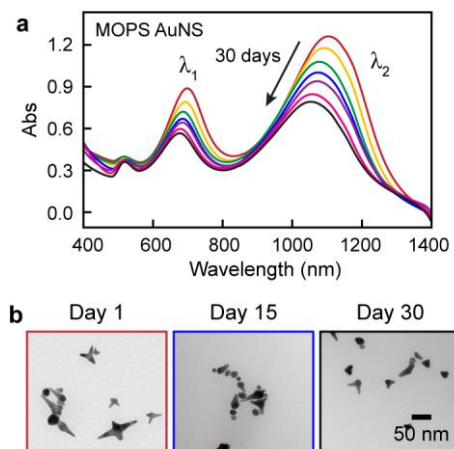


Figure 3.2: Absorbance peak of MOPS AuNS in growth solution blue shifted over 30 days.

(a) The absorbance was measured 24 h (red line) after the addition of H_{AuCl}₄ up to 30 days (black line) in 5-day increments. (b) TEM images of MOPS AuNS after 1, 15, and 30 days after the addition of H_{AuCl}₄.

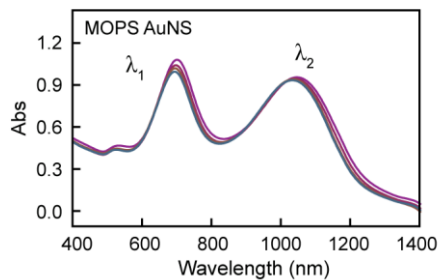


Figure 3.3: Absorbance spectra of AuNS stored in growth solution for initial 24 h. The λ_1 and λ_2 peak do not decrease in intensity nor shift in wavelength 24 h after the addition of gold. The maximum peak absorbance was reached after 60 min, which indicated that the reaction completed. Only minimal shifts in the LSP and absorbance occurred between 1 and 24 h.

Table 3.1: Particle size, average branch length, and percentage of spherical particles at

different time points. The overall particle size was measured using DLS and branch lengths were measured through analysis of TEM images. ≥ 500 branches were measured manually to obtain average branch length. Representative images were taken across the entire TEM grid. At initial time points, larger particles (> 80 nm) remained in solution, with an average branch length 45 ± 9 nm. At longer time points (30 days), particle size decreased by 35 ± 10 nm, and branch length shortened by 20 ± 4 nm compared to the day-1 solution. Additionally, spherical particles percentage increased from 35% to 54% over 30 days, which was corroborated by an increase in the 520-nm LSP peak.

| Time Point | Hydrodynamic diameter (nm) | Average branch length (nm) | Sphere |
|-------------------|-----------------------------------|-----------------------------------|---------------|
| 1 day | 71 ± 9 nm | 45 ± 9 nm | 35% |
| 30 days | 36 ± 10 nm | 25 ± 8 nm | 54% |

3.2.2 *Exchanging Solvent Storage Conditions*

In earlier work, we observed that AuNS synthesized with MOPS transformed into spheres over 12 days when stored in the buffer growth solution.¹⁰⁰ Here, we resuspended the as-synthesized solution in ultra-pure water either one (1× solution) or two (2× solution) times (**Figure 3.4**). We tracked the changes in bulk optical properties at the two LSP peaks to determine whether AuNS shape changed; within the first five days, λ_1 and λ_2 shifted blue-shifted by 15 nm for 1× and 2× solutions. After 10 days, the LSP resonances of the 2× solution did not change, and the branch lengths decreased minimally (by 5 ± 3 nm). Larger AuNS (≥ 80 nm) remained in solution over 30 days compared with as-synthesized particles. The LSP peaks of the 1× solution, however, shifted to shorter wavelengths by an additional 10 nm and 20 nm, and the particle size decreased. The percentage of spherical particles increased for the 1× solution from 35% to 47%, while the percentage remained the same for the 2× solution. We hypothesize that exchanging buffered growth solutions for ultra-pure water stabilized AuNS, in contrast to similar systems that are stabilized by excess buffer solution, since excess MOPS degrades over time in the presence of Au salt.¹³⁸

3.2.3 *Comparing Linear and Step Gradients*

Even with improved storage conditions, MOPS AuNS solutions still contained ca. 37% undesirable spherical particles. Because as-synthesized AuNS showed a broad distribution of shapes (0 – 8 branches) and sizes (20 – 80 nm),¹⁰⁰ we used DGC to sort branched nanoparticles.¹⁰⁹ We compared two different types of gradient densities: linear and step (**Figure 3.5**). A linear gradient contains a single continuous zone while a step gradient has multiple density zones. Both gradients can enrich solutions by sorting nanoparticles into distinct bands.¹³⁵ Changing the gradient

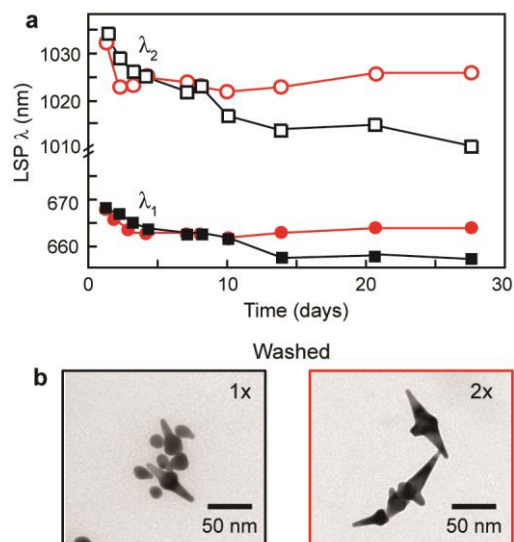


Figure 3.4: Shape stability of AuNS increased due to water resuspensions. (a) Plot of the LSP resonance shift over time for solutions at one (black) and two (red) resuspensions. Filled markers correspond to the λ_1 peak and open markers correspond to λ_2 peak. (b) TEM images of AuNS 30 days after one or two resuspensions in water.

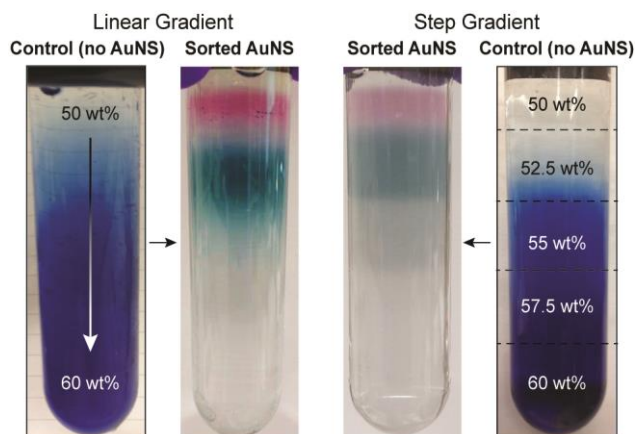


Figure 3.5: Linear gradient allowed for greater separation than step gradient. The control (no AuNS) was used to establish the linear and step gradients and contained the coloring agent Trypan blue. Once the gradients were established, AuNS were centrifuged through a gradient with without Trypan blue (Sorted AuNS). A linear gradient with increasing viscosity and density produced two bands: red and blue. The particles had a greater spatial separation over a step gradient. The step gradient produced two bands, but within the bands particles were not further separated.

composition and centrifugation time can improve both dispersion through the gradient and nanoparticle yield. Since sorting of particles with similar sizes but different shapes requires a shallow gradient (10%),¹⁰⁹ we started with an 50 – 60% (w/v) gradient of sucrose.

To monitor the gradients, we added a standard coloring agent, Trypan blue, to the denser 60% (w/v) solution. For the linear gradient, the dense, blue solution was layered below the clear 50% (w/v) solution. Using a custom mixing program (Methods), the two sucrose solutions were mixed at an angle without AuNS to create a continuous linear gradient (Figure 3.5, control no AuNS). We determined the linearity of the sucrose gradients by fractionating the control gradient and calculated the concentration of sucrose in each fraction using the following equation:¹³⁹

$$c_i = (x - y) \frac{A_{fn}}{A_{60\%}} + y \quad (3.1)$$

where c_i is the concentration of sucrose at point i ; x is the concentration of the heavier solution (60%); y is the concentration of the lighter solution (50%); A_{fn} is the absorbance of fraction n ; and, $A_{60\%}$ is the absorbance of 60% sucrose dye. The concentration of sucrose over the gradient was linear and contained an r^2 -value of 0.9998. For the step gradient, we layered five different density sucrose solutions into zones: 50%, 52.5%, 55%, 57.5%, and 60% (w/v).

We created linear and step gradients without Trypan blue and then layered 500 μ L of AuNS solutions (8 – 10 nM) and centrifuged samples at $4400 \times g$ (Figure 3.5, sorted AuNS). DGC is limited intrinsically by the sample volume that can be layered on top of the gradient;¹⁴⁰ however, we found that the starting concentration of the layered sample had no effect on the degree of separation (**Figure 3.6**). In the linear gradient, two distinct bands formed: (1) a thin red band of spherical nanoparticles and (2) a long blue/gray band of sorted AuNS. TEM analysis verified that the red band contained 80 – 85% spherical nanoparticles and the blue/gray band had enriched

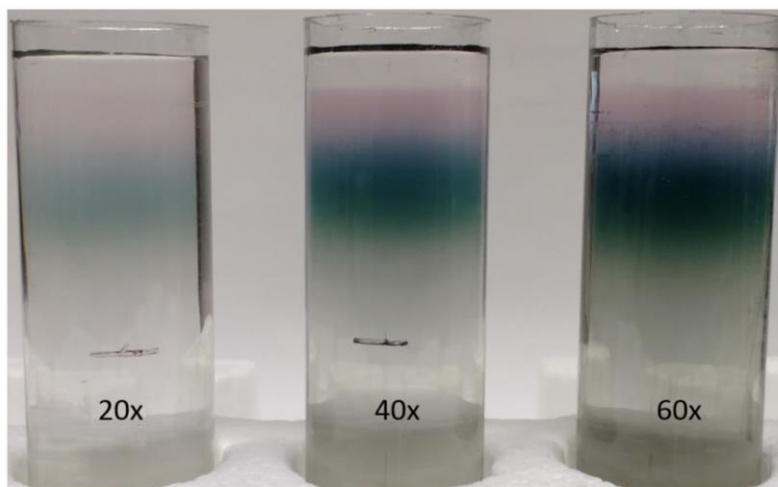


Figure 3.6: Varying concentration of layered sample did not affect separation. The layered sample for DGC is typically limited to 200 – 500 μL ; however, the concentration of the sample can be increased. We changed the concentration of the 500- μL layered solution to 20 \times , 40 \times , and 60 \times the as-synthesized solution concentration. The concentration of the layered solution did not affect the quality of AuNS separation.

populations of AuNS. For the step gradient, centrifugation of AuNS produced bands in the top three zones and resulted in reduced spreading of the particle distributions compared to the linear gradient. Moreover, each step-gradient band contained nanoparticles with mixed particle shapes and size. Hence, linear density gradients can separate similarly sized nanoparticles with small structural differences (i.e. AuNS with varying branch length and number), and step gradients are more useful for sorting a few, distinct populations of nanoparticles.

3.2.4 Characterizing Separation of AuNS in a Linear Gradient

After centrifuging AuNS through the linear gradient, samples were fractionated at intervals of 4 mm from the meniscus 30 times. The corresponding fractions were collected in different tubes and labelled F1 to F30. F1 indicates the top-most fraction, and F30 is the bottom-most fraction. We found the best separation of particles, without forming a pellet at the bottom, occurred for centrifugation times of 1.5 h at $4400 \times g$ (**Figure 3.7a**). To characterize the sorted AuNS fractions (F1 – F30), we measured the absorbance spectra and correlated optical properties with TEM images (**Figure 3.7b-c**). F1 – F4 produced a peak only at 520 nm that corresponded to spherical nanoparticles. F5 – F19 contained AuNS with a LSP at λ_1 between 700 – 720 nm with high intensity absorbance (> 0.3), which was the minimum absorbance needed to image particles and to measure bulk optical properties. The second LSP at λ_2 shifted from 800 nm to 1150 nm in fractions F5 to F19; this shift indicated an increase in branch length. In fractions $> F19$, the absorbance decreased by half, which indicated a low concentration of particles. Although particles with the same mass or shape may have similar sedimentation rates,¹⁰⁹ sorted AuNS showed improved particle homogeneity in each fraction compared with the unsorted solution.

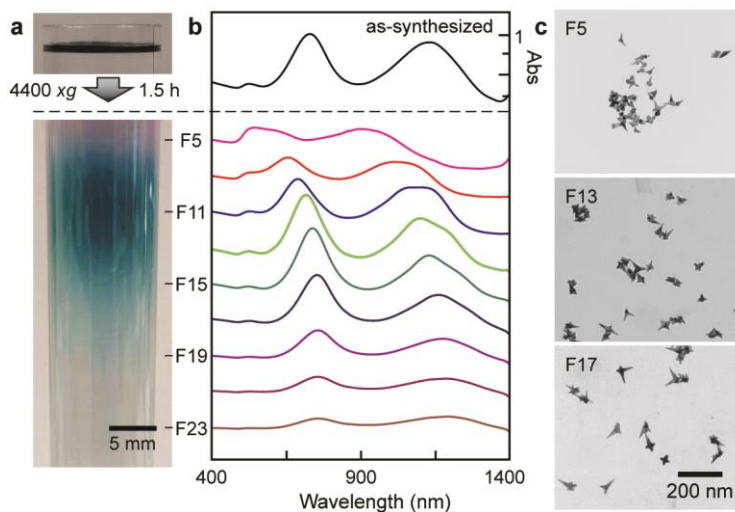


Figure 3.7: Separation of AuNS through a linear density gradient by size and shape. (a) Photographs of F5 – F23 of the AuNS (top) layered on top of the gradient and (bottom) centrifuged through the linear sucrose gradient. **(b)** Absorbance spectra for every odd-numbered fraction from F5 – F23. **(c)** Representative TEM images from F5, F13, and F17 show branched particles in all the different fractions.

3.2.5 *Sorting AuNS by Branch Length and Number*

To quantify particle size, branch length, and branch number of AuNS, more than 500 branches of every other fraction from F5 – F19 were analyzed manually by ImageJ (**Figure 3.8a**, **Figure 3.9**). We omitted F1 – F4 since they contained mostly spherical particles. For F5 to F19, the average tip-to-tip particle size increased from 21 ± 5 nm to 100 ± 17 nm, which also corresponded with an increase in branch length from 18 ± 10 nm to 32 ± 18 nm (**Figure 3.8b**). We observed two populations of AuNS: shorter (< 30 nm) and longer (> 30 nm) branched particles. In all fractions, most branches were less than 30 nm. With an increase in fraction number, the number of short branches decreased as the number of long branches increased. In F5 – F11, the population consisted of particles that had lower masses and hence remained closer to the top of the density gradient. In higher fractions (F13 – F19), AuNS had longer branches with larger particle sizes and greater mass per particle.

Rate-zonal separation efficiency depends on shape or number of branches (0 – 8) per particle (**Figure 3.10**). We categorized fractions into branch-number populations: spheres (0), low (1 – 2), medium (3 – 4), and high (> 5). We observed a decrease in percentage of spheres from 20% to $< 1\%$ from F5 to F13. This low percentage of spheres ($< 1\%$ of the population) remained in F13 – F19, which created highly enriched populations of branched AuNS. Each fraction showed greater particle homogeneity than as-synthesized solutions. From fractions F5 to F19, high branch-number populations increased while low branch-number decreased. Particles with a greater number of branches, longer branches, and larger sizes tended to sediment to the bottom of the gradient. These characteristic differences between spherical nanoparticles and heterogeneous AuNS allowed for sorting based on nanoscale structural features.

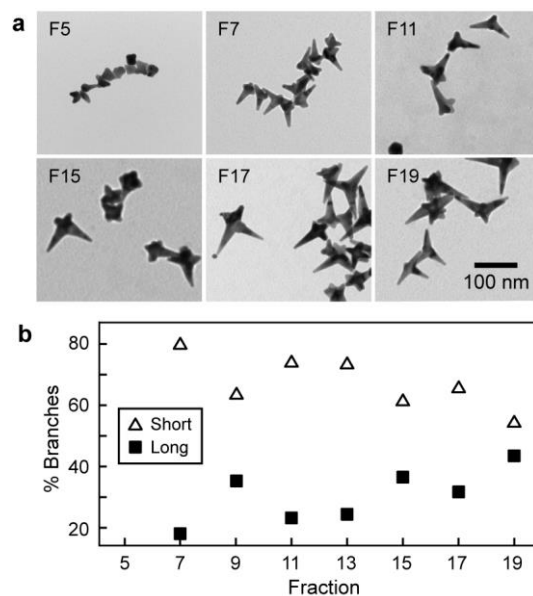


Figure 3.8: Branch length increased with fraction number. (a) TEM images for odd numbered fractions in F5 – F19. (b) The percentage of branches that are short (< 30 nm) or long (> 30 nm) for each fraction.

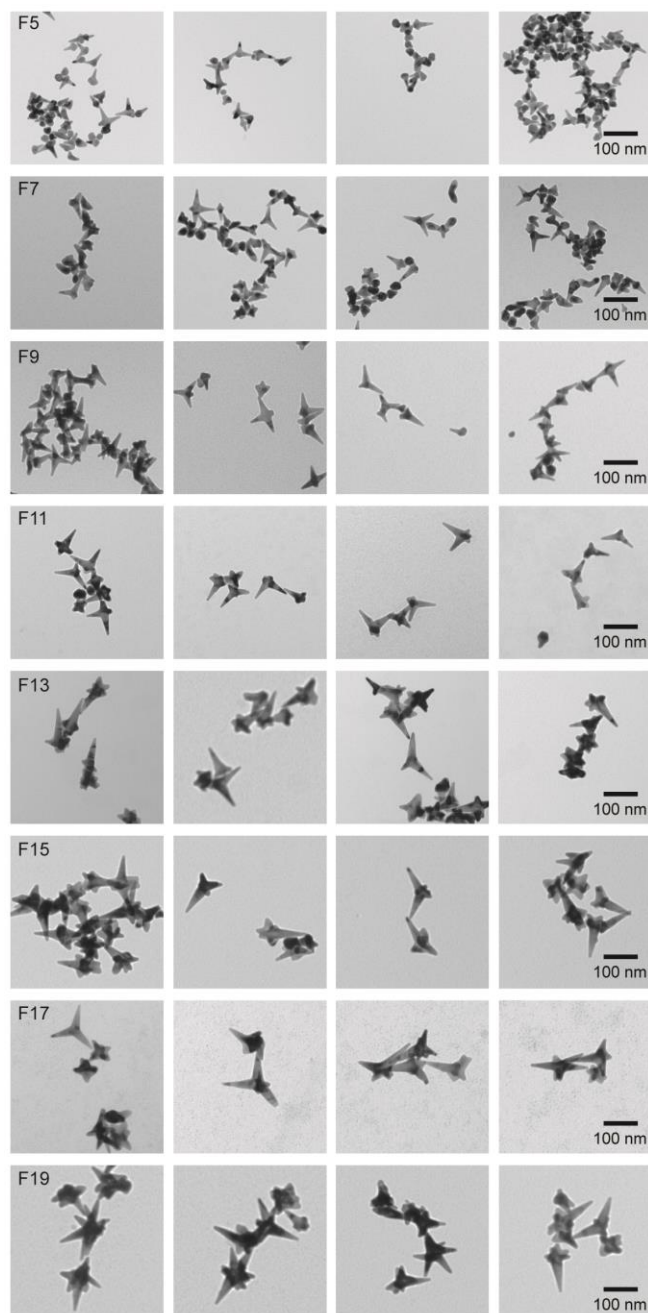


Figure 3.9: Zoomed-out TEM images from each fraction after one round of DGC. Images were collected from different areas of the grid and analysis was performed on ≥ 500 branches per fraction.

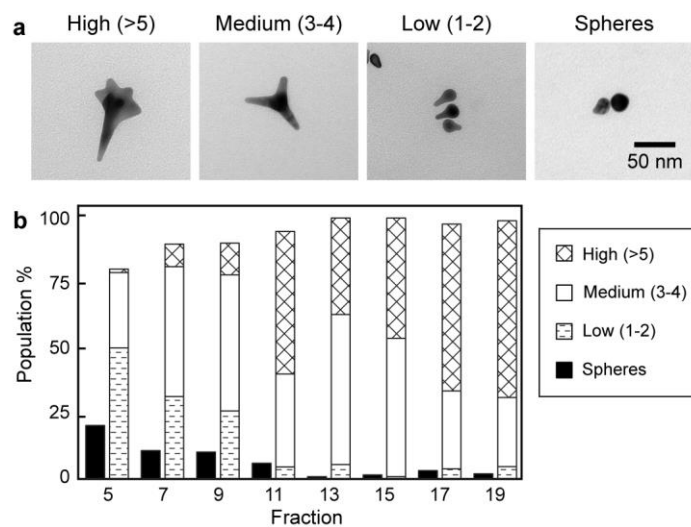


Figure 3.10: Analyzing the AuNS branch number population for each fraction. (a) TEM images of high, medium, and low number of branches. The dimensions of all the images are $150 \text{ nm} \times 200 \text{ nm}$. **(b)** The percentage of the AuNS population that have low (1 – 2), medium (3 – 4) or high (> 5) number of branches.

3.2.6 *Sorting AuNS through a Second Round of Separation*

To achieve more refined populations of AuNS, we processed the original (O) fractions by DGC for a second time (**Figure 3.11a**). During round 1 of DGC, AuNS dispersed throughout the top half of the tube; therefore, for round 2, we created a second linear 50 – 55% (w/v) sucrose gradient. AuNS in the top (T), middle (M), and bottom (B) regions of each gradient were analyzed for branch-number, but no differences were found between the three fractions compared to the original population (**Figure 3.11b**). We found that a single round of rate-zonal DGC efficiently enriched AuNS populations based on differences in size and shape, and additional rounds did not improve particle homogeneity.

3.3 **Summary**

In summary, we established techniques to stabilize and separate heterogeneous solutions of AuNS synthesized with a morpholine-based Good's buffer. The modified storage conditions can be generalized to other metal nanoparticles that change shape in solution over time. We found that linear gradients are better suited to sort similarly sized particles with small differences such as branch length and number. The robust techniques described herein can produce highly-enriched populations of anisotropic nanoparticles that can be exploited for different shape-dependent applications, such as surface-enhanced spectroscopies, sensing of chemical and biological analytes, bio-imaging and therapeutics.

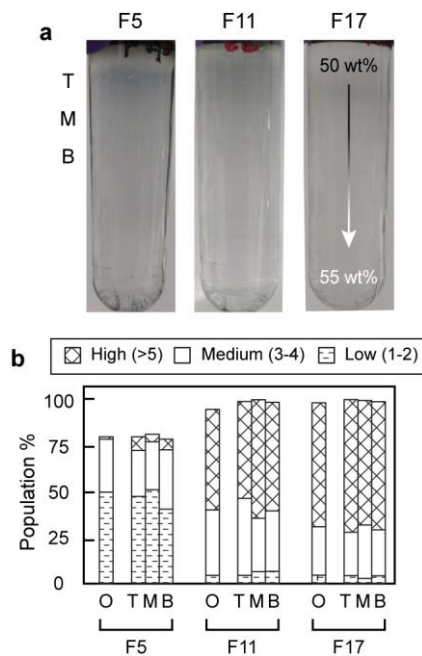


Figure 3.11: Round 2 of DGC fractions did not enrich branch populations. (a) Odd-numbered original fractions were layered on top of a 50 – 55 wt% sucrose gradient and centrifuged for 45 min at $4400 \times g$. Top (T), middle (M), and bottom (B) fractions of the each of the round 2 fractionated samples were collected. (b) The branch number distribution for each of the T, M, and B samples was analyzed manually. The population distribution was similar among the original fractions (O) and re-fractionated samples.

3.4 Experimental Methods

3.4.1 *Gold Nanostar Synthesis*

The Good's buffer used was 3-(N-morpholino)propanesulfonic acid (MOPS buffer, Sigma Aldrich). The 1-M stock MOPS solution was made by dissolving the buffer salt in Millipore water (18.2 M Ω ·cm) using a medium-sized stir bar to ensure thorough mixing. The pH of the MOPS solution was measured using a Thermo Scientific pH meter and was adjusted using concentrated solutions of NaOH. For fine pH adjustments, HCl was added dropwise.

AuNS were synthesized by adding 0.2 mM (final concentration) gold (III) chloride trihydrate (HAuCl₄, Sigma Aldrich) to 150 mM of MOPS buffer. Each solution was vortexed in a 50-mL Falcon tube for one minute before addition of HAuCl₄ and for 1 min afterwards. After vortexing, the growth solution was left undisturbed at room temperature for 24 h. The zero-minute time point indicates an unstirred growth solution after the addition of HAuCl₄.

3.4.2 *Particle Characterization Techniques*

3 mL of AuNS solution was placed in a 1-cm plastic Brookhaven cuvette and the absorbance spectra was measured from 400 to 1400 nm using a Cary 5000 UV-vis-NIR spectrophotometer (Agilent Technologies).

For TEM grid preparation, carbon Type B, 300 mesh copper grids (Ted Pella) were treated with 0.1% (w/v) poly-L-lysine (Sigma Aldrich) for 5 minutes. 40 μ L of 10 \times concentrated Au nanoparticle solution was left to rest on the treated grids for 30 – 60 seconds and then wicked away with filter paper. A JEOL 1230 TEM was used for imaging the particles. Representative images were collected from different areas of the grid. Structural features, such as circularity and Feret diameter, were characterized using the Analyze Particles plugin on ImageJ for ≥ 500 particles per

sample. A circularity threshold of 0.85 was used to define spherical particles and the Feret diameter corresponds to the largest tip-to-tip distance on a particle. Branch length was measured manually from the tip to the base of the branch.

3.4.3 Density Gradient Centrifugation

Linear sucrose density gradients were formed using a gradient maker (BioComp Instruments) with 9 mL starting solutions of 50% and 60% (w/v) sucrose in water. A custom mixing program alternated 5 times between the following two steps: (1) time: 5 seconds, angle: 76° , speed: 30 RPM; (2) time: 15 seconds, angle: 76° , speed: 0 RPM. Step gradients were layered by hand using solutions of 50%, 52.5%, 55%, 57.5% and 60% w/v sucrose in water. For the first round of DGC, 500 μ L of a concentrated solution of bare AuNS (8 – 10 nM) was layered on top of the density gradient in an Ultra-Clear SW28 centrifuge tube (Beckman Coulter), then centrifuged at $4400 \times g$ for 90 min using a Thermo Fisher Scientific Sorvall Legend XT 120v Benchtop centrifuge. The samples were fractionated at intervals of 4 mm from the meniscus (BioComp Instruments). Each fraction was dialyzed in Thermo Fisher 20K Slide-A-Lyzer™ Dialysis Cassettes for 24 h to remove sucrose from the solution.

For round 2 of DGC, we repeated round 1 DGC 20 times and odd-numbered fractions were combined and concentrated to form 400 μ L of 8 – 10 nM solution. We collected each fraction over the 20 individual rounds of DGC and analyzed only the final distributions of branch number and length of the combined fractions. Each of the combined fractions was layered on top of a linear 50 – 55% (w/v) sucrose gradient and the centrifugation time was set to be 45 min at $4400 \times g$. We note that reproducibility and scalability of this technique is demonstrated by the uniformity of the fractions which were combined from 20 rounds of DGC.

CHAPTER 4:
LABEL FREE PARTICLE-BY-PARTICLE QUANTIFICATION
OF DNA-LOADING ON SORTED GOLD NANOSTARS

This chapter is based, in part, on the research described in the following publication:
*Eller, M.J.; *Chandra, K.; Odom, T.W.; Schweikert, E.A.; Label Free Particle-By-Particle
Quantification of DNA-Loading on Sorted Gold Nanostars *In Preparation to submit to*
Analytical Chemistry *Equal Contributions

4.1 Introduction

An emerging application area of gold (Au) nanoparticles is their use in biological systems due to their various attractive properties. Attaching molecules like DNA to the surface of nanoparticles gives the particles stability in culture media¹⁴¹⁻¹⁴² and functionality.¹⁴³⁻¹⁴⁶ The chemical properties of molecules tethered onto non-spherical nanoparticle depend on the local curvature and shape of the particles.¹⁴⁷⁻¹⁴⁸ Nanoparticle curvature has been shown to affect the structure of absorbed proteins¹⁴⁹ and change ligand distribution and concentration.^{148, 150-151} The latter alters the therapeutic efficacy of each nanoparticle.^{107, 152} Specifically, nanoparticles with high surface area to volume ratios have a greater number of ligands per particle, which changes how the nanoparticle interacts with a cellular system.¹⁵²⁻¹⁵⁵ Therefore, studying the fundamental interactions between single nanoparticles and ligands could reveal new information on multivalent effects and energy-charge transfer.¹⁵⁶⁻¹⁵⁸

Since the contrast between the heavy metal nanoparticle and low-Z elements of the ligand¹⁵⁹ is too large to visualize both through electron microscopy, quantifying the ligand distribution on the single-particle level has proven challenging. Consequently, current quantification of ligand distribution on metal nanoparticle surfaces is limited to: (1) indirect measurements (e.g. unbound ligand SERS detection¹⁶⁰); (2) labeling the ligands (e.g. fluorescently tagged ligands¹⁶¹⁻¹⁶³ or dye molecules¹⁶⁴); or, (3) elemental analysis (e.g. Au and S via inductively coupled plasma mass spectrometry, ICPMS¹⁶⁵). These ensemble quantification methods average differences between heterogenous and anisotropic particles. For accurate analyses, nanoconstructs should be analyzed particle-by-particle. While single particle measurements of fluorophore-labeled ligands have been achieved,^{161, 166} quantifying a large number of particles with such methods is limited. To gain

statistically relevant data and determine how curvature influences ligand properties, high throughput measurements should be taken on intact, individual particles.

Time of flight secondary ion mass spectrometry, TOF-SIMS, is uniquely suited for analyzing nanoscale surfaces due to high lateral (ca. 100-400 nm) and depth resolution (ca. 5-10 nm).¹⁶⁷⁻¹⁶⁸ To analyze single nanoparticles we used a variant of TOF-SIMS with individual projectiles termed event-by-event bombardment/detection mode. The method has two innovative features: (1) the mode of bombardment, and (2) the recording of the secondary ions. This technique bombards a surface with relatively massive 2-nm projectiles (Au_{400}^{4+}), which produces abundant emissions of secondary ions from the sample.¹⁶⁹ Bombarding with one projectile at a time and recording the secondary ions from each impact *separately* allows for evaluation of ions co-emitted from 10 – 15 nm in diameter and up to 10 nm in depth. This one-of-a-kind tool is suited for the quantification of ligand distribution on an individual metal nanoparticle, regardless of nanoparticle morphology and method of ligand attachment.¹⁷⁰ By stochastically sampling with a few million projectile impacts, statistical tools can be used to evaluate correlations among co-emitted species and the ligand distribution.

In this work, we *directly* quantified label-free ligands on single nanoparticles of different morphologies, specifically Au nanostars (AuNS) and nanospheres. TOF-SIMS with individual projectiles was used to quantify the number and position of bound ligands in positive, negative or neutral nanoconstruct surfaces. The ligand loading on the AuNS was compared to spherical particles with similar surface area. We determined that negative particle curvature caused steric and conformational hindrance of the ligands and prevented high loading efficiency. Through these methods, we simultaneously collected information about the attached ligands and inorganic core.

4.2 Results and Discussion

4.2.1 Separation and Characterization of Sorted HEPES AuNS

AuNS were synthesized using 100 mM of the Good's buffer 4-(2-hydroxyethyl)-1-piperazineethanesulfonic acid (HEPES) and 0.2 mM HAuCl₄. We selected these conditions since this HEPES concentration produced heterogeneous AuNS with 0 – 8 branches and varying negative curvature (**Figure 4.1, Figure 4.2**). We quantified the DNA distribution on a 50-nm nanosphere due to the similar average volume and surface area. AuNS were sorted through rate-zonal density gradient centrifugation (DGC) using our previously established methods¹⁰⁹ based on differences in sedimentation rates, which are due to particle size and shape. Particles with a greater number of branches, longer branches, and larger overall size tended to sediment to the bottom of the gradient, while particles closer in shape to a small sphere moved more slowly through the gradient. These characteristic differences between nanospheres and heterogeneous AuNS allowed for sorting based on structural features.

After centrifuging AuNS through the linear gradient, samples were fractionated at intervals of 4 mm (ca. 2 mL) from the meniscus 15 times. The corresponding fractions were collected and labeled F1 to F15. Rate-zonal separation efficiency depended on particle shape, characterized by number of branches per particle for AuNS. F2 through F10 contained a high intensity of AuNS in the fractions. We categorized fractions into branch-number populations: low (0 – 2), medium (3 – 5), and high (≥ 6). We observed a decrease in the percentage of spheres from 18% to 3% from F2 to F10 and an increase in high branch-number populations. Rate-zonal separation created enriched populations of AuNS; each fraction showed greater particle homogeneity than the unsorted solution. Additionally, the fractions exhibited different surface area per volume of particles, which

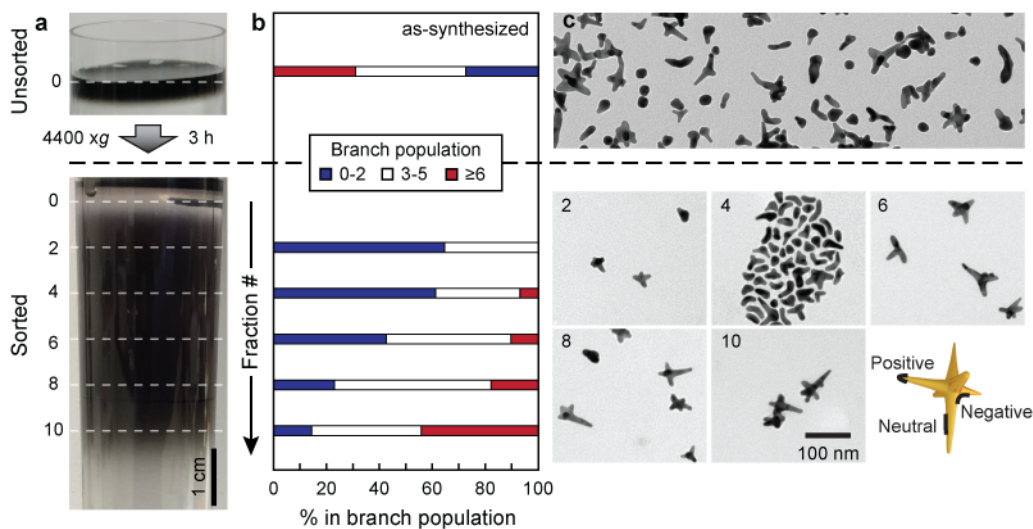


Figure 4.1: Density gradient centrifugation (DGC) isolates populations of AuNS with similar morphologies. (a) Photographs of a centrifuge tube before (top) and after (bottom) centrifugation of a concentrated AuNS solution in a sucrose linear density gradient. (b) Branch number distribution within each fraction based on manual branch counting of ≥ 400 particles per fraction. (c) TEM images of unsorted AuNS (top) and different fractions after DGC (bottom). The cartoon scheme denotes different areas of curvature (i.e. positive, negative, or neutral) on a AuNS.

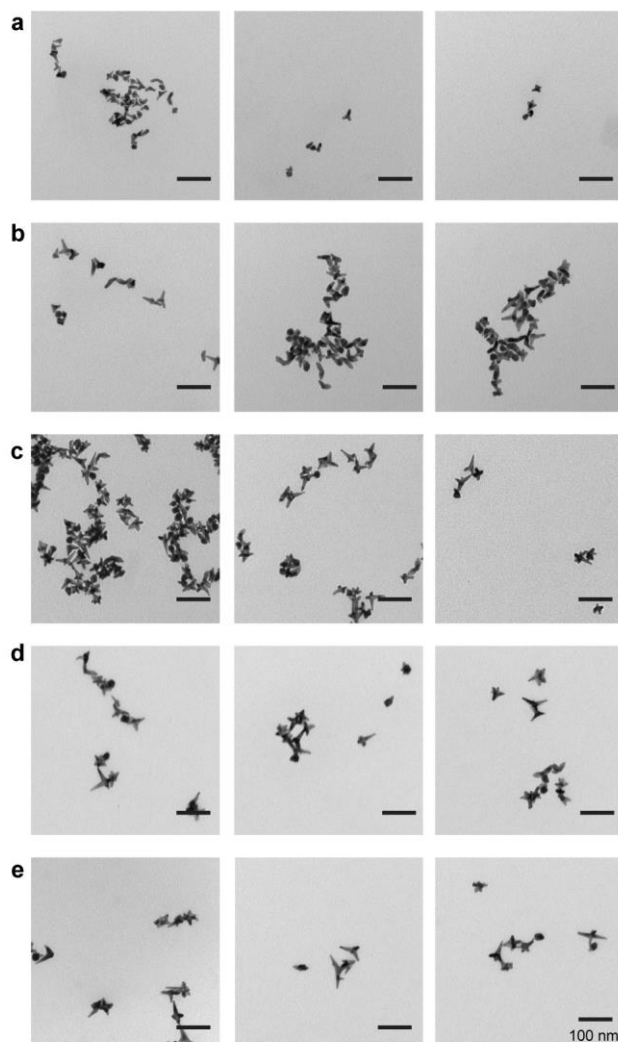


Figure 4.2: Low-magnification TEM images of sorted HEPES AuNS. Zoomed-out images of 100 mM HEPES AuNS sorted through DGC in fractions (a) 2, (b) 4, (c) 6, (d) 8, and (e) 10. All scale bars are 100 nm. These images demonstrate the difference in particle shape of the sorted AuNS.

demonstrated curvature change between the fractions (**Figure 4.3, Figure 4.4**). With an increase in fraction number, an increase in branch number, branch length, and overall volume of the particles increased. On a per particle basis, the volume increased at a greater rate than the surface area with an increase in fraction number.

4.2.2 Quantification of Co-Emitted Species

We functionalized every other AuNS fraction (F2 - F10) and 50-nm nanospheres with a single strand poly-T DNA and analyzed them with TOF-SIMS with individual projectiles. As described previously, each mass spectrum was composed of chemical information from isolated individual particles (event-by-event bombardment/detection mode) (**Figure 4.5, Figure 4.6**). From these mass spectra, characteristic ions were grouped together based on type of species: carbon (purple), the silicon support (orange), AuNS (black), DNA (pink), and salt (green) (**Figure 4.7, Figure 4.8**). From the silicon support, two silicon oxide clusters were observed: SiO_3H^- and $\text{Si}_2\text{O}_5\text{H}^-$. Salt clusters formed due to preparation in aqueous conditions, Na_xCl_y^- . Three types of ions related to the nanoconstruct were observed: nine peaks related to the AuNS ($\text{Au}_n^{-n} = 1$ to 9), seven peaks related to the DNA ligands (PO_2^- , PO_3^- , CN^- , CNO^- , $\text{C}_5\text{H}_5\text{N}_2\text{O}_2^-$, $\text{C}_5\text{H}_5\text{N}_2\text{O}_2\text{PO}_2\text{C}_4\text{H}_6\text{O}^-$, and $\text{C}_5\text{H}_6\text{N}_2\text{O}_2\text{PO}_4\text{C}_5\text{H}_7\text{O}^-$) and four peaks related to the Au-DNA adducts (AuCN^- , $\text{Au}(\text{CN})_2^-$, Au_2CN^- , and AuPO_2^-).

To evaluate the co-localization of species on the sample, we measured ions that were co-emitted and correlated the rate of simultaneous occurrence. **Figure 4.9 – 4.14** displays heat maps for F2, F4, F6, F8, F10, and 50-nm spheres; all the evaluated ions were correlated with their co-emitted species (coincidence ions). Positive correlation indicated co-localization (red) and negative correlation indicated segregation (blue). Using Equation 1, the correlation coefficient

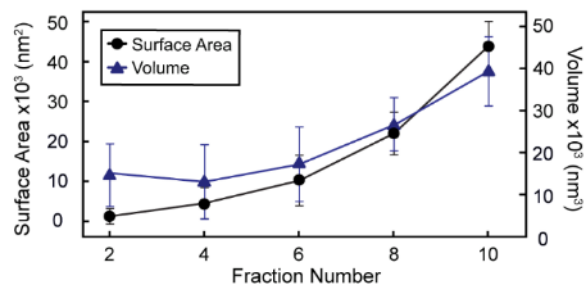


Figure 4.3: The surface area and volume per particle in each AuNS fraction.

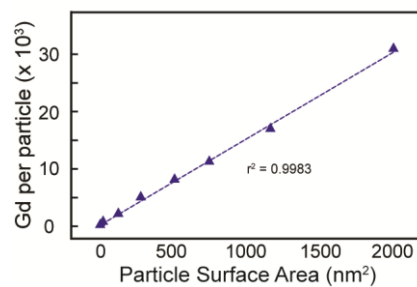


Figure 4.4: Gd-nanoparticle surface area standard curve. Gold nanospheres (2 – 150 nm in diameter) with known surface area were functionalized with Gd-chelate. Through ICPMS, the amount of Gd per particle was determined. This standard curve was used to determine the surface area of the sorted AuNS particles.

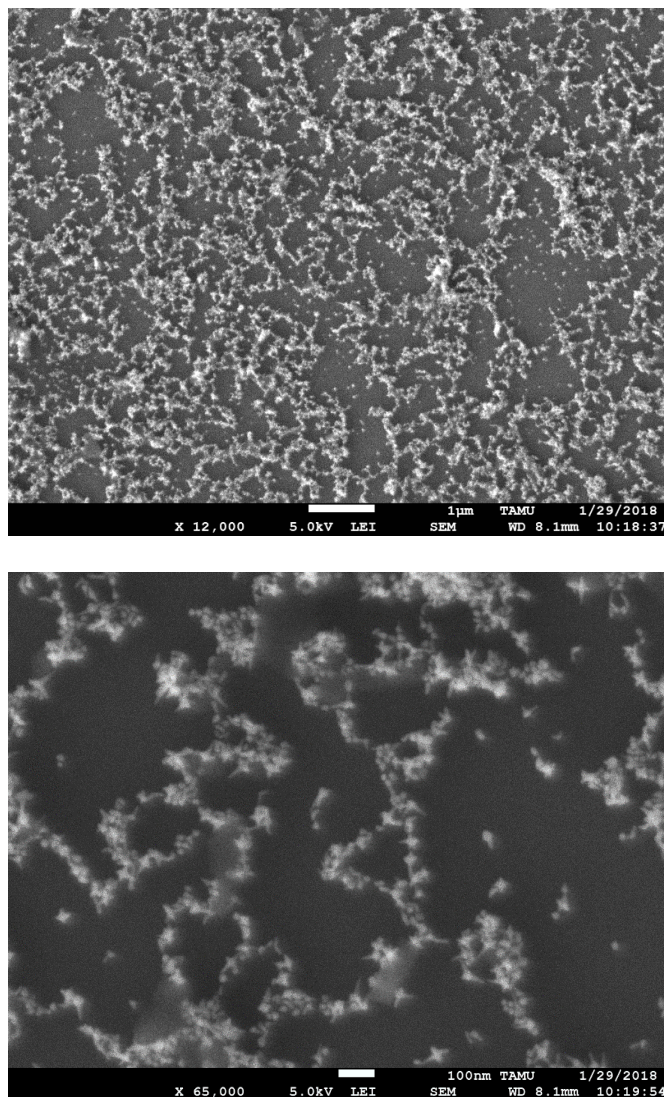


Figure 4.5: SEM image of F4 AuNS as prepared for SIMS analysis. (a) At 12 K, the images show that the nanoparticles organize on to the surface in small groups after deposition. **(b)** At 65 K, higher resolution reveals the distribution of individual particles on the surface. AuNS connect in long chains with a few particles completely isolated on the substrate.

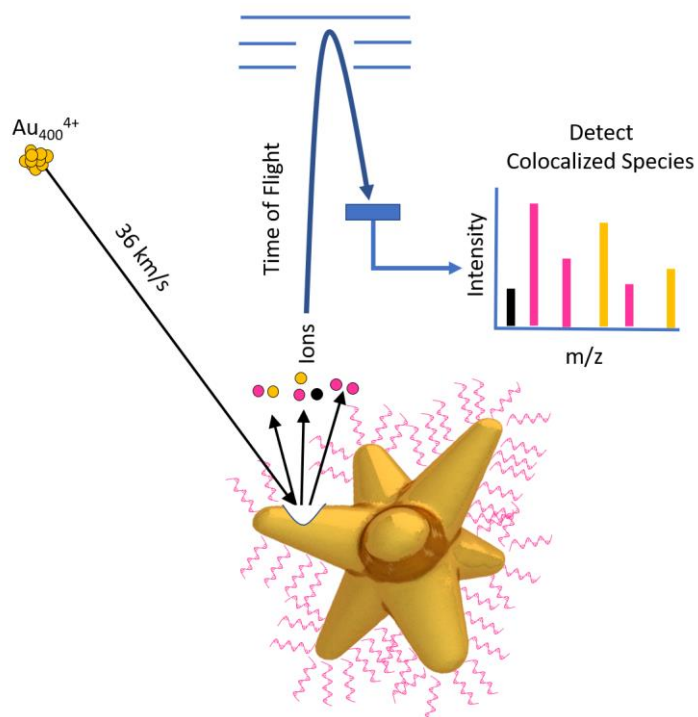


Figure 4.6: Schematic of cluster SIMS experiment. Each projectile is separated in time and space, and upon impacting the sample causes emission from a volume 10-15 nm in diameter. For each projectile impact the co-emitted ions are mass analyzed by TOF and collected in a mass spectrum.

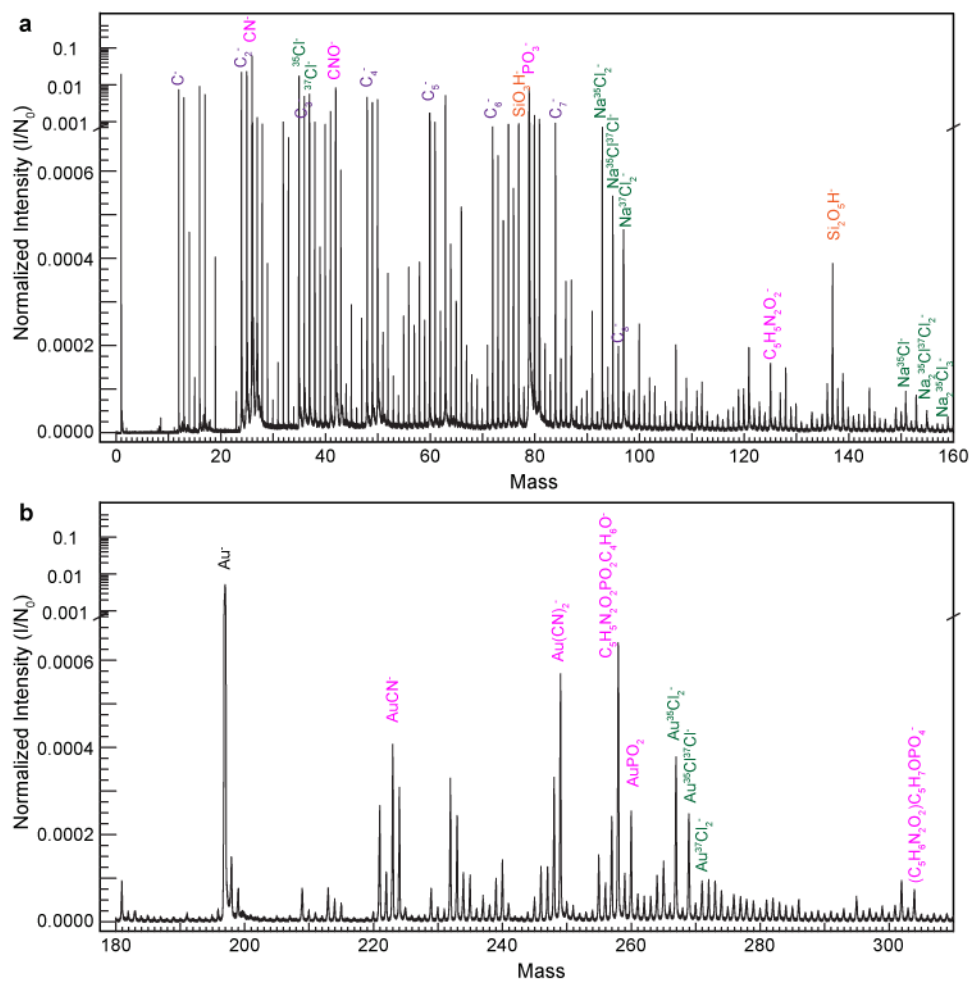


Figure 4.7: Mass spectra identified notable peaks of functionalized AuNS. Notable peaks are identified and color coded: purple are carbon clusters, pink are DNA related, orange are silicon related, green are salt, and black are Au clusters.

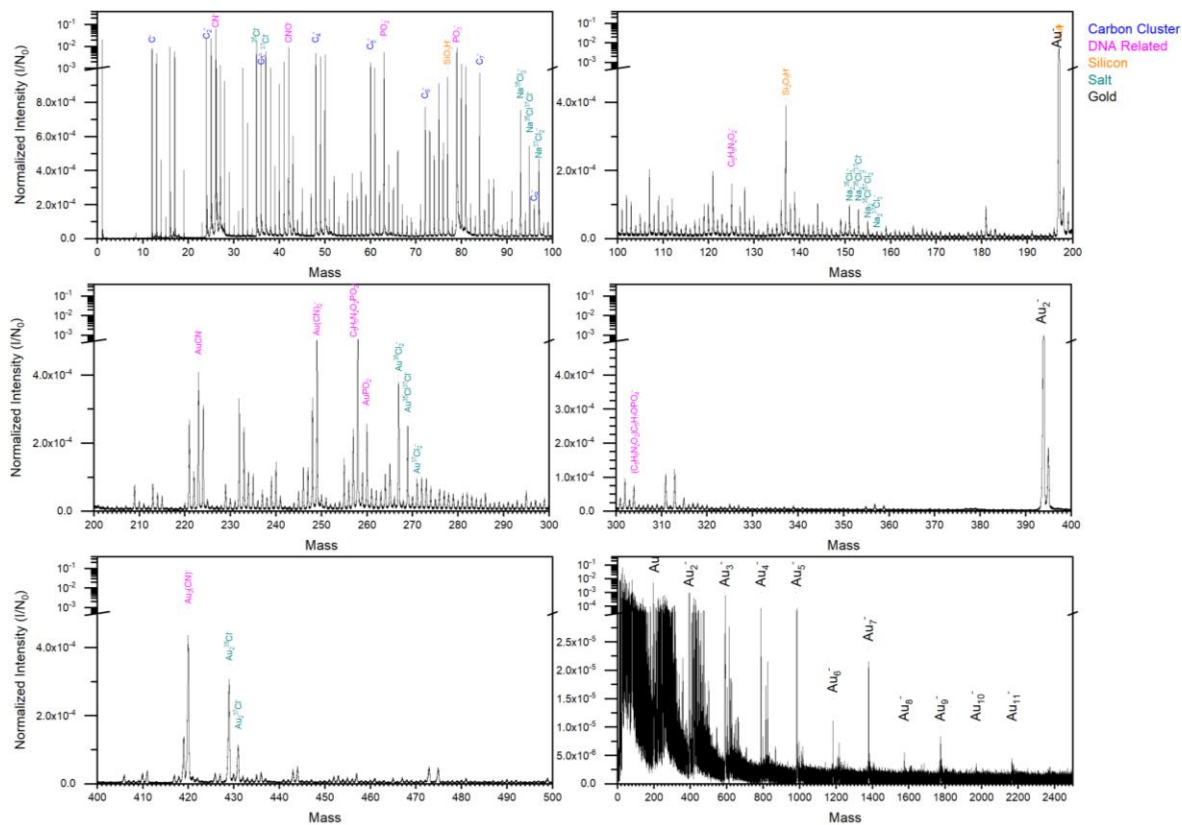


Figure 4.8: Mass spectrum of F4 AuNS. Each panel shows a different mass range and the y-axis is the intensity divided by the number of projectile impacts. Notable peaks are identified and color coded. Pink peaks are related to the DNA, black are gold clusters, orange are related to the silicon support, green are sodium chloride clusters, and blue are carbon clusters.

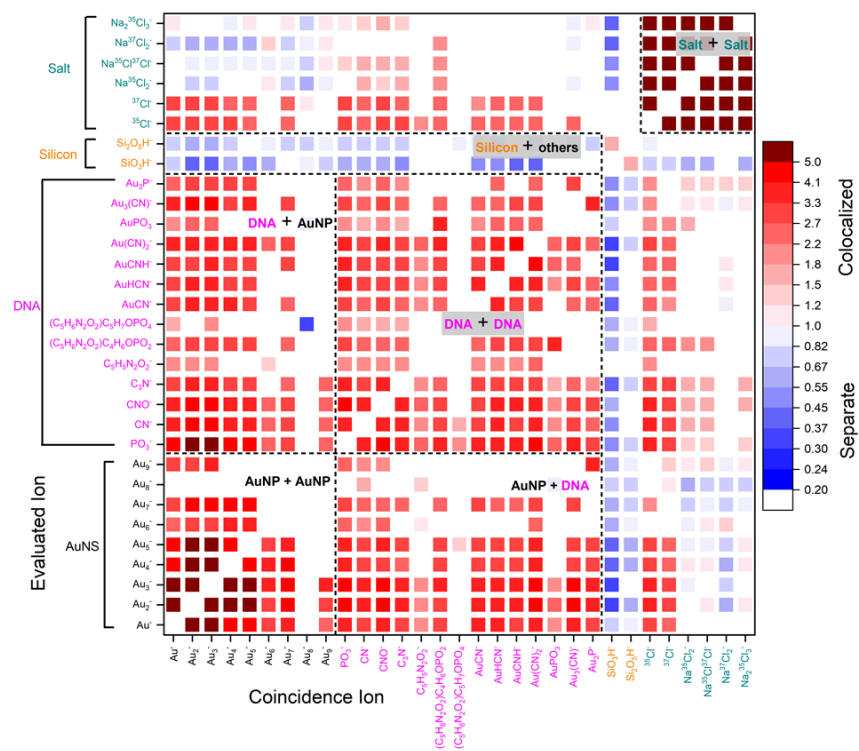


Figure 4.9: Two-dimensional correlation heat map for F2 AuNS. The color scale is correlation coefficient, with red corresponding to positive correlation and blue to negative correlation. Ions which do not have a significant correlation were not plotted. The evaluated ions are listed on the y-axis, the coincidental mass spectrum is listed on the x-axis.

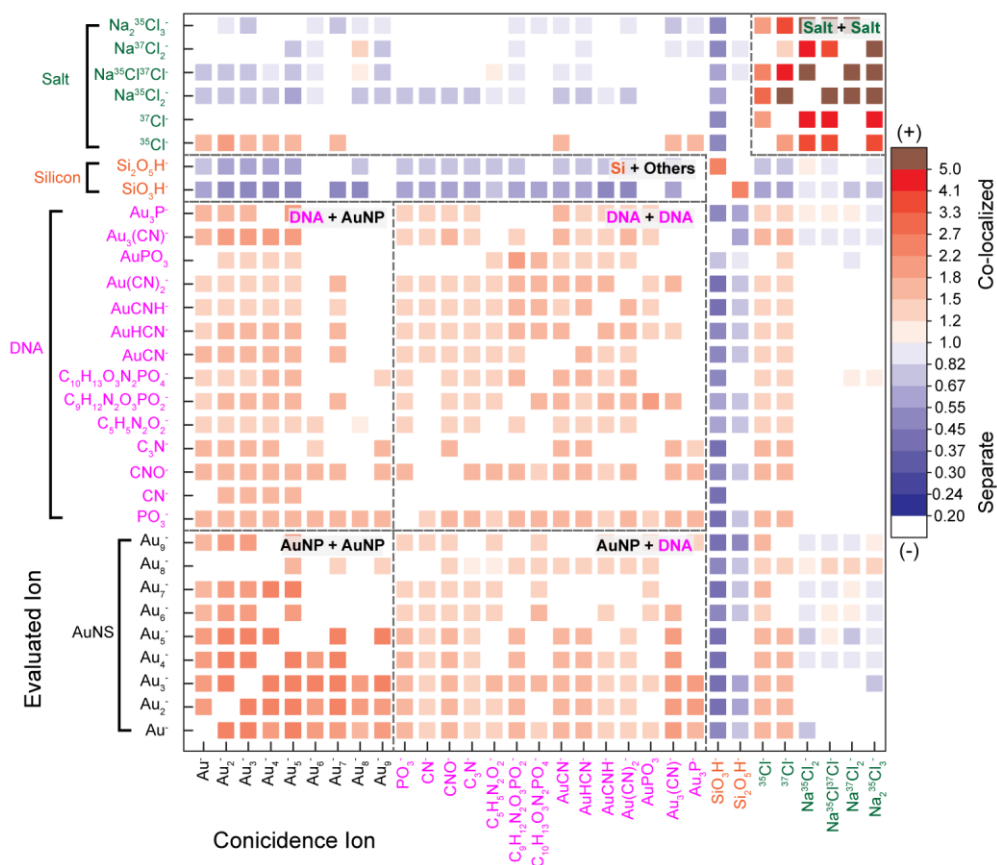


Figure 4.10: Two-dimensional correlation heat map for F4 AuNS. The color scale is correlation coefficient, with red corresponding to positive correlation and blue to negative correlation. Ions which do not have a significant correlation were not plotted. The evaluated ions are listed on the y-axis, the coincidental mass spectrum is listed on the x-axis.

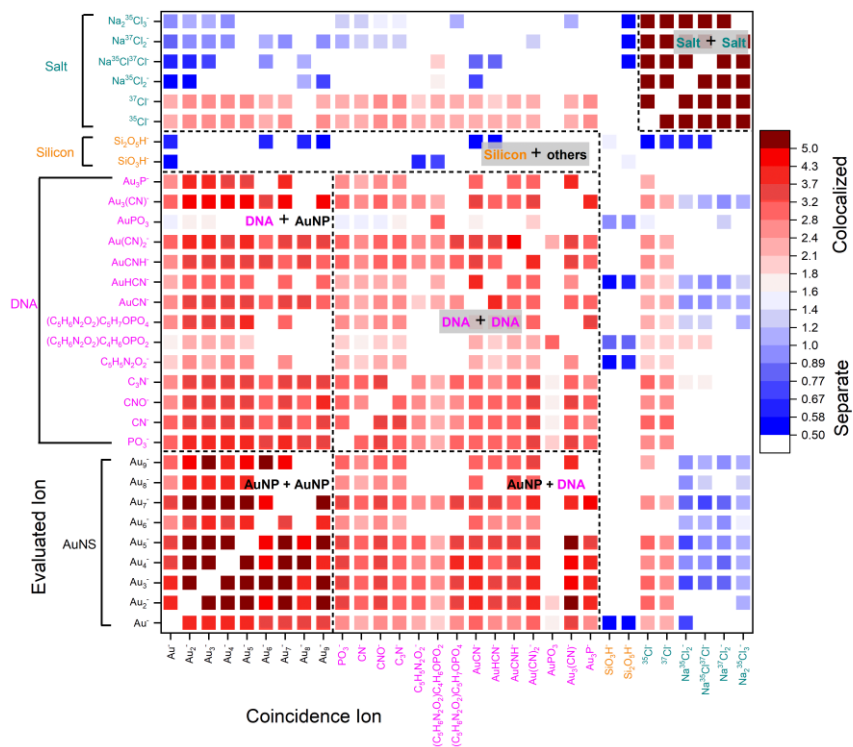


Figure 4.11: Two-dimensional correlation heat map for F6 AuNS. The color scale is correlation coefficient, with red corresponding to positive correlation and blue to negative correlation. Ions which do not have a significant correlation were not plotted. The evaluated ions are listed on the y-axis, the coincidental mass spectrum is listed on the x-axis.

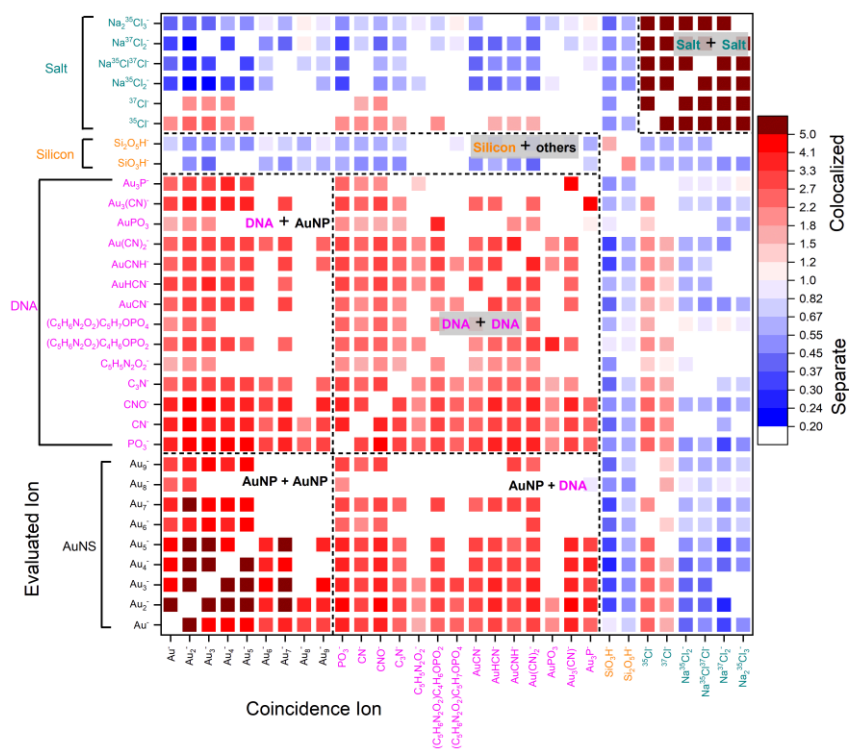


Figure 4.12: Two-dimensional correlation heat map for F8 AuNS. The color scale is correlation coefficient, with red corresponding to positive correlation and blue to negative correlation. Ions which do not have a significant correlation were not plotted. The evaluated ions are listed on the y-axis, the coincidental mass spectrum is listed on the x-axis.

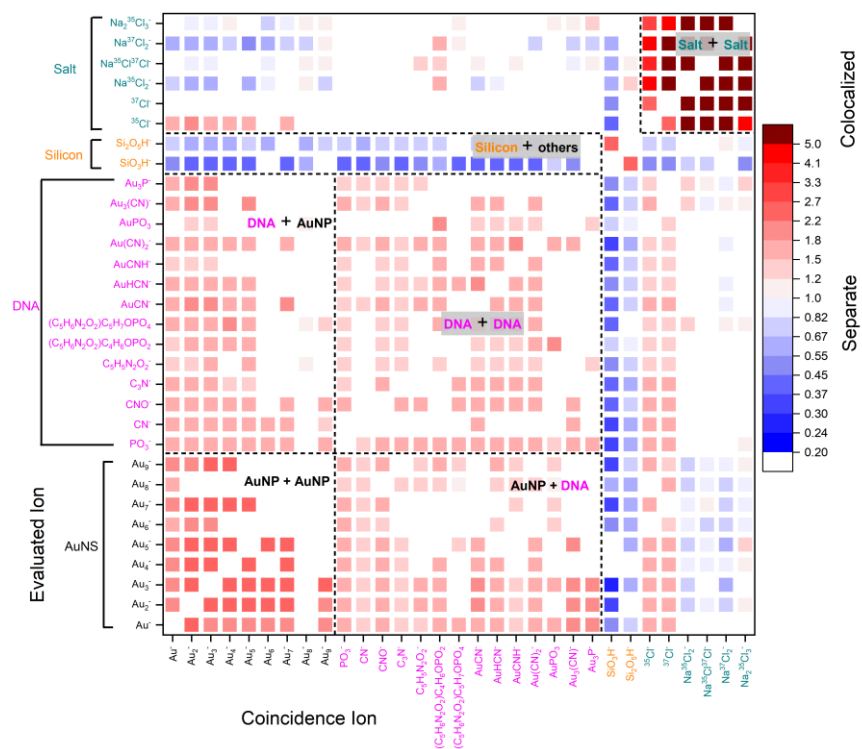


Figure 4.13: Two-dimensional correlation heat map for F10 AuNS. The color scale is correlation coefficient, with red corresponding to positive correlation and blue to negative correlation. Ions which do not have a significant correlation were not plotted. The evaluated ions are listed on the y-axis, the coincidental mass spectrum is listed on the x-axis.

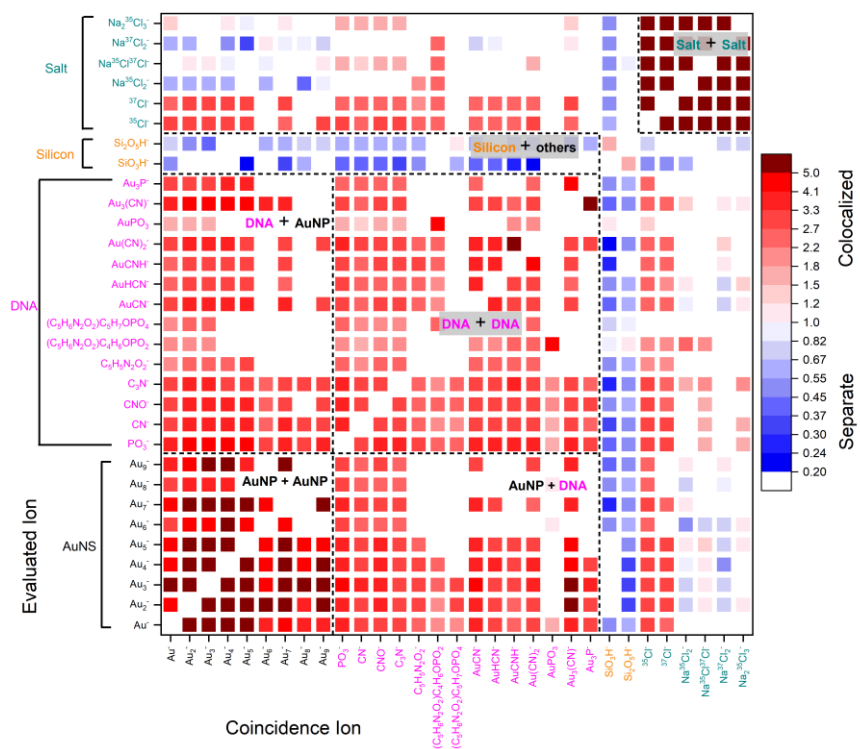


Figure 4.14: Two-dimensional correlation heat map for 50-nm spheres. The color scale is correlation coefficient, with red corresponding to positive correlation and blue to negative correlation. Ions which do not have a significant correlation were not plotted. The evaluated ions are listed on the y-axis, the coincidental mass spectrum is listed on the x-axis.

between two ions (a , b) was determined and tested against a random correlation and with a 99% confidence interval:

$$\frac{I_{a,b}}{I_a * I_b} = \text{correlation coefficient} \quad (4.1)$$

Where I_a is the intensity of a ; I_b is the intensity of b ; and $I_{a,b}$ is the intensity of the co-emission of a with b . This correlation test was performed pair wise on all characteristic ions. To demonstrate that all DNA co-emissions were captured, all regions of the sample were identified and displayed, including the silicon wafer and salt crystals. All types of ions were negatively correlated with the silicon oxide clusters, which indicated open regions of the wafers where only silicon species were co-localized. This illustrated that the nanoconstructs were isolated on the surface, which ensured measurements occurred on individual particles. Additionally, we found that NaCl clusters were positively correlated with one another due to salt crystal formation; however, they exhibited negative correlation with all other species. This correlation demonstrated that the salt crystals were not involved in the DNA or AuNS measurements but were still included in the sample evaluation. Since all regions of the sample were identified, the plot shows where DNA was localized on the sample.

AuNS are represented by the small Au clusters (Au_n , $n= 1-9$) in the lower left corner of the heat map. AuNS and DNA-related ions were positively correlated to one another and to themselves. Overall, DNA related species and Au clusters exhibit the same correlation coefficients and have similar relationships to salt and silicon related ions. Since positive correlation means the secondary ions were co-emitted in the same impacts, the DNA and AuNS were within 10 – 15 nm of one another. These results definitively demonstrate that the DNA was co-localized on the surface with the AuNS. By examining these impacts, we evaluated the extent of ligand loading on the AuNS.

In SIMS, the observed intensity of an ion is a product of the number of ejected molecules, the chance that a molecule or fragment will become charged (ionization probability), the transmission of the mass spectrometer, and the detection efficiency; thus, the intensity does not directly reflect the species concentration. Comparing the intensity of an ion between different samples proves challenging, because changes in the chemical environment may affect ionization probability and skew the results. In equation 1 (correlation coefficient) and equation 2 (homogeneity), the ionization probability of each ion appears in both the numerator and denominator and therefore does not affect the calculation.¹⁷¹ Therefore a comparison of the homogeneity or correlation coefficient between samples can be performed.¹⁷⁰ We evaluated the homogeneity of each component by identifying ions which originate from the same types of impacts, i.e. ones which have a positive correlation coefficient. We then determined the fraction of impacts containing the two species together using the following equation:

$$\frac{I_a * I_b}{I_{a,b} * N_0} = \text{homogeneity} \quad (4.2)$$

Where I_a is the intensity of a ; I_b is the intensity of b ; $I_{a,b}$ is the intensity of the co-emission of a with b ; and N_0 is the number of measurements. The sum of the silicon, salt, DNA, and Au on each sample gives 1.0 ± 0.1 , indicating that all regions of the sample were identified (**Figure 6**). The DNA homogeneity was in good agreement with the DNA/Au homogeneity, which verified little free DNA not attached to AuNS.

AuNS homogeneity was calculated for all samples by selecting impacts where two Au species were co-emitted. The results for F4 are presented in **Figure 6** and all others are presented in the supporting information. For all samples, we note that the AuNS homogeneity is approximately 65% that of Au with DNA. This underestimation was due to two effects. First, AuNS coated with a

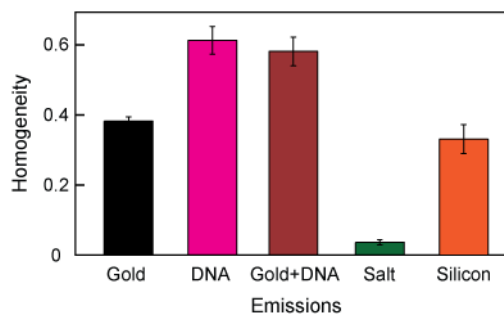


Figure 4.15: Emission homogeneity demonstrated 100% surface coverage. The sum of the silicon, salt and DNA/gold on all samples gives ca. $1 \pm .1$ (100 %), which indicates all the regions of the sample surface were identified. Good agreement between the DNA + Gold and DNA homogeneity was found, signifying most of the DNA was bound to the particles. This is a representative homogeneity graph for the F4 AuNS sample.

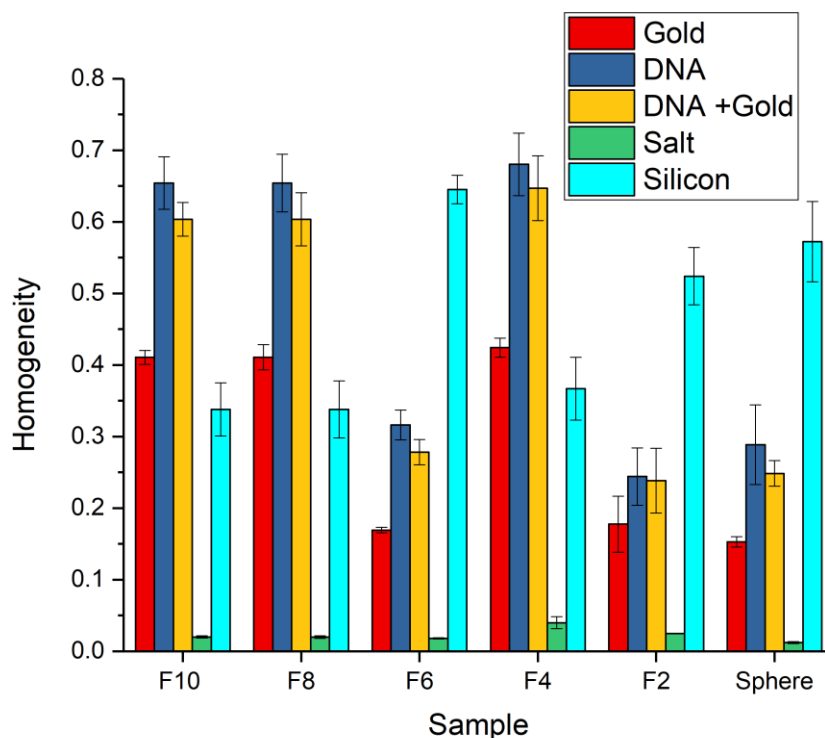


Figure 4.16: Homogeneity of each nanoparticle sample. The surface composition was determined for each sample using the methodology described in the article. In each sample the composition of the surface is composed of exposed silicon, sodium chloride, and gold particles. In all cases there is good agreement between DNA and DNA plus gold, indicating little or no unbound DNA was deposited on the surface. Additionally, the summation of silicon, sodium chloride and DNA plus gold gives 1.0 ± 0.1 showing all regions of the surface were identified. The absolute number of deposited gold particles depends on the initial concentration in solution and the deposition area.

single-stranded 15mer Poly-T DNA may result in decreased emissions from underlying regions. For areas where ligands were bound to the nanoparticle, the Au₄₀₀⁴⁺ projectile interacts with the ligand before striking the AuNS surface, resulting in decreased Au emission. Second, the emission of Au clusters was affected by the asymmetric shape of the AuNS. The core of a particle has a greater density of Au atoms than the branches. Therefore, impacts occurring on the core emit more gold than those occurring on the branches.¹⁷² These two effects, ligand coating and anisotropic shape, resulted in fewer impacts where two or more Au clusters were co-emitted. Hence, to compare the relative DNA distribution on different AuNS samples, we measured the relative coincidence yield and normalized it to the 50-nm nanospheres.

4.2.3 Determination of DNA Distribution Per Particle on Varying Morphologies

To determine the DNA distribution on the particles, we selected a gold cluster that was detected in all nanoconstruct samples. Then, measured the number of DNA ions that were co-emitted with the cluster; therefore, differences in DNA loading among nanospheres and sorted AuNS were evaluated. The approach only evaluates impacts occurring on the nanoconstructs, while avoiding ones containing the silicon support or salt. Using equation 3, we evaluated the coincidental yield of DNA ions when a gold cluster was detected to determine DNA loading per particle:

$$\frac{I_{a,b}}{N_{i,b}} = CY_{a,b} \quad (4.3)$$

Where $I_{a,b}$ is the intensity of the co-emission of a with b ; $N_{i,b}$ is the number of impacts where b was detected; and $CY_{a,b}$ is the coincidental yield of a in impacts where b was detected. The CY is correlated to the ligand loading per particle.

The DNA loading of each AuNS fraction, represented through CY, was compared to the 50-nm nanospheres to determine shape or curvature effects, by dividing the CY_{AuNS} by the $CY_{50\text{-nm spheres}}$. The $CY_{\text{AuNS}}/CY_{50\text{ nm spheres}}$ ratio for $C_5H_6N_2O_2PO_4C_5H_7O^-$ co-detected with Au_7^- is presented in **Figure 4.17**. The dashed line at 1.0 represents the loading of a 50-nm sphere. The results showed that the CY (i.e. ligand loading per particle) was higher in all AuNS fractions compared to the spheres, potentially due to branches allowing for additional DNA molecules to be attached per particle, thereby increasing loading efficiency. A similar trend was found for all DNA related species.

F4 AuNS displayed the highest relative CY, i.e. the most DNA functionalized on a single particle. F4 AuNS contained on average 3 branches, which increased the surface area per particle compared to a 50-nm sphere but limited negative curvature; this morphology optimized DNA functionalization on the particles. F2 had an average of 1 branch per particle and a higher percentage of nanospheres (diameter ~ 10 nm), which limited overall surface area per particle, leading to the lowest loading. Above F4, the number of branches increased and formed more regions of negative curvature where the branch meets the core. We hypothesize that an increase in negative curvature causes a decrease in DNA loading, due to steric hinderance.

The results presented show that particle size and curvature influence ligand loading, specifically the abundance of positive and negative curvature. To optimize ligand loading, particle geometries with an abundance of positive curvature should be considered. The size and length of target ligand would also need to be considered when determining the size and curvature of the nanoconstruct.

We have shown that by using event-by-event bombardment/detection TOF SIMS the extent of ligand loading can be evaluated on sorted nanoparticles. Previous experiments have shown that particle size and shape alters the intensity and relative abundance of metal clusters emitted from metal particles.¹⁷³⁻¹⁷⁴ Therefore identifying impacts on particles with similar size and shape from a mixture of particles should be feasible.

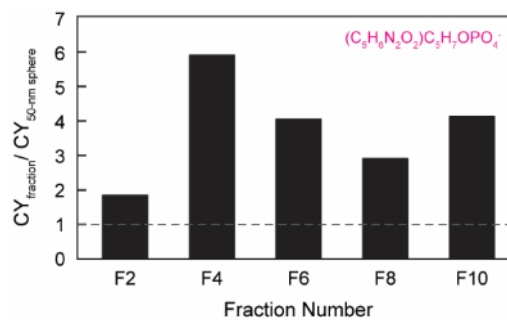


Figure 4.17: Coincidental yield for particles of varying morphology. The CY ratio for the for the deprotonated thymine nucleotide and a fragment of the nucleotide at m/z 248 compared to the 50-nm spheres. F4 demonstrated $6\times$ enhancement of loading compared with spheres as shown through ratio of the CY of deprotonated nucleotide.

4.3 Summary

This study carried out on size-selected AuNS demonstrates the ability of event-by-event bombardment/detection TOF-SIMS to determine shape dictated DNA loading. We found that the amount of functionalized DNA on the nanoparticles depended on their size and curvature. AuNS with branches increased the amount of loaded DNA versus 50-nm Au nanospheres. However, a greater branch-number sterically hindered additional attachment, especially in regions of negative curvature where the branch meets the core. This methodology can be universally applied to probe any ligand-nanoparticle interaction and may be further developed to evaluate ligand loading with the concurrent identification of an individual particle's size and shape.

4.4 Experimental Methods

4.4.1 Nanoparticle Synthesis

The Good's buffer used was 4-(2-hydroxyethyl)-1-piperazineethanesulfonic acid (HEPES buffer, Sigma Aldrich, St. Louis, MO, USA). The 1-M stock HEPES solution was made by dissolving the buffer salt in Millipore water ($18.2 \text{ M}\Omega\cdot\text{cm}$) using a medium-sized stir bar to ensure thorough mixing. The pH of the HEPES solution was measured using a Thermo Scientific pH meter and was adjusted using concentrated solutions of NaOH. For fine pH adjustments, HCl was added dropwise. AuNS were synthesized by adding 0.2 mM (final concentration) gold (III) chloride trihydrate (HAuCl_4 , Sigma Aldrich) to 100 mM of HEPES buffer. Each solution was vortexed in a 50-mL Falcon tube for one minute before addition of HAuCl_4 and for 1 minute afterwards. After vortexing, the growth solution was left undisturbed at room temperature for 24 hours. Au nanospheres of varying diameters (5, 10, 20, 30, 40, 60, 80, 100, and 150 nm) were purchased from Sigma Aldrich.

4.4.2 Particle Characterization Techniques

3 mL of AuNS solution was placed in a 1-cm plastic Brookhaven cuvette and the absorbance spectra was measured from 400 nm to 1400 nm using a Cary 5000 UV-vis-NIR spectrophotometer (Agilent Technologies, Santa Clara, CA, USA).

For TEM grid preparation, carbon Type B, 300 mesh copper grids (Ted Pella, Redding, CA, US) were treated with 0.1% (w/v) poly-L-lysine (Sigma Aldrich) for 5 minutes. 40 μ L of 10 times concentrated Au nanoparticle solution was left to rest on the treated grids for 30 – 60 seconds and then wicked away with filter paper. A JEOL 1230 TEM was used to image the particles with an 80 kV accelerating potential. Representative images were collected from different areas of the grid. Structural features, such as circularity and Feret diameter, were characterized using the Analyze Particles plugin on ImageJ for ≥ 500 particles per sample. A circularity threshold of 0.8 was used to define spherical particles. The Feret diameter, which corresponds to the largest tip-to-tip distance on a particle, was also measured. Branch length and number of branches were measured manually from the tip to the base of the branch.

4.4.3 Density Gradient Centrifugation

DGC was used to separate AuNS based on size and shape. The sorted AuNS were analyzed separately to understand how differences in shape and curvature (positive, negative, and neutral) affected DNA loading. Sucrose density gradients were formed using a gradient maker (BioComp Instruments) with 9 mL starting solutions of 50% and 60% w/v sucrose in water. Based on previous methods,¹⁷⁵ we created a linear gradient through a custom mixing program alternated 5 times between the following two steps: (1) time: 5 seconds, angle: 76°, speed: 30 rpm; (2) time: 15 seconds, angle: 76°, speed: 0 rpm. For DGC, 500 μ L of a concentrated solution of bare AuNS (35

– 40 nM) was layered on top of the density gradient in an Ultra-Clear SW28 centrifuge tube (Beckman Coulter), and then centrifuged at 4400g for 3 hours using a Thermo Fisher Scientific Sorvall Legend XT 120v Benchtop centrifuge. The samples were fractionated at intervals of 4 mm from the meniscus (BioComp Instruments). Each fraction was dialyzed in Thermo Fisher 20K Slide-A-Lyzer™ Dialysis Cassettes for 24 hours to remove sucrose from the solution. The as-synthesized and sorted solutions were characterized by UV-Vis spectroscopy to measure the bulk optical properties and by transmission electron microscopy (TEM) to visualize individual AuNS.

4.4.4 Functionalization of DNA to Nanoparticles

Each AuNS fraction and 50-nm Au nanospheres were functionalized with single-stranded 15mer Poly-T DNA by deprotection of the disulfide and salt-aging.¹⁰⁵ Functionalized nanoparticles were purified by three rounds of centrifugation (10 000 RPM, 10 min) and resuspension in Milli-Q water with 0.01% TWEEN.

4.4.5 Surface Area and Volume Characterization

We created a standard curve of surface area using 9 Au nanospheres (5, 10, 20, 30, 40, 60, 80, 100, and 150 nm) which were functionalized with Gd-chelates.¹⁰⁹ The Gd-chelate is a heavy metal that can be easily measured through by inductively coupled plasma mass spectrometry (ICP-MS). The nanosphere solutions and sorted AuNS fractions were vortexed with 100 × excess Gd-chelate for 12 – 24 hours with 0.01% TWEEN. The Gd-nanoparticle solutions were purified through three rounds of centrifugation (10 000 rpm, 10 minutes) and resuspension in Milli-Q water.

Au and Gd-chelate quantification was performed by acid digestion of samples followed by ICP-MS analysis on a Thermo iCap QC ICP-MS (Thermo Fisher Scientific, Waltham, MA, USA). ICP-MS samples were digested in 1:1 nitric acid:hydrochloric acid (Nitric acid, >69% ;

TraceSelect HCl, 37%). Milli-Q water and a multielement internal standard containing Bi, Ho, In, Li, Sc, Tb, and Y (Inorganic Ventures, Christiansburg, VA, USA) were added to produce a solution of 2% nitric acid (v/v), 2% HCl (v/v), and 5.0 ng/mL internal standard up to a final volume of either 3 or 10 ml. Serial dilutions of Gd and Au standards (Inorganic Ventures) were prepared in the same matrix as the samples. The Gd/AuNS were then interpolated on the Au nanoparticle standard to determine the surface area per particle.

Structural characterization was based on analysis of TEM images of AuNS which were taken from several areas on the grid to obtain representative populations. The branch number was manually counted from at least 10 different zoomed-out images for ≥ 400 particles in each fraction. AuNS volumes were approximated from TEM images of ≥ 300 particles per fraction using the Analyze Particles plugin of ImageJ.

4.4.6 Secondary Ion Mass Spectroscopy

Samples were stored at 4° C after synthesis. AuNS samples were prepared for SIMS analysis using the MarangoniFlow-Assisted method on cleaned 1 cm x 1 cm silicon wafers.¹⁷⁶ This method ensured sufficient isolation between individual particles to allow for single particle measurements, see supporting information.

SIMS analysis was done using a custom-built instrumentation. A simplified schematic of the experimental approach is presented in **Figure 1**, as detailed instrumental schematic has been presented previously.¹⁷⁰ A brief description of the instrumentation follows, the Au clusters were produced by a Au liquid metal ion source, LMIS, installed on a 120kV platform. From the range of Au projectiles produced by the LMIS, Au₄₀₀⁴⁺ was mass selected by a Wien filter. After exiting the platform, the beam of projectiles was pulsed a rate of 1000 impacts per second. Each projectile

then impacted the sample (biased to -10kV). From each impact the emitted electrons and secondary ions were extracted concurrently. The electrons were deviated by a weak magnetic field to a MCP-based detector and were the start of the time of flight (TOF) measurement. The secondary ions were mass analyzed by a reflectron TOF mass spectrometer equipped with a MCP-based eight anode detectors, which allows for up to eight isobaric ions to be detected from a single impact. The start and stop signals were collected by a multi-stop time to digital converter and stored in the PC as an individual mass spectrum. Samples were stochastically analyzed with $2 - 4 \times 10^6$ Au_{400}^{4+} projectiles on an area ca. $125 \mu\text{m}$ in radius, corresponding to $2 - 4 \times 10^6$ individual mass spectra for each sample. In the SIMS analysis ca. 0.3% of the surface was analyzed, thus each projectile impacts an unperturbed portion of the sample (super static regime).

CHAPTER 5:
DETECTING AND VISUALIZING REACTION INTERMEDIATES
OF ANISOTROPIC NANOPARTICLE GROWTH

This chapter is based, in part, on the research described in the following publication:
Chandra, K.; Rugg, B.; Ratner, M.; Wasielewski, M.; Odom, T.W.; Detecting and Visualizing
Reaction Intermediates of Anisotropic Nanoparticle Growth. *J. Am. Chem. Soc.*, **2018**, 140 (9),
3219–3222

5.1 Introduction

The physical and chemical properties of anisotropic gold (Au) nanoparticles are determined by their size and shape.^{56, 153} Conventional anisotropic Au nanoparticle syntheses occur in two steps: (1) nucleation of 2 – 5 nm spherical particles called seeds using a reducing agent; and (2) addition of these seeds to a separate solution containing a shape-directing agent for preferential growth.⁷⁰ The mechanism underpinning seed-based synthesis for Au nanorods and bipyramids using the shape-directing agent cetyltrimethylammonium bromide has been studied through *in situ* high-resolution transmission electron microscopy (TEM).⁷⁹⁻⁸⁰ In contrast, little is known how *seedless* syntheses allow for anisotropic nanoparticle growth in a one-pot solution.

Recently, a surfactant-less, seedless synthesis of Au nanostars (AuNS) has received increasing attention because only two precursors are required: Au salt (HAuCl₄) and a biocompatible Good's buffer, e.g. HEPES [4-(2-hydroxyethyl)-1-piperazine ethanesulfonic acid] or EPPS [4-(2-hydroxyethyl) piperazine-1-propanesulfonic acid].^{58, 96, 100} Although HEPES and EPPS show only a small difference in chemical structure (an additional carbon in the alkanesulfonate chain), the different buffers produced different branch-growth directions and a drastic differences in branch length (3 – 5 times).¹⁰⁰ HEPES acts as a shape-directing agent through the alkanesulfonate group that binds to the Au surface¹⁰³ as well as a reducing agent from the two nitrogen atoms. The reduction of Au(III) to Au(0) produces nitrogen-centered cationic free radicals.¹⁰¹ Based on the production of EPPS radicals in the presence of Fe(III) that created iron oxide nanoparticles,¹⁰² the mechanism for AuNS synthesis using EPPS is expected to be similar. Comparing the radical generation between HEPES and EPPS in the presence of HAuCl₄ could elucidate mechanistic differences that result in the final nanoparticle morphology. Additionally, outside of this specific

reaction, other seed-mediated¹⁷⁷⁻¹⁷⁹ and seedless¹⁸⁰⁻¹⁸² nanoparticle syntheses use radicals to reduce metal ions. Although widely used to study paramagnetic species,¹⁸³ electron paramagnetic resonance (EPR) spectroscopy has not been applied to characterize radical-based nanoparticle syntheses.

Here we report a correlative approach to detect and characterize intermediate species during the seedless growth of anisotropic AuNS. We integrated the intensity of the EPR signal resulting from radical generation and compared it with intermediate optical and structural properties of AuNS as a function of time. We found that type and concentration of Good's buffer determined whether one or two increases in radical generation were observed. The first increase in EPR signal related to the initial formation of particles, and the second corresponded to extended growth in branch length. EPR spectroscopy measurements of radical production *during the reaction* enable insight into key factors that contribute to seedless nanoparticle syntheses.

5.2 Results and Discussion

5.2.1 Proposed Mechanism for Radical Generation

Figure 5.1 depicts AuNS synthesis using two Good's buffers, HEPES or EPPS, in a single solution. The electron-rich piperazine group reduces the Au(III) to inert Au(0), which leads to particle formation.¹⁸⁴ Both buffers produced AuNS with 1 – 8 branches that were stable for ≥ 12 h from 100 – 500 mM buffer concentration (**Figure 5.2**). Above 500 mM, HEPES did not produce AuNS in solution, while EPPS could produce AuNS with high aspect ratio particles. To explain differences in particle shape, we compared HEPES and EPPS radicals at varying concentrations and correlated the results to optical properties and structure through UV-Vis and TEM.

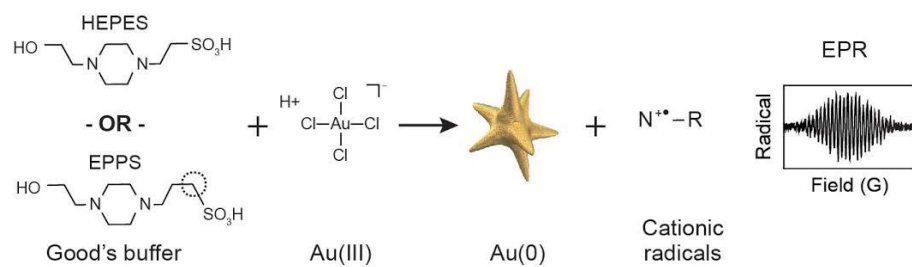


Figure 5.1: A chemical reaction scheme for the synthesis of AuNS with a Good's buffer (HEPES or EPPS), measured by EPR.

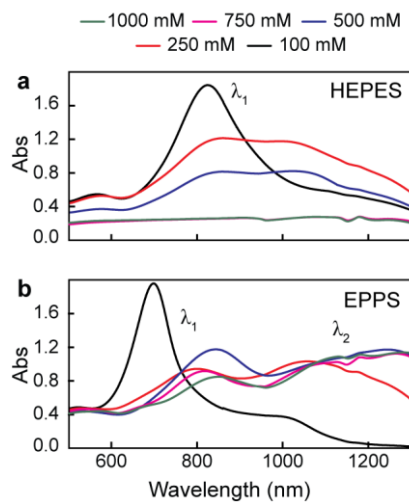


Figure 5.2: Absorption spectra of HEPES and EPPS at varying concentrations. (a) One injection of HAuCl_4 into 100 – 1000 mM HEPES produced solutions with one LSP peak, λ_1 . Above 500 mM [HEPES], the particles were unstable in solution and did not produce AuNS. (b) One injection of HAuCl_4 into 100 – 1000 mM EPPS produced solutions with two LSP peaks, λ_1 and λ_2 . For all [EPPS], the particles were stable in solution and produced AuNS.

5.2.2 Radical Generation Corresponded to a Plasmon Peak Shift and Particle Size Increase

First, we examined the reaction of 100-mM HEPES and 0.2-mM H₂AuCl₄ since these concentrations produced the smallest, stable AuNS (Figure S1a). This H₂AuCl₄ concentration was used in all subsequent reactions. Pure HEPES and aqueous H₂AuCl₄ produced no radical signal (**Figure 5.3a, Figure 5.4**). HEPES injected with H₂AuCl₄ immediately produced a strong EPR signal similar to radicals formed from the reaction of HEPES or EPPS in other conditions.¹⁰² We monitored the change in radical concentration through a continuous-wave EPR every 20 s (Experimental Methods). The radical intensity increased sharply in the first 10 min and decreased for the rest of the reaction (**Figure 5.3b, Figure 5.5, Figure 5.6**). Through UV-Vis spectroscopy, we also measured the change in localized surface plasmon (LSP) resonance, which depends on the particle size, aspect ratio,⁵⁸ and branch length.⁹⁷ The change in optical properties over the reaction time (one LSP peak λ_1 , **Figure 5.7**) showed a similar trend to the radical intensity; λ_1 formed and had a sharp increase in the first 11 – 13 min of the reaction and then stabilized at 780 nm. The initial increase in radical concentration at time t_1 and shift in λ_1 is consistent with reduction of Au(III). To develop a better understanding of particle characteristics, we quenched the growth reaction with a thiolated, low-molecular-weight polyethylene glycol and visualized intermediate particles using TEM (**Figure 5.3c, Figure 5.8, Figure 5.9**). At 3 min, the nanoparticles had no branches and were 3 – 5 nm in diameter. At longer reaction times, the average particle volume, branch number, and branch length increased (**Figure 5.10**). At 12 min, after λ_1 and radical concentration reached a maximum, the reaction completed and the particle morphology stopped evolving.

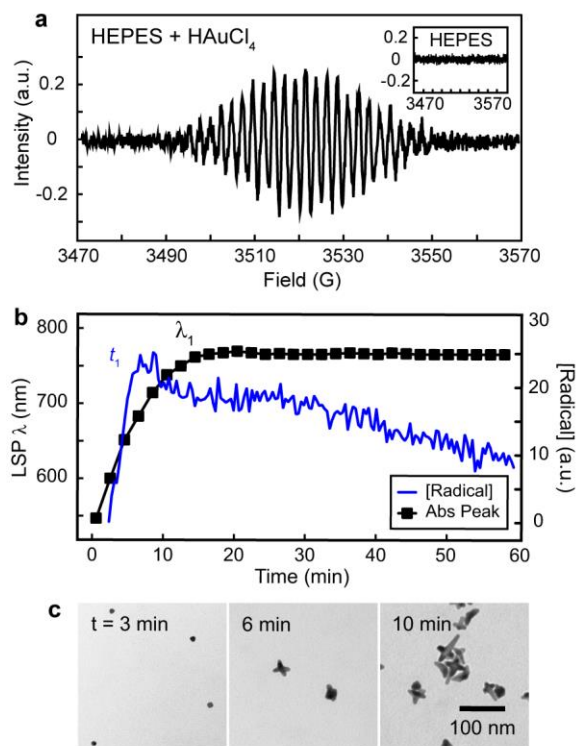


Figure 5.3: Characterization of intermediate species of HEPES + HAuCl₄. (a) Initial EPR signal of 100 mM HEPES before (inset) and after the addition of HAuCl₄. (b) Integrated radical concentration and LSP (λ_1) of the absorbance spectra over the reaction time. t_1 indicates the time of the initial increase in radical concentration. (c) TEM images of the quenched growth reaction at 3, 6, and 10 min.

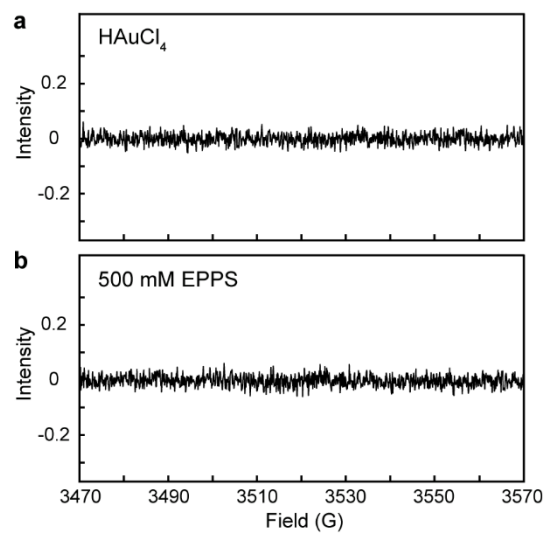


Figure 5.4: EPR spectra of pure HAuCl₄ and EPPS. No radical signal was produced for pure (a) HAuCl₄ or (b) EPPS.

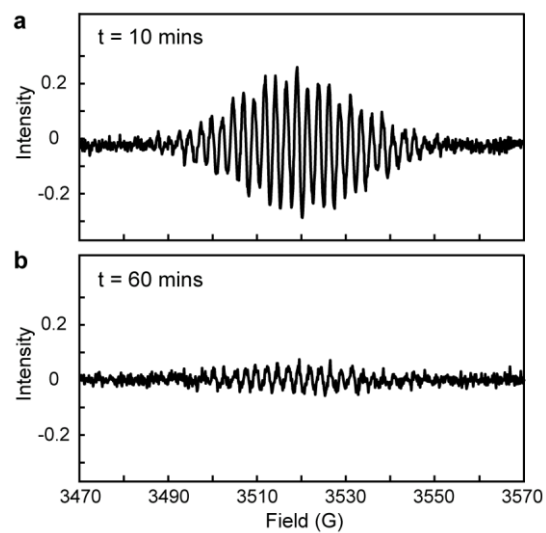


Figure 5.5: EPR spectra of H[AuCl₄] + HEPES. (a) The radical signal peaked at 10 minutes and decayed over the rest of the reaction. **(b)** At 60 minutes, the signal was weak.

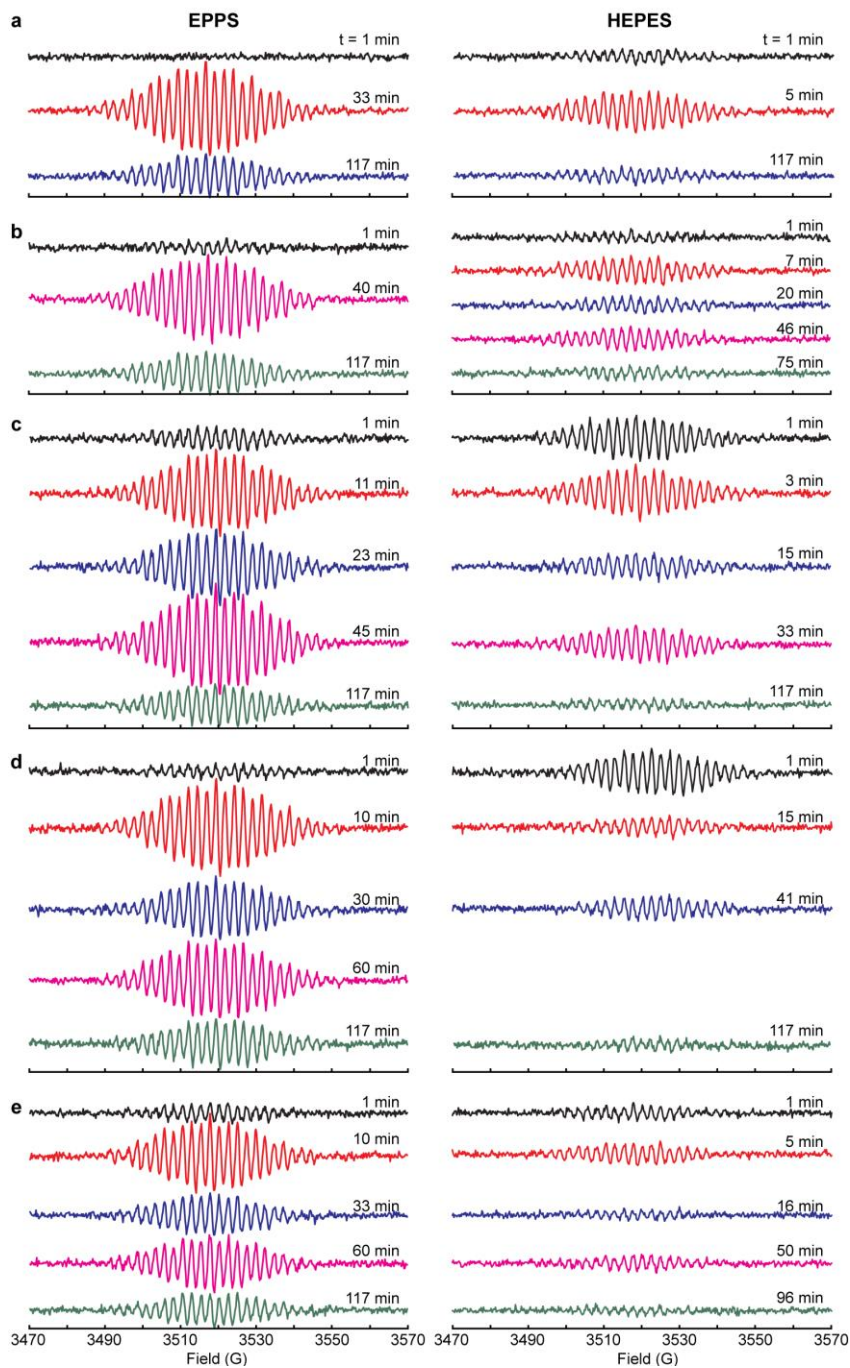


Figure 5.6: Raw HEPES and EPPS EPR spectra. Raw spectra for (a) 100, (b) 250, (c) 500, (d) 750, and (e) 1000 mM EPPS and HEPES concentrations at varying time points.

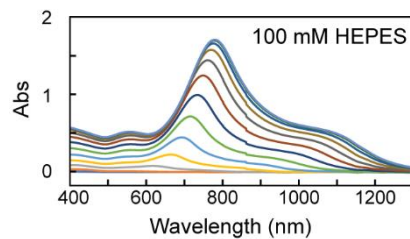


Figure 5.7: Reaction Rate Spectra for HEPES. Absorbance spectra of HEPES AuNS during the course of the synthesis at 100 mM. Spectra were taken every 1 min until the reaction was completed. 100 mM HEPES AuNS solutions had one LSP peak (λ_1).

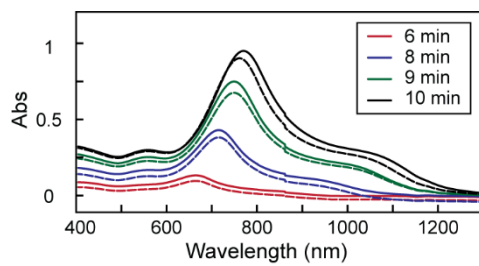


Figure 5.8: Quenched spectra compared to reaction rate spectra. The LSP peak of the real-time reaction rate spectra (solid) compare well with the quenched solutions (dashed).

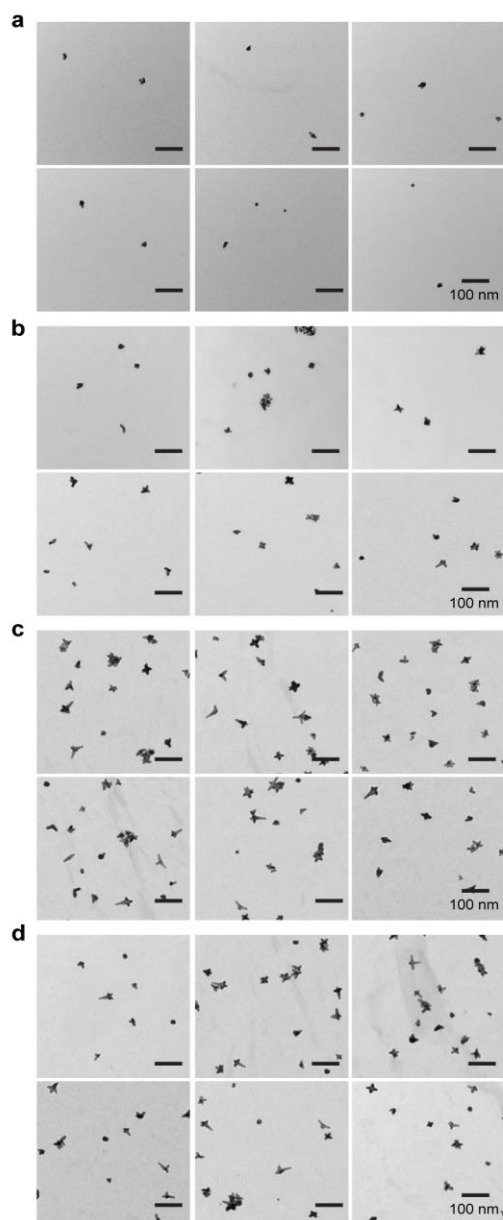


Figure 5.9: Low magnification images of quenched HEPES AuNS. Zoomed-out TEM images of 100 mM HEPES AuNS in the growth solution quenched at **(a)** 3, **(b)** 5, **(c)** 10, and **(d)** 60 minutes. These images demonstrate the change in particle shape over the reaction. After ca. 10 minutes, the reaction completed and the particles did not grow further in solution.

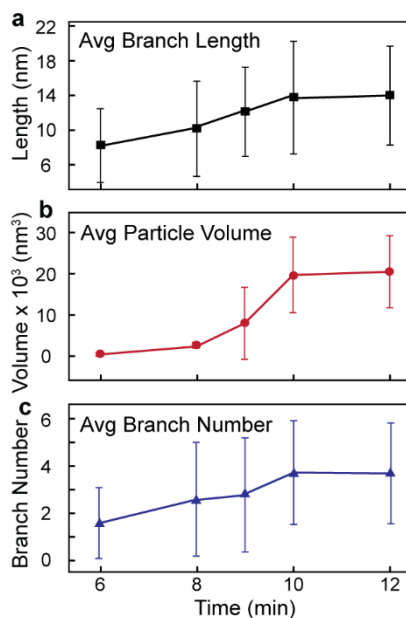


Figure 5.10: Average branch length, particle volume, and branch length of HEPES AuNS.

100 mM HEPES + H₂AuCl₄ was quenched at 6, 8, 9, 10, and 12 minutes with PEG. Using ImageJ, particle morphology was analyzed at each time point based on ≥ 300 particles. **(a)** The average branch length increased to ca. 14 nm during the first 10 minutes of the reaction. The branch length did not increase significantly after that time. The large error bars are due to the heterogeneity of branch number for HEPES AuNS. **(b)** The average particle volume remained low below 8 minutes, due to the formation of small particles. After 8 minutes, the particle grew in average particle volume which corresponded to the large growth in branch length and branch number. **(c)** From 6 to 10 minutes during the reaction, the branch number increased from ca. 2 to ca. 4 branches.

5.2.3 *Second Radical Concentration Increase Indicated Higher Aspect Ratio AuNS*

The branch length of 100-mM HEPES AuNS never exceeded 30 nm, unlike 500-mM EPPS that produced 50% larger particle sizes (80 nm) and up to five times the branch length (≥ 30 nm).¹⁰⁰ Because of these higher aspect ratios, EPPS AuNS produced an optical spectrum with 2 LSP peaks: λ_1 at 800 nm and λ_2 at 1200 nm (**Figure 5.11a**, Figure 5.2). EPPS was injected with HAuCl₄ and exhibited two increases in radical generation. Similar to HEPES, the radical concentration increased immediately after HAuCl₄ injection at a starting time t_1 . The first radical increase correlated to the formation and shift of the λ_1 peak; this indicated particle formation and the initial reduction of Au. At t_1 , the particles were similar to 2 – 5 nm seeds but contained protrusions (**Figure 5.11b**, **Figure 5.12**, **Figure 5.13**). From 5 to 30 min, the branch number increased from approximately 1 to 3 branches per particle, and the branch length remained constant between 7 – 10 nm. The radical signal decreased slightly at 20 min, but unlike HEPES, had a slow second increase in intensity at t_2 . At t_2 , the branch length increased two-fold, but the branch number remained constant (**Figure 5.11c**). Additionally, the formation of a λ_2 peak occurred at t_2 , which indicated branch lengths > 30 nm. Thus, we conclude that the particles and branches formed in the first 30 min and, starting at t_2 , the branches increased more in length.

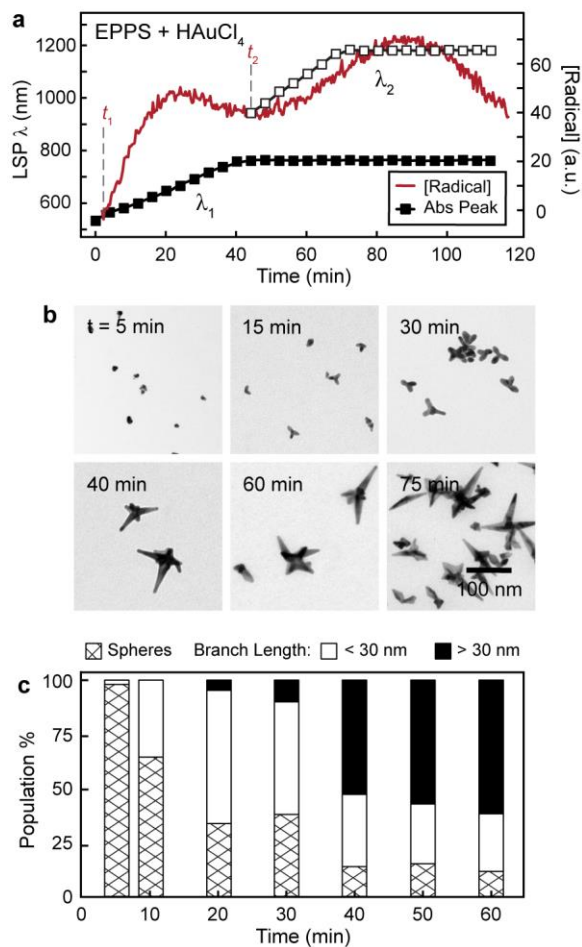


Figure 5.11: Two increases in radical generation for EPPS AuNS. (a) 2 LSP peaks (λ_1 - filled and λ_2 - open) and radical concentration over the reaction. Two increases in radical intensity occur at t_1 and t_2 . (b) TEM images of the quenched growth at 5, 15, 30, 40, 60, and 75 min. (c) The percentage of particles with no branches (spheres), short branches (< 30 nm), or long branches (≥ 30 nm) at different time points during the reaction.

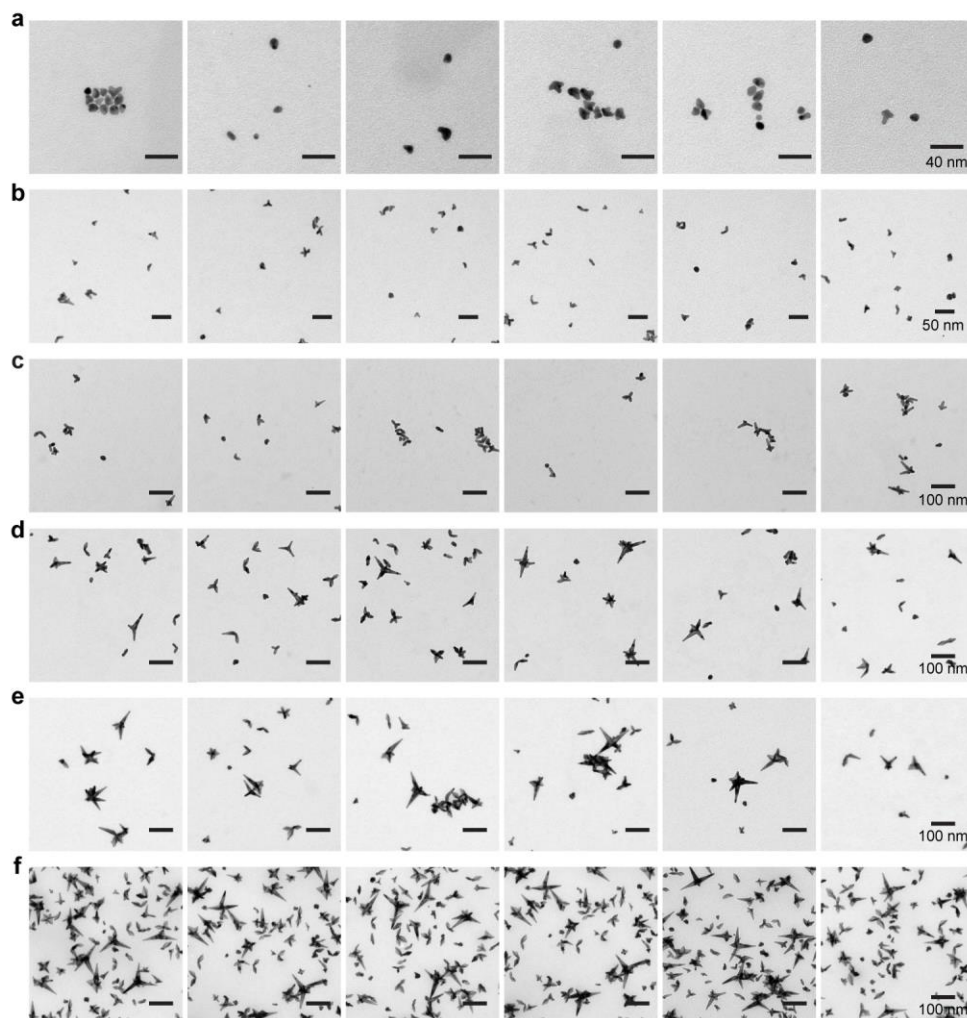


Figure 5.12: Low magnification images of quenched EPPS AuNS. Zoomed-out TEM images of 500 mM HEPES AuNS in the growth solution quenched at (a) 5, (b) 15, (c) 30, (d) 40, (e) 60, and (f) 75 minutes. The scale bars for (a) and (b) are 40 and 50 nm, respectively, due to the small size of the particles. All remaining scale bars are 100 nm. These images demonstrate the change in particle shape over the EPPS AuNS reaction. A significant increase in branch length occurs between (c) 30 and (d) 45 minutes.

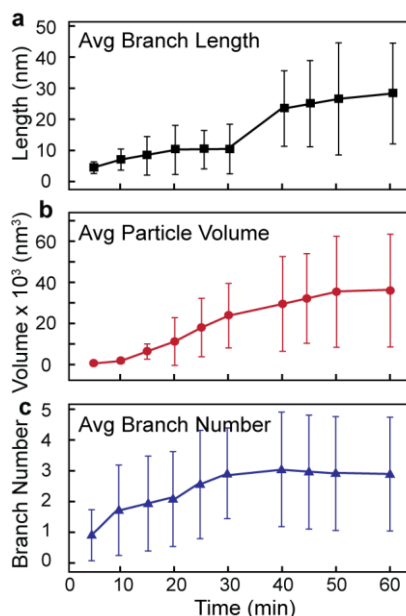


Figure 5.13: Average branch length, particle volume, and branch length of EPPS AuNS.

500 mM EPPS + H₂AuCl₄ was quenched at 5, 10, 15, 20, 25, 30, 40, 45, 50, and 60 minutes with PEG. Using ImageJ, particle morphology was analyzed at each time point based on ≥ 300 particles. **(a)** The average branch length increased to ca. 12 nm during the first 30 minutes of the reaction. The branch length increased significantly to ca. 30 nm between 30 and 40 minutes. The error bars increased between 30 and 40 minutes, because not every particle branch length increased, which created a greater distribution of branch length. **(b)** The average particle volume grew steadily up to 50 minutes. Initially, during the first 30 minutes, the particle volume was due to an increase in branch number. After 30 minutes, the increase in particle volume was due to an increase in branch length. **(c)** During the reaction, from 5 to 30 minutes, the branch number increased from ca. 1 to ca. 3 branches, and remained around 3 – 4 for the remainder of the reaction. The standard deviation of branch number was due to particle heterogeneity.

5.2.4 Radical Generation Depended on Buffer Concentration

Besides buffer type, buffer concentration also affected particle morphology. **Figure 5.14** shows HEPES and EPPS radical production and intermediate particle shape during the reaction at varying concentrations (Figure S4). The integrated intensity represents radical concentration in solution and allows comparison of between samples. Note: the two radical intensity plots from Figures 1 – 2 are redisplayed in Figure 3 to compare buffer concentration trends. HEPES concentration ≤ 500 mM produced AuNS and generated radicals; however, the intensity and trend changed with buffer concentration (**Figure 5.14a-b, Figure 5.15**). For all concentrations, an increase in radical concentration of varying intensities occurred at t_1 , which corresponded to the initial formation of the particles. For 100-mM HEPES, the particles were fully formed at 12 min. At 500-mM HEPES, a second radical increase occurred but at a low intensity that correlated with the late formation and shift of λ_2 (**Figure 5.16**). The branch length for HEPES was *ca.* 15 nm but still a third of the length of 500-mM EPPS AuNS. Above this concentration, HEPES could not produce AuNS (Figure S1) and a very low intensity of radicals was generated, which indicated little Au (III) reduction.

EPPS produced stable AuNS and generated radicals up to 1000 mM (**Figure 5.14c-d, Figure 5.2**). For all concentrations, a high-intensity radical concentration increase occurred at t_1 along with the formation and shift of λ_1 . Above 100 mM, a second increase occurred at different times and intensities and was associated with longer branch lengths (> 30 nm). The time of the second increase, t_2 , correlated with the formation and shift of λ_2 for higher EPPS concentrations (Figure 5.15). We observed that branch length and overall particle size were influenced by the intensity and duration of the second radical increase. We hypothesize that the multi-step AuNS reaction

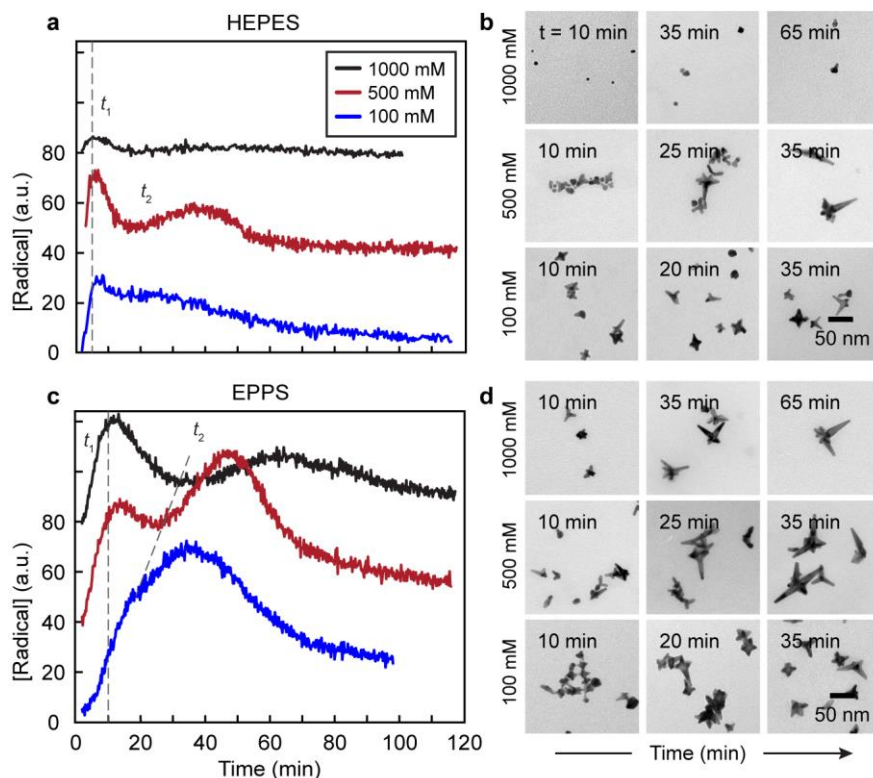


Figure 5.14: Radical generation depends on buffer concentration and type. (a) HEPES and (c) EPPS radical intensity at 3 different [buffer]. Each line scan is offset by 40 (a.u.). A dashed line was placed at 20 min to distinguish the relative radical increases at t_1 and t_2 . Thinner dashed lines demonstrate the temporal shift for t_2 of different [EPPS]. Corresponding TEM images of AuNS quenched at different time points during the reaction (in the upper LH corner of each image) for (b) HEPES and (d) EPPS.

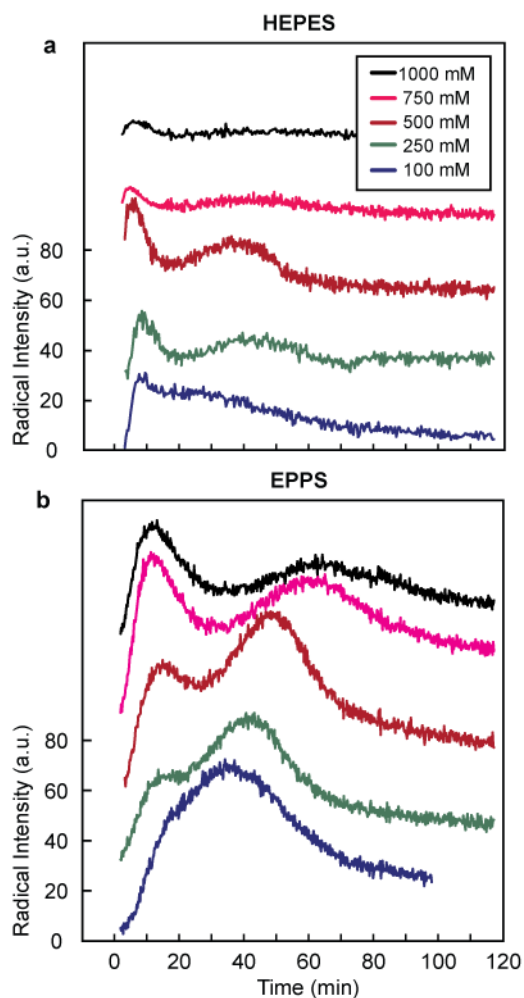


Figure 5.15: Radical generation depends on buffer concentration and type. (a) HEPES and (b) EPPS line scans at 5 different [buffer] (100, 250, 500, 750, and 1000 mM). Green and pink radical scans represent additional concentrations to demonstrate the trend continuity. Each line scan is offset by 30 (a.u.). HEPES AuNS only produced a significant second rise at 250 and 500 mM. EPPS AuNS produced a second rise of varying intensities at varying times.

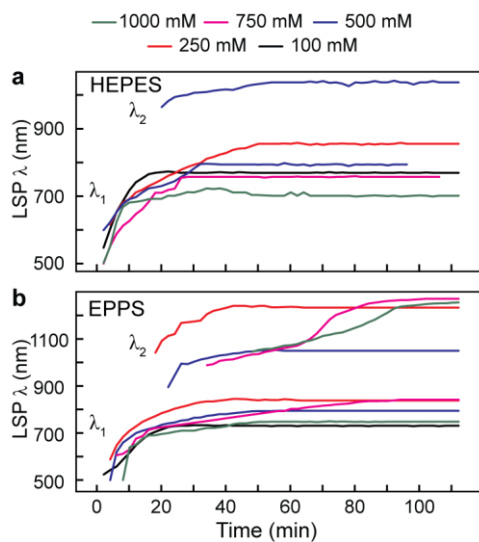


Figure 5.16: LSP peak shift during the AuNS reaction. (a) HEPES AuNS formed 1 LSP peak for all concentrations except for 500 mM which formed 2 LSP peaks. For concentrations > 500 mM, the absorbance spectra did not have any defined peaks (Fig. S1). **(b)** EPPS AuNS > 100 mM had absorbance spectra with 2 LSP peaks.

may be rate-limited by exposure of the more reactive crystalline planes on the nanoparticle surface. EPPS samples produced a stronger radical signal than HEPES at both t_1 and t_2 at any concentration. Since the only difference between HEPES and EPPS is an additional carbon in the alkane sulfonate group, the isolation of the piperazine ring, which allows for a more electron-rich environment, may cause an increase in the reducing ability for EPPS.

5.2.5 Visualizing AuNS Growth through In Situ TEM

We visualized the morphological evolution of AuNS through an *ex situ* protocol, i.e. the quenching of the synthesis at different times. Liquid-TEM has been developed over the last decade as an *in situ* alternative tool.¹⁸⁵ This technique allows direct visualization of the crystals in solution as they grow. To visualize the particle growth (100 mM HEPES + HAuCl₄) in real-time, we used *in situ* and liquid TEM. We completed two experimental methods: (1) *in situ* TEM – flowing the precursor solution through a SiN transparent chip and (2) liquid TEM – depositing the growth solution in a graphene grid at varying time points in the reaction.

The SiN chip had a 50 μm \times 200 μm transparent window that the e^- beam can transmitted through. The spacing between the top and bottom chip was 250 nm, which allowed for a volume of < 1 μL in the viewing area. Initially, we loaded the SiN window with water and *ex situ* mixed 100 mM HEPES with HAuCl₄. We slowly flowed the growth solution through the SiN chip using a turbo pump. Initially, under a high accelerating voltage, the beam interacted with the buffer salt in solution and created 500-nm artifacts which impeded particle visualization (**Figure 5.17a**). After lowering the accelerating voltage, we still could not visualize particles due to the flow of the growth solution.

Next, we tried direct deposition of the growth solution onto the SiN chip without any flow of the precursors. We *ex situ* mixed the precursors and transferred the growth solution into the SiN window at varying time points. After the chip was loaded in the TEM, we began imaging within 5 minutes. We captured particles at different time points depending on the deposition time (**Figure 5.17b**). In the initial 10 minutes, small particles at the beginning stages of growth formed, similar to seeds formed. After 10 minutes, the particle branches formed and did not significantly grow with time. These results matched well with our *ex situ* quenching experiments (Figure 5.9). Two major issues arose from imaging AuNS *in situ*. First, capturing the AuNS growth in one continuous video was difficult due to the minute time-scale growth. Secondly, the limited viewing area coupled with the dynamic motion of the AuNS caused continuous viewing of the same particle challenging (**Figure 5.17c**).

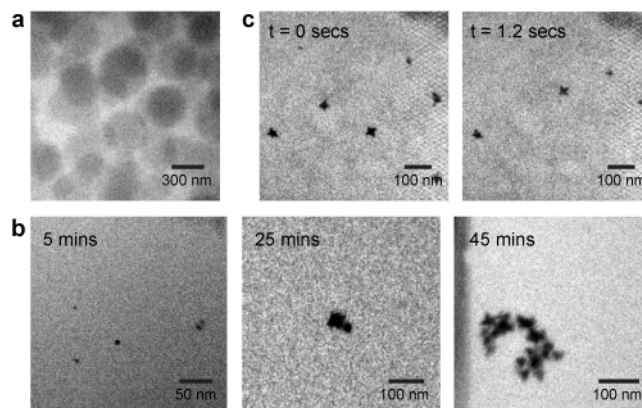


Figure 5.17: Morphological evolution of HEPES AuNS through *in situ* TEM using a SiN cell. (a) HEPES interacting with a high-kV caused large artifacts in the cell, which preventing imaging of the AuNS. **(b)** After direct deposition of the growth solution, images of AuNS at 5, 25, and 45 minutes were taken. **(c)** Two snaps of a movie collected of the growth solution *in situ*, spaced 1.2 seconds apart. The movement of the particles in solution was too rapidly to allow for imaging of one particle over an extended time period.

To resolve high resolution images of the growing particles, we used a liquid graphene cell as described in Alvisatos et. al.¹⁸⁶ Briefly, the AuNS growth solution is sandwiched between two laminated graphene layers suspend over holes in a conventional mesh, copper TEM grid. Due to van der Waals interactions between the graphene sheet, the solution is encapsulated in the center. Liquid droplets from 6 – 200 nm can be securely trapped between the double-membrane liquid pocket. Due to the small thickness of graphene and the copper grid, high resolution of the particles in liquid is possible. After mixing the precursors, we immediately placed the growth solution on the graphene cell. We found that 2 – 5 nm particles formed within 5 minutes (**Figure 5.18a**). These contained slight protrusions but the majority were spherical (circularity > 0.8). High resolution imaging revealed that the initial particles had twin boundaries form in the <111> direction (**Figure 5.18b**). The twin boundaries on the initial particle allowed for growth of the branches in the <111> direction. As previously published, the branches of HEPES AuNS grow in the <111> direction.⁹⁶
¹⁰⁰ Thus, the seeds we visualized through liquid TEM show the initial particles determined the branch growth direction.

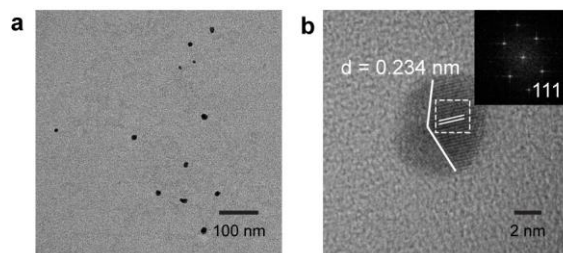


Figure 5.18: Crystallographic structure of initial HEPES particles. (a) Initial particle formation during the first 5 minutes of the reaction. (b) HR-TEM images were taken of initial particles during the AuNS growth reaction in a liquid graphene cell. The lattice spacing (d) was determined through FFT analysis. The FFT (inset) was taken from the area outlined with a dotted white box. The initial particles had twinned boundaries (solid white line) between the $\langle 111 \rangle$ direction.

5.3 Summary

In summary, we showed how EPR signals of intermediates during a nanoparticle reaction can be combined with optical and structural properties of particles at specific time points to provide insight into the mechanism of seedless nanoparticle growth. This correlative approach can be used as a multi-faceted method to determine intermediate species during synthesis and reveal new information about radical-based nanoparticle formation.

5.4 Experimental methods

5.4.1 *Nanostar synthesis and characterization*

The Good's buffers used were 4-(2-hydroxyethyl)piperazine-1-ethanesulfonic acid (HEPES buffer, Sigma Aldrich) and 4-(2-hydroxyethyl)-1piperazinepropanesulfonic acid (EPPS buffer, Sigma Aldrich). The 1-M stock HEPES and EPPS solution was made by dissolving the buffer salt in Millipore water (18.2 M Ω ·cm) using a medium-sized stir bar to ensure thorough mixing. The pH of the buffer solution was measured using a Thermo Scientific pH meter and was adjusted using concentrated solutions of NaOH. For fine pH adjustments, HCl was added dropwise.

AuNS were synthesized by adding 0.2 mM (final concentration) Au (III) chloride trihydrate (HAuCl₄, Sigma Aldrich) to 100 - 1000 mM of each buffer. Each solution was vortexed in a 50-mL Falcon tube for one minute before addition of HAuCl₄ and for 30 seconds afterwards. After vortexing, the growth solution was measured through UV-Vis.

5.4.2 *Particle Characterization Technique*

3 mL of AuNS solution was placed in a 1-cm plastic Brookhaven cuvette and the absorbance spectra was measured from 400 nm to 1400 nm using a Cary 5000 UV-vis-NIR spectrophotometer

(Agilent Technologies). The spectra were measured every minute for 60 minutes or until the reaction had completed.

For TEM grid preparation, carbon Type B, 300 mesh copper grids (Ted Pella) were treated with 0.1% (w/v) poly-L-lysine (Sigma Aldrich) for 5 minutes. Then, 40 μ L of 10 \times concentrated Au nanoparticle solution was left to rest on the treated grids for 30 – 60 seconds and then wicked away with filter paper. A JEOL 1230 TEM was used for imaging the particles. Representative images were collected from different areas of the grid. Structural features, such as circularity and Feret diameter, were characterized using the Analyze Particles plugin on ImageJ for at least 500 particles per sample. A circularity threshold of 0.9 was used to define spherical particles and the Feret diameter corresponds to the largest tip-to-tip distance on a particle. Branch length for ≥ 300 particles was measured manually from the tip to the base of the branch.

5.4.3 Growth Solution Quenching

The growth solutions were prepared by adding 0.2 mM (final concentration) Au (III) chloride trihydrate (HAuCl_4 , Sigma Aldrich) to 20 mL of each buffer concentration, which indicated the 0-minute time point. Each solution was measured in real-time through UV-Vis spectroscopy every minute until 100 minutes.

Throughout the reaction, 1-mL aliquots were pipetted at varying time points to 2-mL Eppendorf tubes of 20 μ L of 40 mM thiolated, 0.5 kDa polyethylene glycol (Sigma Aldrich). Each PEG + growth solution aliquot was vortexed for 30 seconds and then centrifuged for 10,000 RPM for 10 – 15 minutes. The supernatant was removed and the pellet was re-dispersed in the corresponding concentration of the buffer, either HEPES or EPPS. The absorbance spectra were

taken of the re-dispersed quenched solution and matched with the real-time absorbance spectra to ensure that the growth solution had been quenched.

5.4.4 Electron Paramagnetic Resonance Spectroscopy

Continuous wave electron paramagnetic resonance (EPR) spectra were obtained at X-band (9.5 GHz) fields using a Bruker Eleksys E680 spectrometer equipped with a 4122SHQE resonator. Scans were performed with magnetic field modulation amplitude of 1 G and non-saturating microwave power between 0.4 and 0.6 mW. Samples were contained in quartz tubes with I.D. 1.50 mm and O.D. 1.80 mm. Scans of approximately 20 s in length were performed continually to monitor the concentration of the radical. To compensate for the relatively weak signal, the absolute values of the resulting spectra were integrated across the field range.

REFERENCES

1. Chaudhary, A., Ayurvedic Bhasma: Nanomedicine of Ancient India-Its Global Contemporary Perspective. *Journal of Biomedical Nanotechnology* **2011**, 7 (1), 68-69.
2. Higby, G. J., Gold in medicine: a review of its use in the West before 1900. *Gold Bulletin* **1982**, 15 (4), 130-140.
3. Huber, A., The chemical nature of purple of Cassius. *Physikalische Zeitschrift* **1924**, 25 45-47.
4. Freestone, I.; Meeks, N.; Sax, M.; Higgitt, C., The Lycurgus Cup - A Roman nanotechnology. *Gold Bulletin* **2007**, 40 (4), 270-277.
5. Daniel, M. C.; Astruc, D., Gold nanoparticles: Assembly, supramolecular chemistry, quantum-size-related properties, and applications toward biology, catalysis, and nanotechnology. *Chemical Reviews* **2004**, 104 (1), 293-346.
6. Faraday, M., The Bakerian Lecture – Experimental relations of gold (and other metals) to light. *Philosophical Transactions* **1857**, 147 145-181.
7. Williams, L. P., Michael Faraday and the physics of 100 years ago. *Science* **1967**, 156 (3780), 1335-1342.
8. Cosslett, V. E., Fundamentals of Transmission Electron Microscopy. *Nature* **1965**, 206 (4979), 52-130.
9. Kelly, K. L.; Coronado, E.; Zhao, L. L.; Schatz, G. C., The optical properties of metal nanoparticles: The influence of size, shape, and dielectric environment. *Journal of Physical Chemistry B* **2003**, 107 (3), 668-677.
10. El-Sayed, M. A., Some interesting properties of metals confined in time and nanometer space of different shapes. *Accounts of Chemical Research* **2001**, 34 (4), 257-264.
11. Valden, M.; Lai, X.; Goodman, D. W., Onset of catalytic activity of gold clusters on titania with the appearance of nonmetallic properties. *Science* **1998**, 281 (5383), 1647-1650.
12. Chen, M. S.; Goodman, D. W., The structure of catalytically active gold on titania. *Science* **2004**, 306 (5694), 252-255.
13. Johnston, H. J.; Hutchison, G.; Christensen, F. M.; Peters, S.; Hankin, S.; Stone, V., A review of the *in vivo* and *in vitro* toxicity of silver and gold particulates: Particle attributes and biological mechanisms responsible for the observed toxicity. *Critical Reviews in Toxicology* **2010**, 40 (4), 328-346.

14. Dam, D. H. M.; Lee, J. H.; Sisco, P. N.; Co, D. T.; Zhang, M.; Wasielewski, M. R.; Odom, T. W., Direct Observation of Nanoparticle-Cancer Cell Nucleus Interactions. *ACS Nano* **2012**, *6* (4), 3318-3326.
15. Chance, B., Near-infrared images using continuous, phase-modulated, and pulsed light with quantitation of blood and blood oxygenation. *Advances in Optical Biopsy and Optical Mammography* **1998**, *838* 29-45.
16. Durr, N. J.; Larson, T.; Smith, D. K.; Korgel, B. A.; Sokolov, K.; Ben-Yakar, A., Two-photon luminescence imaging of cancer cells using molecularly targeted gold nanorods. *Nano Letters* **2007**, *7* (4), 941-945.
17. Su, K. H.; Wei, Q. H.; Zhang, X.; Mock, J. J.; Smith, D. R.; Schultz, S., Interparticle coupling effects on plasmon resonances of nanogold particles. *Nano Letters* **2003**, *3* (8), 1087-1090.
18. Skrabalak, S. E.; Chen, J. Y.; Sun, Y. G.; Lu, X. M.; Au, L.; Cobley, C. M.; Xia, Y. N., Gold Nanocages: Synthesis, Properties, and Applications. *Accounts of Chemical Research* **2008**, *41* (12), 1587-1595.
19. Jain, P. K.; Huang, X. H.; El-Sayed, I. H.; El-Sayed, M. A., Noble Metals on the Nanoscale: Optical and Photothermal Properties and Some Applications in Imaging, Sensing, Biology, and Medicine. *Accounts of Chemical Research* **2008**, *41* (12), 1578-1586.
20. Schultz, D. A., Plasmon resonant particles for biological detection. *Current Opinion in Biotechnology* **2003**, *14* (1), 13-22.
21. Elghanian, R.; Storhoff, J. J.; Mucic, R. C.; Letsinger, R. L.; Mirkin, C. A., Selective colorimetric detection of polynucleotides based on the distance-dependent optical properties of gold nanoparticles. *Science* **1997**, *277* (5329), 1078-1081.
22. Cognet, L.; Tardin, C.; Boyer, D.; Choquet, D.; Tamarat, P.; Lounis, B., Single metallic nanoparticle imaging for protein detection in cells. *Proceedings of the National Academy of Sciences* **2003**, *100* (20), 11350-11355.
23. Taton, T. A.; Mirkin, C. A.; Letsinger, R. L., Scanometric DNA array detection with nanoparticle probes. *Science* **2000**, *289* (5485), 1757-1760.
24. Xu, X. H. N.; Brownlow, W. J.; Kyriacou, S. V.; Wan, Q.; Viola, J. J., Real-time probing of membrane transport in living microbial cells using single nanoparticle optics and living cell imaging. *Biochemistry* **2004**, *43* (32), 10400-10413.
25. Stone, J. W.; Sisco, P. N.; Goldsmith, E. C.; Baxter, S. C.; Murphy, C. J., Using gold nanorods to probe cell-induced collagen deformation. *Nano Letters* **2007**, *7* (1), 116-119.

26. Garrell, R. L., Surface-Enhanced Raman-Spectroscopy. *Analytical Chemistry* **1989**, *61* (6), 401-411.
27. Campion, A.; Kambhampati, P., Surface-enhanced Raman scattering. *Chemical Society Reviews* **1998**, *27* (4), 241-250.
28. Kneipp, K.; Kneipp, H.; Itzkan, I.; Dasari, R. R.; Feld, M. S., Ultrasensitive chemical analysis by Raman spectroscopy. *Chemical Reviews* **1999**, *99* (10), 2957-2976.
29. Jiang, J.; Bosnick, K.; Maillard, M.; Brus, L., Single molecule Raman spectroscopy at the junctions of large Ag nanocrystals. *Journal of Physical Chemistry B* **2003**, *107* (37), 9964-9972.
30. Nie, S. M.; Emery, S. R., Probing single molecules and single nanoparticles by surface-enhanced Raman scattering. *Science* **1997**, *275* (5303), 1102-1106.
31. Sokolov, K.; Chumanov, G.; Cotton, T. M., Enhancement of molecular fluorescence near the surface of colloidal metal films. *Analytical Chemistry* **1998**, *70* (18), 3898-3905.
32. Malicka, J.; Gryczynski, I.; Gryczynski, Z.; Lakowicz, J. R., DNA hybridization using surface plasmon-coupled emission. *Biomedical Vibrational Spectroscopy and Biohazard Detection Technologies* **2004**, *5321* 283-288.
33. Parfenov, A.; Gryczynski, I.; Malicka, J.; Geddes, C. D.; Lakowicz, J. R., Enhanced fluorescence from fluorophores on fractal silver surfaces. *Journal of Physical Chemistry B* **2003**, *107* (34), 8829-8833.
34. Wang, Y.; Zhang, S.; Du, D.; Shao, Y. Y.; Li, Z. H.; Wang, J.; Engelhard, M. H.; Li, J. H.; Lin, Y. H., Self assembly of acetylcholinesterase on a gold nanoparticles-graphene nanosheet hybrid for organophosphate pesticide detection using polyelectrolyte as a linker. *Journal of Materials Chemistry* **2011**, *21* (14), 5319-5325.
35. Zhang, L., Self-assembly Ag nanoparticle monolayer film as SERS Substrate for pesticide detection. *Applied Surface Science* **2013**, *270* 292-294.
36. Maxwell, D. J.; Taylor, J. R.; Nie, S. M., Self-assembled nanoparticle probes for recognition and detection of biomolecules. *Journal of the American Chemical Society* **2002**, *124* (32), 9606-9612.
37. Polsky, R.; Gill, R.; Kaganovsky, L.; Willner, I., Nucleic acid-functionalized Pt nanoparticles: Catalytic labels for the amplified electrochemical detection of biomolecules. *Analytical Chemistry* **2006**, *78* (7), 2268-2271.
38. Niikura, K.; Nagakawa, K.; Ohtake, N.; Suzuki, T.; Matsuo, Y.; Sawa, H.; Ijio, K., Gold Nanoparticle Arrangement on Viral Particles through Carbohydrate Recognition: A Non-

- Cross-Linking Approach to Optical Virus Detection. *Bioconjugate Chemistry* **2009**, *20* (10), 1848-1852.
39. Chou, T. C.; Hsu, W.; Wang, C. H.; Chen, Y. J.; Fang, J. M., Rapid and specific influenza virus detection by functionalized magnetic nanoparticles and mass spectrometry. *Journal of Nanobiotechnology* **2011**, *9* 9-52.
 40. Jv, Y.; Li, B. X.; Cao, R., Positively-charged gold nanoparticles as peroxidase mimic and their application in hydrogen peroxide and glucose detection. *Chemical Communications* **2010**, *46* (42), 8017-8019.
 41. Lu, W. B.; Luo, Y. L.; Chang, G. H.; Sun, X. P., Synthesis of functional SiO₂-coated graphene oxide nanosheets decorated with Ag nanoparticles for H₂O₂ and glucose detection. *Biosensors & Bioelectronics* **2011**, *26* (12), 4791-4797.
 42. Cui, H. F.; Ye, J. S.; Zhang, W. D.; Li, C. M.; Luong, J. H. T.; Sheu, F. S., Selective and sensitive electrochemical detection of glucose in neutral solution using platinum-lead alloy nanoparticle/carbon nanotube nanocomposites. *Analytica Chimica Acta* **2007**, *594* (2), 175-183.
 43. Park, S. J.; Taton, T. A.; Mirkin, C. A., Array-based electrical detection of DNA with nanoparticle probes. *Science* **2002**, *295* (5559), 1503-1506.
 44. Cao, Y. W. C.; Jin, R. C.; Mirkin, C. A., Nanoparticles with Raman spectroscopic fingerprints for DNA and RNA detection. *Science* **2002**, *297* (5586), 1536-1540.
 45. Su, M.; Li, S. U.; Dravid, V. P., Microcantilever resonance-based DNA detection with nanoparticle probes. *Applied Physics Letters* **2003**, *82* (20), 3562-3564.
 46. Hua, Y.; Chandra, K.; Dam, D. H. M.; Wiederrecht, G. P.; Odom, T. W., Shape-Dependent Nonlinear Optical Properties of Anisotropic Gold Nanoparticles. *Journal of Physical Chemistry Letters* **2015**, *6* (24), 4904-4908.
 47. Philip, R.; Kumar, G. R.; Sandhyarani, N.; Pradeep, T., Picosecond optical nonlinearity in monolayer-protected gold, silver, and gold-silver alloy nanoclusters. *Physical Review B* **2000**, *62* (19), 13160-13166.
 48. Xia, Y. N.; Xiong, Y. J.; Lim, B.; Skrabalak, S. E., Shape-Controlled Synthesis of Metal Nanocrystals: Simple Chemistry Meets Complex Physics? *Angewandte Chemie-International Edition* **2009**, *48* (1), 60-103.
 49. Elechiguerra, J. L.; Reyes-Gasga, J.; Yacaman, M. J., The role of twinning in shape evolution of anisotropic noble metal nanostructures. *Journal of Materials Chemistry* **2006**, *16* (40), 3906-3919.

50. Niu, W. X.; Xu, G. B., Crystallographic control of noble metal nanocrystals. *Nano Today* **2011**, *6* (3), 265-285.
51. Wang, Z. L., Transmission electron microscopy of shape-controlled nanocrystals and their assemblies. *Journal of Physical Chemistry B* **2000**, *104* (6), 1153-1175.
52. Jones, M. R.; Osberg, K. D.; Macfarlane, R. J.; Langille, M. R.; Mirkin, C. A., Templated Techniques for the Synthesis and Assembly of Plasmonic Nanostructures. *Chemical Reviews* **2011**, *111* (6), 3736-3827.
53. Tao, A. R.; Habas, S.; Yang, P. D., Shape control of colloidal metal nanocrystals. *Small* **2008**, *4* (3), 310-325.
54. Mody, V. V.; Siwale, R.; Singh, A.; Mody, H. R., Introduction to metallic nanoparticles. *Journal of Pharmacy and Bioallied Sciences* **2010**, *2* (4), 282-289.
55. Burda, C.; Chen, X. B.; Narayanan, R.; El-Sayed, M. A., Chemistry and properties of nanocrystals of different shapes. *Chemical Reviews* **2005**, *105* (4), 1025-1102.
56. Murphy, C. J.; San, T. K.; Gole, A. M.; Orendorff, C. J.; Gao, J. X.; Gou, L.; Hunyadi, S. E.; Li, T., Anisotropic metal nanoparticles: Synthesis, assembly, and optical applications. *Journal of Physical Chemistry B* **2005**, *109* (29), 13857-13870.
57. Thomas, K. G.; Barazzouk, S.; Ipe, B. I.; Joseph, S. T. S.; Kamat, P. V., Uniaxial plasmon coupling through longitudinal self-assembly of gold nanorods. *Journal of Physical Chemistry B* **2004**, *108* (35), 13066-13068.
58. Webb, J. A.; Erwin, W. R.; Zarick, H. F.; Aufrecht, J.; Manning, H. W.; Lang, M. J.; Pint, C. L.; Bardhan, R., Geometry-Dependent Plasmonic Tunability and Photothermal Characteristics of Multibranching Gold Nanoantennas. *Journal of Physical Chemistry C* **2014**, *118* (7), 3696-3707.
59. Xie, J. P.; Zhang, Q. B.; Lee, J. Y.; Wang, D. I. C., The Synthesis of SERS-Active Gold Nanoflower Tags for *In Vivo* Applications. *ACS Nano* **2008**, *2* (12), 2473-2480.
60. de Puig, H.; Tam, J. O.; Yen, C. W.; Gehrke, L.; Hamad-Schifferli, K., Extinction Coefficient of Gold Nanostars. *Journal of Physical Chemistry C* **2015**, *119* (30), 17408-17415.
61. Yuan, H. K.; Khoury, C. G.; Hwang, H.; Wilson, C. M.; Grant, G. A.; Vo-Dinh, T., Gold nanostars: surfactant-free synthesis, 3D modelling, and two-photon photoluminescence imaging. *Nanotechnology* **2012**, *23* (7), 075102.
62. Hao, E.; Bailey, R. C.; Schatz, G. C.; Hupp, J. T.; Li, S. Y., Synthesis and optical properties of "branched" gold nanocrystals. *Nano Letters* **2004**, *4* (2), 327-330.

63. Tang, X. L.; Jiang, P.; Ge, G. L.; Tsuji, M.; Xie, S. S.; Guo, Y. J., Poly(N-vinyl-2-pyrrolidone) (PVP)-capped dendritic gold nanoparticles by a one-step hydrothermal route and their high SERS effect. *Langmuir* **2008**, *24* (5), 1763-1768.
64. Jeong, G. H.; Lee, Y. W.; Kim, M.; Han, S. W., High-yield synthesis of multi-branched gold nanoparticles and their surface-enhanced Raman scattering properties. *Journal Colloid Interface Science* **2009**, *329* (1), 97-102.
65. Zou, X. Q.; Ying, E. B.; Dong, S. J., Seed-mediated synthesis of branched gold nanoparticles with the assistance of citrate and their surface-enhanced Raman scattering properties. *Nanotechnology* **2006**, *17* (18), 4758-4764.
66. Yuan, H.; Fales, A. M.; Vo-Dinh, T., TAT Peptide-Functionalized Gold Nanostars: Enhanced Intracellular Delivery and Efficient NIR Photothermal Therapy Using Ultralow Irradiance. *Journal of American Chemical Society* **2012**, *134* (28), 11358-11361.
67. Li, W.; Chen, X., Gold nanoparticles for photoacoustic imaging. *Nanomedicine* **2015**, *10* (2), 299-320.
68. Rotz, M. W.; Culver, K. S. B.; Parigi, G.; MacRenaris, K. W.; Luchinat, C.; Odom, T. W.; Meade, T. J., High Relaxivity Gd(III)-DNA Gold Nanostars: Investigation of Shape Effects on Proton Relaxation. *ACS Nano* **2015**, *9* (3), 3385-3396.
69. Gole, A.; Murphy, C. J., Seed-mediated synthesis of gold nanorods: Role of the size and nature of the seed. *Chemistry of Materials* **2004**, *16* (19), 3633-3640.
70. Turkevich, J.; Stevenson, P. C.; Hillier, J., A Study of the Nucleation and Growth Processes in the Synthesis of Colloidal Gold. *Discussions of the Faraday Society* **1951**, (11), 55-75.
71. Turkevich, J.; Stevenson, P. C.; Hillier, J., The Formation of Colloidal Gold. *Journal of Physical Chemistry* **1953**, *57* (7), 670-673.
72. Frens, G., Controlled Nucleation for Regulation of Particle-Size in Monodisperse Gold Suspensions. *Nature Physical Science* **1973**, *241* (105), 20-22.
73. Brust, M.; Walker, M.; Bethell, D.; Schiffrin, D. J.; Whyman, R., Synthesis of Thiol-Derivatized Gold Nanoparticles in a 2-Phase Liquid-Liquid System. *Journal of the Chemical Society, Chemical Communications* **1994**, (7), 801-802.
74. Grzelczak, M.; Perez-Juste, J.; Mulvaney, P.; Liz-Marzan, L. M., Shape control in gold nanoparticle synthesis. *Chemical Society Reviews* **2008**, *37* (9), 1783-1791.
75. Kumar, S.; Gandhi, K. S.; Kumar, R., Modeling of formation of gold nanoparticles by citrate method. *Industrial & Engineering Chemistry Research* **2007**, *46* (10), 3128-3136.

76. Wang, Y. S.; Aili, D.; Selegard, R.; Tay, Y.; Baltzer, L.; Zhang, H.; Liedberg, B., Specific functionalization of CTAB stabilized anisotropic gold nanoparticles with polypeptides for folding-mediated self-assembly. *Journal of Materials Chemistry* **2012**, *22* (38), 20368-20373.
77. Verma, M. S.; Chen, P. Z.; Jones, L.; Gu, F. X., Branching and size of CTAB-coated gold nanostars control the colorimetric detection of bacteria. *RSC Advances* **2014**, *4* (21), 10660-10668.
78. Jana, N. R.; Gearheart, L.; Murphy, C. J., Seed - Mediated Growth Approach for Shape - Controlled Synthesis of Spheroidal and Rod - like Gold Nanoparticles Using a Surfactant Template. *Advanced Materials* **2001**, *13* (18), 1389-1393.
79. Nikoobakht, B.; El-Sayed, M. A., Preparation and growth mechanism of gold nanorods (NRs) using seed-mediated growth method. *Chemistry of Materials* **2003**, *15* (10), 1957-1962.
80. Liu, M.; Guyot-Sionnest, P., Mechanism of Silver(I)-Assisted Growth of Gold Nanorods and Bipyramids. *Journal of Physical Chemistry B* **2005**, *109* (47), 22192-22200.
81. Johnson, C. J.; Dujardin, E.; Davis, S. A.; Murphy, C. J.; Mann, S., Growth and form of gold nanorods prepared by seed-mediated, surfactant-directed synthesis. *Journal of Materials Chemistry* **2002**, *12* (6), 1765-1770.
82. Busbee, B. D.; Obare, S. O.; Murphy, C. J., An improved synthesis of high-aspect-ratio gold nanorods. *Advanced Materials* **2003**, *15* (5), 414-416.
83. Gou, L. F.; Murphy, C. J., Fine-tuning the shape of gold nanorods. *Chemistry of Materials* **2005**, *17* (14), 3668-3672.
84. Link, S.; Mohamed, M. B.; El-Sayed, M. A., Simulation of the optical absorption spectra of gold nanorods as a function of their aspect ratio and the effect of the medium dielectric constant. *Journal of Physical Chemistry B* **1999**, *103* (16), 3073-3077.
85. Wang, Z. L.; Mohamed, M. B.; Link, S.; El-Sayed, M. A., Crystallographic facets and shapes of gold nanorods of different aspect ratios. *Surface Science* **1999**, *440* (1-2), L809-L814.
86. Mohamed, M. B.; Wang, Z. L.; El-Sayed, M. A., Thermal Reshaping of Gold Nanorods in Micelles. *Journal of Physical Chemistry B* **1998**, *102* (47), 9370-9374.
87. Li, N.; Zhao, P. X.; Astruc, D., Anisotropic Gold Nanoparticles: Synthesis, Properties, Applications, and Toxicity. *Angewandte Chemie-International Edition* **2014**, *53* (7), 1756-1789.

88. Wan, J.; Wang, J.-H.; Liu, T.; Xie, Z.; Yu, X.-F.; Li, W., Surface chemistry but not aspect ratio mediates the biological toxicity of gold nanorods *in vitro* and *in vivo*. *Scientific Reports* **2015**, *5* 11398.
89. Takahashi, H.; Niidome, Y.; Niidome, T.; Kaneko, K.; Kawasaki, H.; Yamada, S., Modification of Gold Nanorods Using Phosphatidylcholine to Reduce Cytotoxicity. *Langmuir* **2006**, *22* (1), 2-5.
90. Alkilany, A. M.; Nagaria, P. K.; Hexel, C. R.; Shaw, T. J.; Murphy, C. J.; Wyatt, M. D., Cellular Uptake and Cytotoxicity of Gold Nanorods: Molecular Origin of Cytotoxicity and Surface Effects. *Small* **2009**, *5* (6), 701-708.
91. Khanal, B. P.; Zubarev, E. R., Rings of nanorods. *Angewandte Chemie-International Edition* **2007**, *46* (13), 2195-2198.
92. Chen, H.; Zhang, X.; Dai, S.; Ma, Y.; Cui, S.; Achilefu, S.; Gu, Y., Multifunctional gold nanostar conjugates for tumor imaging and combined photothermal and chemo-therapy. *Theranostics* **2013**, *3* (9), 633-649.
93. Hao, E. C.; Hupp, J. T.; Schatz, G. C., Synthesis and optical properties of anisotropic metal nanoparticles. *Abstracts of Papers of the American Chemical Society* **2004**, *14* (4), 331-341.
94. Jana, N. R., Gram-scale synthesis of soluble, near-monodisperse gold nanorods and other anisotropic nanoparticles. *Small* **2005**, *1* (8-9), 875-882.
95. Samal, A. K.; Sreeprasad, T. S.; Pradeep, T., Investigation of the role of NaBH₄ in the chemical synthesis of gold nanorods. *Journal of Nanoparticle Research* **2010**, *12* (5), 1777-1786.
96. Xie, J. P.; Lee, J. Y.; Wang, D. I. C., Seedless, surfactantless, high-yield synthesis of branched gold nanocrystals in HEPES buffer solution. *Chemistry of Materials* **2007**, *19* (11), 2823-2830.
97. Pallavicini, P.; Chirico, G.; Collini, M.; Dacarro, G.; Donà, A.; Falqui, A.; Diaz-Fernandez, Y.; Freddi, S.; Garofalo, B.; Genovese, A.; Sironi, L.; Taglietti, A., Synthesis of branched Au nanoparticles with tunable near-infrared LSPR using a zwitterionic surfactant. *Chemical Communications* **2011**, *47* (4), 1315-1317.
98. Weiner, R. G.; Kunz, M. R.; Skrabalak, S. E., Seeding a New Kind of Garden: Synthesis of Architecturally Defined Multimetallic Nanostructures by Seed-Mediated Co-Reduction. *Accounts of Chemical Research* **2015**, *48* (10), 2688-2695.

99. Guerrero-Martínez, A.; Barbosa, S.; Pastoriza-Santos, I.; Liz-Marzán, L. M., Nanostars shine bright for you. *Current Opinion in Colloid & Interface Science* **2011**, *16* (2), 118-127.
100. Chandra, K.; Culver, K. S. B.; Werner, S. E.; Lee, R. C.; Odom, T. W., Manipulating the Anisotropic Structure of Gold Nanostars using Good's Buffers. *Chemistry of Materials* **2016**, *28* (18), 6763-6769.
101. Habib, A.; Tabata, M.; Wu, Y. G., Formation of gold nanoparticles by Good's buffers. *Bulletin of the Chemical Society of Japan* **2005**, *78* (2), 262-269.
102. Grady, J. K.; Chasteen, N. D.; Harris, D. C., Radicals from "Good's" buffers. *Analytical Biochemistry* **1988**, *173* (1), 111-115.
103. Liu, H.; Xu, Y.; Qin, Y.; Sanderson, W.; Crowley, D.; Turner, C. H.; Bao, Y., Ligand-Directed Formation of Gold Tetrapod Nanostructures. *Journal of Physical Chemistry C* **2013**, *117* (33), 17143-17150.
104. Dam, D. H.; Culver, K. S.; Odom, T. W., Grafting Aptamers onto Gold Nanostars Increases *in vitro* Efficacy in a Wide Range of Cancer Cell Types. *Molecular Pharmaceutics* **2014**, *11* (2), 580-587.
105. Dam, D. H. M.; Lee, H.; Lee, R. C.; Kim, K. H.; Kelleher, N. L.; Odom, T. W., Tunable Loading of Oligonucleotides with Secondary Structure on Gold Nanoparticles through a pH-Driven Method. *Bioconjugate Chemistry* **2015**, *26* (2), 279-285.
106. Lee, H.; Dam, D. H. M.; Ha, J. W.; Yue, J.; Odom, T. W., Enhanced Human Epidermal Growth Factor Receptor 2 Degradation in Breast Cancer Cells by Lysosome-Targeting Gold Nanoconstructs. *ACS Nano* **2015**, *9* (10), 9859-9867.
107. Dam, D. H.; Lee, R. C.; Odom, T. W., Improved *in vitro* efficacy of gold nanoconstructs by increased loading of G-quadruplex aptamer. *Nano Letters* **2014**, *14* (5), 2843-2848.
108. Dam, D. H. M.; Culver, K. S. B.; Kandela, I.; Lee, R. C.; Chandra, K.; Lee, H.; Mantis, C.; Ugolkov, A.; Mazar, A. P.; Odom, T. W., Biodistribution and *in vivo* toxicity of aptamer-loaded gold nanostars. *Nanomedicine* **2015**, *11* (3), 671-679.
109. Culver, K. S. B.; Shin, Y. J.; Rotz, M. W.; Meade, T. J.; Hersam, M. C.; Odom, T. W., Shape-Dependent Relaxivity of Nanoparticle-Based T1 Magnetic Resonance Imaging Contrast Agents. *Journal of Physical Chemistry C* **2016**, *120* (38), 22103-22109.
110. Saverot, S.; Geng, X.; Leng, W.; Vikesland, P. J.; Grove, T. Z.; Bickford, L. R., Facile, tunable, and SERS-enhanced HEPES gold nanostars. *RSC Advances* **2016**, *6* (35), 29669-29673.

111. Lee, K. S.; El-Sayed, M. A., Gold and silver nanoparticles in sensing and imaging: Sensitivity of plasmon response to size, shape, and metal composition. *Journal of Physical Chemistry B* **2006**, *110* (39), 19220-19225.
112. Zhao, P. X.; Li, N.; Astruc, D., State of the art in gold nanoparticle synthesis. *Coordination Chemistry Reviews* **2013**, *257* (3-4), 638-665.
113. Umadevi, S.; Lee, H. C.; Ganesh, V.; Feng, X.; Hegmann, T., A versatile, one-pot synthesis of gold nanostars with long, well-defined thorns using a lyotropic liquid crystal template. *Liquid Crystals* **2014**, *41* (3), 265-276.
114. Chen, R.; Wu, J. L.; Li, H.; Cheng, G.; Lu, Z.; Che, C. M., Fabrication of gold nanoparticles with different morphologies in HEPES buffer. *Chinese Journal of Rare Metals* **2010**, *29* (2), 180-186.
115. Cai, J.; Raghavan, V.; Bai, Y. J.; Zhou, M. H.; Liu, X. L.; Liao, C. Y.; Ma, P.; Shi, L.; Dockery, P.; Keogh, I.; Fan, H. M.; Olivo, M., Controllable synthesis of tetrapod gold nanocrystals with precisely tunable near-infrared plasmon resonance towards highly efficient surface enhanced Raman spectroscopy bioimaging. *Journal of Physical Chemistry B* **2015**, *3* (37), 7377-7385.
116. Niidome, Y.; Nishioka, K.; Kawasaki, H.; Yamada, S., Rapid synthesis of gold nanorods by the combination of chemical reduction and photoirradiation processes; morphological changes depending on the growing processes. *Chemical Communication (Cambridge, U. K.)* **2003**, (18), 2376-2377.
117. Yang, Y.; Wang, W.; Li, J.; Mu, J.; Rong, H., Manipulating the solubility of gold nanoparticles reversibly and preparation of water-soluble sphere nanostructure through micellar-like solubilization. *Journal of Physical Chemistry B* **2006**, *110* (34), 16867-16873.
118. Mahmoud, M. A.; El-Sayed, M. A.; Gao, J. P.; Landman, U., High-Frequency Mechanical Stirring Initiates Anisotropic Growth of Seeds Requisite for Synthesis of Asymmetric Metallic Nanoparticles like Silver Nanorods. *Nano Letters* **2013**, *13* (10), 4739-4745.
119. Nehl, C. L.; Hafner, J. H., Shape-dependent plasmon resonances of gold nanoparticles. *Journal of Materials Chemistry* **2008**, *18* (21), 2415-2419.
120. Dondapati, S. K.; Sau, T. K.; Hrelescu, C.; Klar, T. A.; Stefani, F. D.; Feldmann, J., Label-free Biosensing Based on Single Gold Nanostars as Plasmonic Transducers. *ACS Nano* **2010**, *4* (11), 6318-6322.
121. Hao, F.; Nehl, C. L.; Hafner, J. H.; Nordlander, P., Plasmon resonances of a gold nanostar. *Nano Letters* **2007**, *7* (3), 729-732.

122. Haiss, W.; Thanh, N. T. K.; Aveyard, J.; Fernig, D. G., Determination of size and concentration of gold nanoparticles from UV-Vis spectra. *Analytical Chemistry* **2007**, *79* (11), 4215-4221.
123. Link, S.; El-Sayed, M. A., Size and temperature dependence of the plasmon absorption of colloidal gold nanoparticles. *Journal of Physical Chemistry B* **1999**, *103* (21), 4212-4217.
124. Carrasco, S.; Benito-Pena, E.; Navarro-Villoslada, F.; Langer, J.; Sanz-Ortiz, M. N.; Reguera, J.; Liz-Marzan, L. M.; Moreno-Bondi, M. C., Multibranched Gold-Mesoporous Silica Nanoparticles Coated with a Molecularly Imprinted Polymer for Label-Free Antibiotic Surface Enhanced Raman Scattering Analysis. *Chemistry of Materials* **2016**, *28* (21), 7947-7954.
125. Pallavicini, P.; Dona, A.; Casu, A.; Chirico, G.; Collini, M.; Dacarro, G.; Falqui, A.; Milanese, C.; Sironi, L.; Taglietti, A., Triton X-100 for three-plasmon gold nanostars with two photothermally active NIR (near IR) and SWIR (short-wavelength IR) channels. *Chemical Communications* **2013**, *49* (56), 6265-6267.
126. Nehl, C. L.; Liao, H. W.; Hafner, J. H., Optical properties of star-shaped gold nanoparticles. *Nano Letters* **2006**, *6* (4), 683-688.
127. Sau, T. K.; Murphy, C. J., Room temperature, high-yield synthesis of multiple shapes of gold nanoparticles in aqueous solution. *Journal of the American Chemical Society* **2004**, *126* (28), 8648-8649.
128. Kumar, P. S.; Pastoriza-Santos, I.; Rodriguez-Gonzalez, B.; Garcia de Abajo, F. J.; Liz-Marzan, L. M., High-yield synthesis and optical response of gold nanostars. *Nanotechnology* **2008**, *19* (1), 015606.
129. Caswell, K. K.; Bender, C. M.; Murphy, C. J., Seedless, surfactantless wet chemical synthesis of silver nanowires. *Nano Letters* **2003**, *3* (5), 667-669.
130. Ghosh, S.; Bachilo, S. M.; Weisman, R. B., Advanced sorting of single-walled carbon nanotubes by nonlinear density-gradient ultracentrifugation. *Nature Nanotechnology* **2010**, *5* (6), 443-450.
131. Krueger, K. M.; Al-Somali, A. M.; Falkner, J. C.; Colvin, V. L., Characterization of nanocrystalline CdSe by size exclusion chromatography. *Analytical Chemistry* **2005**, *77* (11), 3511-3515.
132. Akthakul, A.; Hochbaum, A. I.; Stellacci, F.; Mayes, A. M., Size fractionation of metal nanoparticles by membrane filtration. *Advanced Materials* **2005**, *17* (5), 532-534.

133. Sweeney, S. F.; Woehle, G. H.; Hutchison, J. E., Rapid purification and size separation of gold nanoparticles via diafiltration. *Journal of the American Chemical Society* **2006**, *128* (10), 3190-3197.
134. Hanauer, M.; Pierrat, S.; Zins, I.; Lotz, A.; Sonnichsen, C., Separation of nanoparticles by gel electrophoresis according to size-and shape. *Nano Letters* **2007**, *7* (9), 2881-2885.
135. Shin, Y. J.; Ringe, E.; Personick, M. L.; Cardinal, M. F.; Mirkin, C. A.; Marks, L. D.; Van Duyne, R. P.; Hersam, M. C., Centrifugal Shape Sorting and Optical Response of Polyhedral Gold Nanoparticles. *Advanced Materials* **2013**, *25* (29), 4023-4027.
136. Akbulut, O.; Mace, C. R.; Martinez, R. V.; Kumar, A. A.; Nie, Z. H.; Patton, M. R.; Whitesides, G. M., Separation of Nanoparticles in Aqueous Multiphase Systems through Centrifugation. *Nano Letters* **2012**, *12* (8), 4060-4064.
137. Novak, J. P.; Nickerson, C.; Franzen, S.; Feldheim, D. L., Purification of molecularly bridged metal nanoparticle arrays by centrifugation and size exclusion chromatography. *Analytical Chemistry* **2001**, *73* (23), 5758-5761.
138. Zhang, L.; Swift, J.; Butts, C. A.; Yerubandi, V.; Dmochowski, I. J., Structure and activity of apoferritin-stabilized gold nanoparticles. *Journal of Inorganic Biochemistry* **2007**, *101* (11-12), 1719-1729.
139. Coombs, D. H.; Watts, N. R. M., Generating Sucrose Gradients in 3 Minutes by Tilted Tube Rotation. *Analytical Biochemistry* **1985**, *148* (1), 254-259.
140. Robertson, J. D.; Rizzello, L.; Avila-Olias, M.; Gaitzsch, J.; Contini, C.; Magon, M. S.; Renshaw, S. A.; Battaglia, G., Purification of Nanoparticles by Size and Shape. *Scientific Reports* **2016**, *6* 27494.
141. Fang, C.; Bhattarai, N.; Sun, C.; Zhang, M. Q., Functionalized Nanoparticles with Long-Term Stability in Biological Media. *Small* **2009**, *5* (14), 1637-1641.
142. Surette, M. C.; Nason, J. A., Effects of surface coating character and interactions with natural organic matter on the colloidal stability of gold nanoparticles. *Environmental Science-Nano* **2016**, *3* (5), 1144-1152.
143. Sokolov, K.; Follen, M.; Aaron, J.; Pavlova, I.; Malpica, A.; Lotan, R.; Richards-Kortum, R., Real-time vital optical imaging of precancer using anti-epidermal growth factor receptor antibodies conjugated to gold nanoparticles. *Cancer Research* **2003**, *63* (9), 1999-2004.
144. Kennedy, L. C.; Bickford, L. R.; Lewinski, N. A.; Coughlin, A. J.; Hu, Y.; Day, E. S.; West, J. L.; Drezek, R. A., A New Era for Cancer Treatment: Gold-Nanoparticle-Mediated Thermal Therapies. *Small* **2011**, *7* (2), 169-183.

145. Huang, X. H.; Jain, P. K.; El-Sayed, I. H.; El-Sayed, M. A., Plasmonic photothermal therapy (PPTT) using gold nanoparticles. *Lasers in Medical Science* **2008**, *23* (3), 217-228.
146. Huang, X. H.; Jain, P. K.; El-Sayed, I. H.; El-Sayed, M. A., Gold nanoparticles: interesting optical properties and recent applications in cancer diagnostic and therapy. *Nanomedicine* **2007**, *2* (5), 681-693.
147. Walker, D. A.; Leitsch, E. K.; Nap, R. J.; Szleifer, I.; Grzybowski, B. A., Geometric curvature controls the chemical patchiness and self-assembly of nanoparticles. *Nature Nanotechnology* **2013**, *8* (9), 676-681.
148. Hill, H. D.; Millstone, J. E.; Banholzer, M. J.; Mirkin, C. A., The Role Radius of Curvature Plays in Thiolated Oligonucleotide Loading on Gold Nanoparticles. *ACS Nano* **2009**, *3* (2), 418-424.
149. Sang, L. C.; Coppens, M. O., Effects of surface curvature and surface chemistry on the structure and activity of proteins adsorbed in nanopores. *Physical Chemistry Chemical Physics* **2011**, *13* (14), 6689-6698.
150. Zhang, X.; Liu, B. W.; Dave, N.; Servos, M. R.; Liu, J. W., Instantaneous Attachment of an Ultrahigh Density of Nonthiolated DNA to Gold Nanoparticles and Its Applications. *Langmuir* **2012**, *28* (49), 17053-17060.
151. Hurst, S. J.; Lytton-Jean, A. K. R.; Mirkin, C. A., Maximizing DNA loading on a range of gold nanoparticle sizes. *Abstracts of Papers of the American Chemical Society* **2007**, 233.
152. Massich, M. D.; Giljohann, D. A.; Schmucker, A. L.; Patel, P. C.; Mirkin, C. A., Cellular Response of Polyvalent Oligonucleotide-Gold Nanoparticle Conjugates. *ACS Nano* **2010**, *4* (10), 5641-5646.
153. Sajanlal, P. R.; Sreeprasad, T. S.; Samal, A. K.; Pradeep, T., Anisotropic nanomaterials: structure, growth, assembly, and functions. *Nano Reviews* **2011**, *2* 055014.
154. Giljohann, D. A.; Seferos, D. S.; Patel, P. C.; Millstone, J. E.; Rosi, N. L.; Mirkin, C. A., Oligonucleotide loading determines cellular uptake of DNA-modified gold nanoparticles. *Nano Letters* **2007**, *7* (12), 3818-3821.
155. Mu, Q. X.; Jiang, G. B.; Chen, L. X.; Zhou, H. Y.; Fourches, D.; Tropsha, A.; Yan, B., Chemical Basis of Interactions Between Engineered Nanoparticles and Biological Systems. *Chemical Reviews* **2014**, *114* (15), 7740-7781.
156. Cutler, J. I.; Auyeung, E.; Mirkin, C. A., Spherical Nucleic Acids. *Journal of the American Chemical Society* **2012**, *134* (3), 1376-1391.

157. Gao, J.; Huang, X. Y.; Liu, H.; Zan, F.; Ren, J. C., Colloidal Stability of Gold Nanoparticles Modified with Thiol Compounds: Bioconjugation and Application in Cancer Cell Imaging. *Langmuir* **2012**, *28* (9), 4464-4471.
158. Dalal, C.; Saha, A.; Jana, N. R., Nanoparticle Multivalency Directed Shifting of Cellular Uptake Mechanism. *Journal of Physical Chemistry C* **2016**, *120* (24), 13324-13324.
159. Dykman, L.; Khlebtsov, N., Gold nanoparticles in biomedical applications: recent advances and perspectives. *Chemical Society Reviews* **2012**, *41* (6), 2256-2282.
160. Zhang, D. M.; Ansar, S. M., Ratiometric Surface Enhanced Raman Quantification of Ligand Adsorption onto a Gold Nanoparticle. *Analytical Chemistry* **2010**, *82* (13), 5910-5914.
161. Fu, B.; Isaacoff, B. P.; Biteen, J. S., Super-Resolving the Actual Position of Single Fluorescent Molecules Coupled to a Plasmonic Nanoantenna. *ACS Nano* **2017**, *11* (9), 8978-8987.
162. Donehue, J. E.; Wertz, E.; Talicska, C. N.; Biteen, J. S., Plasmon-Enhanced Brightness and Photostability from Single Fluorescent Proteins Coupled to Gold Nanorods. *Journal of Physical Chemistry C* **2014**, *118* (27), 15027-15035.
163. Yu, H. X.; Xu, X. W.; Liang, P. P.; Loh, K. Y.; Guntupalli, B.; Roncancio, D.; Xiao, Y., A Broadly Applicable Assay for Rapidly and Accurately Quantifying DNA Surface Coverage on Diverse Particles. *Bioconjugate Chemistry* **2017**, *28* (4), 933-943.
164. Wertz, E. A.; Isaacoff, B. P.; Biteen, J. S., Wavelength-Dependent Super-resolution Images of Dye Molecules Coupled to Plasmonic Nanotriangles. *ACS Photonics* **2016**, *3* (10), 1733-1740.
165. Hinterwirth, H.; Kappel, S.; Waitz, T.; Prohaska, T.; Lindner, W.; Lammerhofer, M., Quantifying Thiol Ligand Density of Self-Assembled Monolayers on Gold Nanoparticles by Inductively Coupled Plasma-Mass Spectrometry. *ACS Nano* **2013**, *7* (2), 1129-1136.
166. Blythe, K. L.; Willets, K. A., Super-Resolution Imaging of Fluorophore-Labeled DNA Bound to Gold Nanoparticles: A Single-Molecule, Single-Particle Approach. *Journal of Physical Chemistry C* **2016**, *120* (2), 803-815.
167. Winograd, N., Imaging Mass Spectrometry on the Nanoscale with Cluster Ion Beams. *Analytical Chemistry* **2015**, *87* (1), 328-333.
168. Seah, M. P.; Spencer, S. J.; Havelund, R.; Gilmore, I. S.; Shard, A. G., Depth resolution at organic interfaces sputtered by argon gas cluster ions: the effect of energy, angle and cluster size. *Analyst* **2015**, *140* (19), 6508-6516.

169. DeBord, J. D.; Fernandez-Lima, F. A.; Verkhoturov, S. V.; Schweikert, E. A.; Della-Negra, S., Characteristics of positive and negative secondary ions emitted from Au₃⁺ and Au₄₀₀⁺⁴ impacts. *Surface and Interface Analysis* **2013**, *45* (1), 134-137.
170. Eller, M. J.; Verkhoturov, S. V.; Schweikert, E. A., Testing Molecular Homogeneity at the Nanoscale with Massive Cluster Secondary Ion Mass Spectrometry. *Analytical Chemistry* **2016**, *88* (15), 7639-7646.
171. Rickman, R. D.; Verkhoturov, S. V.; Parilis, E. S.; Schweikert, E. A., Simultaneous ejection of two molecular ions from keV gold atomic and polyatomic projectile impacts. *Physical Review Letters* **2004**, *92* (4), -.
172. Liang, C. K.; Verkhoturov, S. V.; Chen, L. J.; Schweikert, E. A., Size-dependent emission of negative ions from gold nanoparticles bombarded with C-60 and Au-400. *International Journal of Mass Spectrometry* **2013**, *334* 43-48.
173. Pinnick, V.; Rajagopalachary, S.; Verkhoturov, S. V.; Kaledin, L.; Schweikert, E. A., Characterization of Individual Nano-Objects by Secondary Ion Mass Spectrometry. *Analytical Chemistry* **2008**, *80* (23), 9052-9057.
174. Liang, C.-K.; Verkhoturov, S. V.; Chen, L.-J.; Schweikert, E. A., Size-dependent emission of negative ions from gold nanoparticles bombarded with C60 and Au400. *International Journal of Mass Spectrometry* **2013**, *334* (0), 43-48.
175. Chandra, K.; Kumar, V.; Werner, S. E.; Odom, T. W., Separation of Stabilized MOPS Gold Nanostars by Density Gradient Centrifugation. *ACS Omega* **2017**, *2* (8), 4878-4884.
176. Majumder, M.; Rendall, C. S.; Eukel, J. A.; Wang, J. Y. L.; Behabtu, N.; Pint, C. L.; Liu, T. Y.; Orbaek, A. W.; Mirri, F.; Nam, J.; Barron, A. R.; Hauge, R. H.; Schmid, H. K.; Pasquali, M., Overcoming the "Coffee-Stain" Effect by Compositional Marangoni-Flow-Assisted Drop-Drying. *Journal of Physical Chemistry B* **2012**, *116* (22), 6536-6542.
177. Nimse, S. B.; Pal, D., Free radicals, natural antioxidants, and their reaction mechanisms. *RSC Advances* **2015**, *5* (35), 27986-28006.
178. Abedini, A.; Daud, A. R.; Hamid, M. A. A.; Othman, N. K.; Saion, E., A review on radiation-induced nucleation and growth of colloidal metallic nanoparticles. *Nanoscale Research Letters* **2013**, *8* 474.
179. Misra, N.; Biswal, J.; Gupta, A.; Sainis, J. K.; Sabharwal, S., Gamma radiation induced synthesis of gold nanoparticles in aqueous polyvinyl pyrrolidone solution and its application for hydrogen peroxide estimation. *Radiation Physics and Chemistry* **2012**, *81* (2), 195-200.

180. Biswal, J.; Ramnani, S. P.; Shirolkar, S.; Sabharwal, S., Seedless synthesis of gold nanorods employing isopropyl radicals generated using gamma radiolysis technique. *International Journal of Nanotechnology* **2010**, 7 (9-12), 907-918.
181. Misra, N.; Kumar, V.; Borde, L.; Varshney, L., Localized surface plasmon resonance-optical sensors based on radiolytically synthesized silver nanoparticles for estimation of uric acid. *Sensors and Actuators, B: Chemical* **2013**, 178 371-378.
182. Lu, Y.; Zhang, C. Y.; Hao, R.; Zhang, D. J.; Fu, Y. Z.; Moeendarbari, S.; Pickering, C. S.; Hao, Y. W.; Liu, Y. Q., Morphological transformations of silver nanoparticles in seedless photochemical synthesis. *Materials Research Express* **2016**, 3 (5).
183. Gordy, W., *Theory and applications of electron spin resonance*. Wiley: New York, 1980; Vol. 15, p xi, 625 p.
184. Okitsu, K.; Yue, A.; Tanabe, S.; Matsumoto, H.; Yobiko, Y., Formation of colloidal gold nanoparticles in an ultrasonic field: Control of rate of gold(III) reduction and size of formed gold particles. *Langmuir* **2001**, 17 (25), 7717-7720.
185. Chen, X.; Li, C.; Cao, H. L., Recent developments of the in situ wet cell technology for transmission electron microscopies. *Nanoscale* **2015**, 7 (11), 4811-4819.
186. Yuk, J. M.; Park, J.; Ercius, P.; Kim, K.; Hellebusch, D. J.; Crommie, M. F.; Lee, J. Y.; Zettl, A.; Alivisatos, A. P., High-resolution EM of colloidal nanocrystal growth using graphene liquid cells. *Science* **2012**, 336 (6077), 61-64.

CURRICULUM VITAE

Department of Materials Science and Engineering
2220 Campus Drive, Cook Hall 2036
Evanston, IL 60208

Office: 847-491-7553
kavitachandra2017@u.northwestern.edu

A. Education

| | |
|--|-------------|
| Northwestern University <i>Doctor of Philosophy in Materials Science in Engineering</i> | 2012 – 2017 |
| Massachusetts Institute of Technology <i>Bachelor in Material Science Engineering</i> | 2008 – 2012 |

B. Research Experience

| | |
|--|----------------|
| Northwestern University, Odom Lab <i>Graduate Researcher</i> | 2012 – Present |
| <ul style="list-style-type: none"> • GPA: 3.5/4.0; Awarded Biotechnology Training and Hierarchical Materials Fellowships • Thesis topic: Anisotropic Gold Nanostars: Seedless Growth Mechanism, Post-Synthetic Separation, and Ligand Distribution Quantification • Published 4 peer-reviewed papers; presented 2 posters & 4 invited talks; trained 5 undergrad mentees • Initiated 6 internal NU and external collaborations at UIUC, GA Tech, Texas A&M, and Stanford | |
| Massachusetts Institute of Technology, Sadoway Lab <i>Undergraduate Researcher</i> | 2010 – 2012 |
| <ul style="list-style-type: none"> • Created case study of strontium-antimony alloys to create a longer lasting, more efficient liquid metal battery • Presented poster research at Material Research Society Conference 2011 | |
| Massachusetts Institute of Technology, Grossman Lab <i>Undergraduate Researcher</i> | 2010 |
| <ul style="list-style-type: none"> • Modeled cement mixing with water to maximize interactions to mitigate high temperatures and CO₂ emissions | |
| Massachusetts Institute of Technology, Cooney Lab <i>Undergraduate Researcher</i> | 2009 |
| <ul style="list-style-type: none"> • Developed novel test holder apparatus for the VanKel bath that allowed for more streamline testing of tablets | |

C. Peer-Reviewed Publications, Printed Editorials, and Posters

-
1. Michael J. Eller,* Kavita Chandra,* Teri W. Odom, and Emile A. Schweikert, *Label Free Particle-by-Particle Quantification of DNA-Loading on Sorted Gold Nanostars*, in preparation to submit to **Analytical Chemistry** (*indicates co-first authorship)
 2. Kavita Chandra, Brandon Rugg, Juyeong Kim, Qian Chen, Mark Ratner, Michael R. Wasielewski, Teri W. Odom, *Detecting and Visualizing Reaction Intermediates of Anisotropic Nanoparticle Growth*, **Journal of American Chemical Society**, **2018**, 140 (9), 3219–3222
 3. Kavita Chandra, Vished Kumar, Stephanie Werner, Teri W. Odom, *Separation of Stabilized MOPS Gold Nanostars by Density Gradient Centrifugation*, **ACS Omega**, 2017, 2(8), 4878-4884

4. Kavita Chandra, Kayla SB Culver, Stephanie Werner, Raymond Lee, Teri W. Odom, *Manipulating the Anisotropic Structure of Gold Nanostars using Good's Buffers*, **Chemistry of Materials**, 2016, 28(18), 6763-6769
5. Kavita Chandra, Kayla Culver, Teri W. Odom, *Manipulating the shape of anisotropic gold nanostars through synthesis with Good's buffers*, poster presentation at **Gordon Research Conference: Noble Metal Nanoparticles**, 18 June 2016
6. Kavita Chandra, *A gold star for cancer research: nanoparticle defend new cancer drugs*, **Helix Magazine**, 2016
7. Kavita Chandra, *A formula for women in science*, As You Were Saying op-ed, **Boston Herald**, 2015
8. Yi Hua, Kavita Chandra, Duncan Dam, Gary P. Weiderrecht, Teri W. Odom, *Shape-dependent Nonlinear Responses of Anisotropic Gold Nanoparticles*, **Journal of Physical Chemistry Letters**, 2015, 6, 4904-4908
9. Duncan Dam, Kayla SB Culver, Irwati Kandela, Raymond C Lee, Kavita Chandra, Hyojin Lee, Christine Mantis, Andrey Ugolkov, Andrew Mazar, Teri W. Odom, *Biodistribution and in vivo toxicity of aptamer-loaded gold nanostars*, **Nanomedicine**, 2014, 11 (3), 671-679
10. Kavita Chandra, Sophie Poizeau, Donald Sadoway, *Determination of the thermodynamic properties of the Sr-Sb system by EMF measurements with SrF₂ electrolyte*, poster presentation at **Material Research Symposium**, 28 November 2011

D. Leadership and Work Experience

| | |
|--|-------------|
| Science Policy Outreach Taskforce (SPOT) <i>Co-Chair, Founding Member</i> | 2016 – 2018 |
| <ul style="list-style-type: none"> • Recruited 100+ members to join SPOT • Organized 2 town halls with Illinois Representative Robyn Gabel • Developed relationships and organized meetings with U.S. Senator Tammy Duckworth representatives | |
| Mirzayan Science Policy Fellowship at the National Academies of Science, Engineering and Medicine <i>Fellow</i> | 2016 |
| <ul style="list-style-type: none"> • Wrote an exhaustive 50-pg review on current K-12 engineering educator standards and practices in the U.S. for the National Academies of Engineering report 'Educator Capacity Building in PreK-12 Engineering Education' • Created and distributed promotional material which increased membership and connectivity on Link Engineering website | |
| Graduate Women Across Northwestern <i>Treasurer</i> | 2015 – 2017 |
| <ul style="list-style-type: none"> • Created a quarterly networking event accessible to 1,500+ graduate women from different disciplines to meet and collaborate • Authored and awarded a \$3,000 grant from The Graduate School at NU to fund quarterly networking events | |
| Expanding Youth Horizons (EYH) Chicago Conference <i>Organizer, Subcommittee Member</i> | 2015 |
| <ul style="list-style-type: none"> • Helped with logistics of weekend conference exposing middle school girls to STEM careers | |
| ComSciCon (Communicating Science Conference) Chicago <i>Participant for 2015 and Organizer for 2016</i> | 2015 – 2016 |

- Secured \$1,000 in funding from NU Materials Umbrella Society; recruited 3 speakers for the 2-day conference
- Promoted ComSciCon 2016 to universities across the Midwest and increased total number of applicants by ~30% to 200

MIT Accelerating Information Technology Initiative, Google-sponsored 2011 – 2012
Entrepreneurship Co-Instructor

- Taught business modeling and entrepreneurial skills to 60+ college students and served as an advisor in creating Android app start-ups at University of Ghana Accra (UGA) and University of Philippines Diliman (UPD)
- Generated initiatives to increase female enrollment in comp sci with the UGA Student's Council Women's Commission
- Interviewed on popular radio show (E-Talakayan) to promote women in STEM fields; syndicated across all 8 UP campuses

Medlinks at MIT 2010 – 2012
Vice President, Treasurer

- Managed a \$30K budget and aided negotiation with Sturbridge Hotel for a three-year contract for training
- Founded a Residential Grant Program that allows students from any MIT dormitory to apply for money for events; this enabled transparency of the budget to the members and promoted Medlinks recognition

Habitat for Humanity at MIT 2010 – 2011
Co-President, Secretary

- Increased attendance to annual Benefit Concert fourfold by utilizing SAO online ticketing and forging relationships with well-recognized groups, producing profits over \$1000 to build homes in Haiti
- Spearheaded a campaign to raise funds for building MIT sponsored house with green technology
- Created the Beaver Dash, a 5K race, raised \$8000+ through donations from a 10+ local businesses

Other Membership Associations:

Consulting: Bain Advance into Consulting, Bridge to Boston Consulting Group, McKinsey Women's Leadership Challenge, MIT Four Consulting

Science: Ready Set Go Science Communication Program, Society of Women Engineers, Association for Women in Science, Material Science Student Association

Leadership: MIT Leadershape, Community Catalyst Leadership Program

Dance: Northwestern Anubhav Dance, MIT Chamak Dance Team (Treasurer), MIT Bhangra Dance Team

E. Volunteering and Teaching Experience

Adler Planetarium Astro-Journalists 2016
Teacher

- Designed and implemented an 8-week science communication curriculum
- Taught 4 high school students for 2 hours/week; culminated in eight articles published on the Adler website

Niles High STEM Mentorship 2013 – Present
Mentor

- Worked for an academic year with a HS student to develop a science fair project, which went to the Regional Science Fair
- Skyped once a week, and brought her to my lab twice to conduct experiments

Educational Counselor for MIT 2013 – Present
Chicago Region Affiliate

- Interviewed dozens of high school students and wrote decisive reports for admission

Northwestern Hobart Women's Residential College Graduate Fellow 2015 – 2017

Horizons for Homeless Children 2006 – 2008
Volunteer

- Tutored 8-10 underprivileged children once a week at a women's shelter

Other Volunteering Associations: Science in the Classroom (SITC), Science Club, LaunchU Mentor, Chiles High School Math Tutoring Program (*Founder and Volunteer*)

F. Selected Honors, Awards, and Fellowships

Women in STEM at Glenbrook South High School invited speaker, highlighted in Chicago Tribune (<http://www.chicagotribune.com/suburbs/glenview/news/ct-gla-women-stem-breakfast-tl-0208-story.html>), 2018
 Greenhouse Theater *Emilie: La Marquise Du Chatelet Defends Her Life Tonight* invited panelist, 2017
 Northwestern iBIS annual symposium panelist, 2017
 StoryColliders Koshland Museum invited speaker, 2016
 EURAXESS Science Slam North America Finalist and Winner, 2015
 Northwestern Biotechnology Training Mentorship Program Fellowship, 2014
 Northwestern Hierarchical Materials Cluster Program Fellowship, 2013
 Mu Alpha Theta State Keynote Speaker, Orlando, Florida, c.a. 1000 high school students, April 18, 2008
 Valedictorian of Lawton Chiles High School, 2008
 National Merit Scholar, 2008
 National Honor Society, 2004 – 2008
 AP Scholar with Distinction and AP Scholar Award, 2007 – 2008
 Lawton Chiles Science Department Award for Outstanding Student, 2006, 2007
 15th Place Statistics Individual, 10th Place Statistics Team, State Convention, April 2007
 4th Place Statistics Individual, State Invitational, March 2007
 5th place Precalculus Team, 13th place Sequences and Series, 15th Place Trigonometry, National Convention, 2006
 22nd Place Precalculus Individual, 2nd Place Precalculus Team, 7th Place Hustle Team, 6th Place Matrices and Vectors, 13th Place Logarithms and Exponents, State Convention, April 2006
 10th Place Sequences and Series, 2nd Place Algebra II team, National Convention, July 2005
 15th Place in Logarithms, 21st Place in Equations and Inequalities, 4th place Algebra II Team, State Convention 2005
 Duke Talent Identification Program, Grand Level Award, 2003

G. Proficient Skills

Cell culture and Microplate reader
 UV-Vis Spectrophotometer and Fluorimeter
 Inductively coupled plasma mass spectrometry
 Dynamic Light Scattering and Zeta Potential
 Scanning Electron Microscope
 Confocal Microscopy
 High-Resolution and *in situ* Transmission Electron Microscope
 ImageJ
 Matlab, Mathematica (Basic)
 Adobe Illustrator and Photoshop
 Visual Basic and Microsoft Excel